공학박사학위논문

직렬형 하이브리드 기반 6륜 인휠 차량의 최적 주행성, 안정성 및 에너지 효율을 위한 주행제어 알고리즘 개발

Integrated Driving Control Algorithm for Optimized Maneuverability, Stability and energy efficiency of a Series Hybrid Electric Vehicle equipped with Six In-wheel Motors

2012 년 6 월

서울대학교 대학원

협동과정 자동차공학

김 원 균

Abstract

Integrated Driving Control Algorithm for Optimized Maneuverability, Stability and Energy Efficiency of a Series Hybrid Electric Vehicle equipped with Six In-wheel Motors

Wongun Kim
A Program in Automotive Engineering
The Graduate School
Seoul National University

This paper describes an integrated driving control algorithm for optimized maneuverability and stability of a six-wheeled driving/brake and six-wheeled steering (6WD/6WS) electric combat vehicle which is equipped with drive/brake-by-wire and steer-by-wire modules. This integrated driving control algorithm is developed to obtain optimized stability, maneuverability and energy efficiency of a 6WD/6WS vehicle.

The proposed control algorithm consists of four parts: desired dynamics, upper level control, lower level control and power management algorithm. The desired dynamics determines the steering angle of each wheel and the desired acceleration according to driver's steering, throttle, and braking inputs. Stability decision/control, yaw moment control, and speed control algorithms are included in the upper level control layer in order to track the desired dynamics and guarantee yaw and roll stability. The lower level control layer

which is based on a control allocation method computes actuator commands, such as independent driving and regenerative braking torques. In the upper level control layer, the stability decision algorithm defines stability regions on a g-g diagram and calculates the desired longitudinal acceleration based on a G-vectoring control method and the desired yaw rate for lateral and yaw stability, and rollover prevention. The G-vectoring control algorithm determines the longitudinal acceleration required to keep the vehicle stable. The speed control calculates the desired longitudinal net force, and the desired net yaw moment is determined to track the desired yaw rate. Control allocation method is used to design the lower level control layer. Limitations related to the physical maximum output torque and prevention of excessive wheel slip are defined as control input constraints of control allocation, which takes friction circle information into account. For real-time implementation, four candidate methods have been designed and developed to solve the control allocation problem. Feasible method has been adopted, taking execution time into account in order to obtain optimized solutions. In the power management layer, from the determined input torque, the required power can be calculated. The required engine/generator and battery power are determined to minimize energy consumption. Fuel consumption minimization strategy (ECMS) is useful for on-line optimization and adopted to implement real-time applications.

Computer simulations have been conducted to evaluate the proposed integrated driving control algorithm. It has been shown from simulation results that, compared to conventional drive systems, significantly improved vehicle maneuverability and stability can be obtained by the proposed

integrated control algorithm.

Keywords : Driving control algorithm, Control allocation, Lateral stability, Rollover prevention, Energy efficiency, Power management

Student Number : 2008-30901

Contents

List of Tables

List of Figures

Nomenclature

a_{des}	[m/s^2]	Desired acceleration from the acceleration determination algorithm
a_x	[m/s^2]	Measurement of longitudinal vehicle acceleration
a_y	[m/s^2]	Measurement of lateral vehicle acceleration
a_{y_ROM}	[m/s^2]	Acceleration limitation for rollover prevention of stability region
$a_{y\_lateral\_stability}$	[m/s^2]	Acceleration limitation for lateral stability of stability region
a_{y_limit}	[m/s^2]	Acceleration limitation of stability region
$a_{y,c}$	[m/s^2]	Critical value of the lateral acceleration for rollover prevention
f_{pen}		Penalty function for fuel consumption conversion according to SOC
g	[m/s^2]	Gravity acceleration of the earth
$k_{sliding}$		Control gain of sliding control algorithm
$l_{f,m,r}$	[m]	Length from mass center to front, middle and rear axle of the vehicle
$\hat{m}$	[kg]	Nominal mass of the vehicle
$\dot{m}_f$	[g]	Amount of fuel consumption
$\dot{m}_{f,eq}$	[g]	Amount of equivalent fuel consumption
m_s	[kg]	Sprung mass of the vehicle
m_u	[kg]	Unsprung mass of the vehicle
r_w	[m]	Effective wheel radius
w	[m]	Track width from left wheel to right wheel of the vehicle
v_i	[m/s]	Wheel velocity of i-th wheel (i=1,…,6)
v_{des}	[m/s]	Desired velocity from the desired dynamic layer
v_x	[m/s]	Longitudinal vehicle velocity

v_y	[m/s]	Lateral vehicle velocity
$C_{1,2,3}$		Positive constant for calculation of rollover index
$C_{f,m,r}$	[N/rad]	Cornering stiffness of front, middle and rear axle
$\hat{C}_{f,m,r}$	[N/rad]	Nominal cornering stiffness of front, middle and rear axle
F_{xdes}	[N]	Desired longitudinal net force from speed control algorithm
$F_{yf,m,r}$	[N]	Lateral tire force of front, middle and rear wheels
$F_{z,i}$	[N]	Vertical tire forces of i-th wheel (i=1,…,6)
G_x	[m/s^2]	Target of longitudinal acceleration command for G-vectoring control method
I_Z	[kgm^2]	Moment of inertia of the vehicle
$\hat{I}_Z$	[kgm^2]	Nominal moment of inertia of the vehicle
I_{bat}	[A]	Current of battery
J_w	[kgm^2]	Wheel moment of inertia
$J_{E/G}$	[kgm^2]	Moment of inertia of engine/generator shaft
L	[m]	Wheelbase from front axle to third axle of the vehicle
M_{zdes}	[Nm]	Desired net yaw moment for yaw stability control
N		Engine – generator gear ratio
N_{gear}		Steering column gear ratio
P_b	[%]	Brake input command from the driver
$P_{b,i}$	[Mpa]	Brake pressure on i-th wheel (i=1,…,6)
P_{bat}	[W]	Battery output power
$P_{E/G}$	[W]	Engine/generator output power
Q_{bat}	[C]	Quantity of electric charge of battery
R_{int}	[Ω]	Internal resistance of battery
S_{bat}		Conversion efficiency (battery → equivalent fuel)

T_b	[Nm]	Regenerative torque command on i-th wheel (i=1,…,6)
T_i	[Nm]	Torque command on i-th wheel (i=1,…,6)
T_{eng}	[Nm]	Engine output torque command
T_{gen}	[Nm]	Generator output torque command
T_{OOL}	[Nm]	Operating torque for tracking optimal operating line of engine
V_{bat}	[V]	Voltage of battery
$V_{b,OC}$	[V]	Open circuit voltage of battery
V_{ss}	[m/s]	Steady state vehicle velocity according to throttle input for speed control algorithm
V_x	[m/s]	Measurement of vehicle longitudinal velocity
W_u		Weighting factor matrix related to control input
W_v		Weighting factor matrix related to virtual control (desired values)
α	[%]	Throttle input command from the driver
$\alpha_{f,m,r}$	[deg]	Slip angle of the front, middle and rear wheel
β	[m/s]	Side slip velocity of the vehicle
γ	[rad/s]	Yaw rate of the vehicle
γ_{ss}	[rad/s]	Steady state desired yaw rate from driver's steering input
γ_{des}	[rad/s]	Desired yaw rate for yaw stability control from the stability decision algorithm
δ_i	[deg]	Steering angle command on i-th wheel (i=1,…,6)
$\hat{\delta}_i$	[deg]	Nominal steering angle on i-th wheel (i=1,…,6)
δ_{SW}	[deg]	Steering wheel command from the driver
η_{inv}		Inverter efficiency
η_{gen}		Generator efficiency
η_{mot_i}		In-wheel motor efficiency of i-th wheel (i=1,…,6)
λ_i		Wheel slip ratio of i-th wheel (i=1,…,6)

μ		Friction coefficient between tire and road
τ_{yaw}	[s]	Time constant for yaw rate dynamic response model
τ_{motor}	[s]	Time constant for in-wheel motor dynamic time response model
ϕ_{th}	[deg]	Threshold of roll angle for rollover index calculation
$\dot{\phi}_{th}$	[deg/s]	Threshold of roll rate for rollover index calculation
ϕ	[deg]	Measurement of roll angle for rollover index calculation
$\dot{\phi}$	[deg/s]	Measurement of roll rate for rollover index calculation
ω_{id}	[rad/s]	Desired wheel angular velocity of i-th wheel (i=1,…,6)
ω_{OOL}	[rad/s]	Angular velocity for tracking optimal operating line of engine
$\dot{\omega}_{E/G}$	[rad/s^2]	Angular acceleration of engine
ω_i	[rad/s]	Wheel angular velocity of i-th wheel (i=1,…,6)
Φ		Boundary of sliding control algorithm

Chapter 1

Introduction

1.1 Background and Motivation

A six-wheeled driving and six-wheeled steering (6WD/6WS) vehicle is developed and manufactured to adapt to various combat situations. In urban combat situations, it is important that combat vehicles have high stability and maneuverability in order to guarantee a solder's safety and hold the advantage in dangerous situations. Therefore, wheeled vehicles are more suitable for battles in urban conditions than tracked vehicles, but lateral safety and rollover prevention in high speed driving conditions must be ensured. Due to the heavy weight, six wheels are adopted for armored vehicles.

Recently, military ground vehicle systems have been developed using commercial vehicle technologies such as hybrid power, stability and autonomous control systems. By combining conventional power system with an electric drive, advanced hybrid electric systems, and rechargeable energy storage, hybrid electric vehicles (HEVs) add a flexible new dimension to

military operations. The electric system gives a number of advantages, including volume efficiency, fuel efficiency, reduced life cycle costs, reduced environmental impact, and increased stealth characteristics. Batteries are integrated into the electric drive system, which allow the vehicle to be driven silently for several hours with the engines shut down.

By virtue of the recent development of the hybrid systems and in-wheel-motors, drive and brake torque can be independently determined. Electric and hybrid systems have been developed to improve driving performance and energy efficiency. These systems require a control system that can connect a driver with drive-, brake- and steer-by-wire systems.

Figure 1.1 Tracked, six-wheeled and series hybrid combat vehicles
[website : (a) http://www.arthurshall.com, (b) http://commons.wikimedia.org, (c) http://www.mil- itaryhotos.net]

In this paper, series hybrid power systems are adopted to enhance the stability, maneuverability, and energy efficiency for a 6WD/6WS vehicle as shown in figure 1.2.

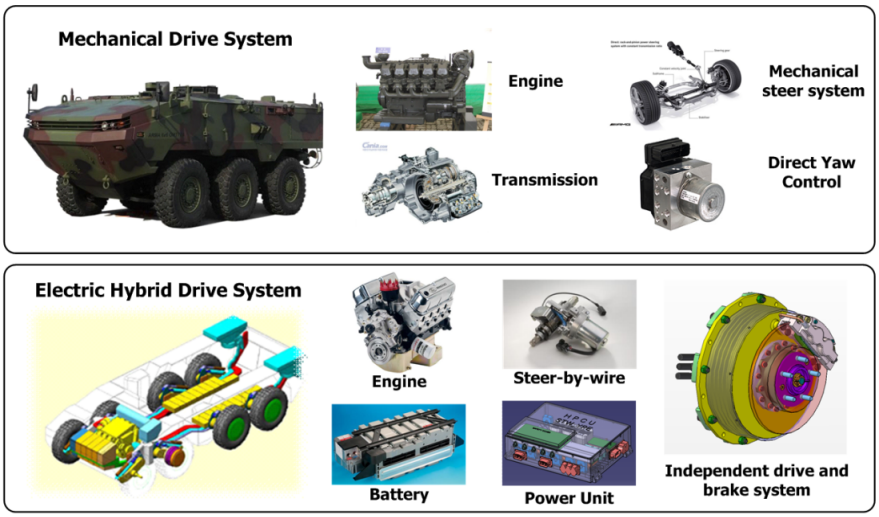

Figure 1.2 Mechanical driver and electric hybrid drive systems

Conventional vehicles are equipped with mechanical steering, drive and braking systems. And the required power is generated by engine and transmission. Compared to conventional six-wheeled vehicles with a mechanical stability control system, a proposed series of hybrid 6WD/6WS vehicles have improved maneuverability and stability by controlling driving, braking torque independently.

1.2 Previous Researches

1.2.1 Lateral Stability Control System

Combat vehicles need to be equipped with a lateral stability control system, because most driving conditions are high speed with risk of drastic turning

maneuvers and slippery roads. Various methods have been studied and actively developed to improve lateral stability of four-wheeled vehicles [Van99, Masao02, Toki01, Nagai99, Song07, Shibahata92]. Recently, research on six wheeled vehicle stability control has been conducted. Huh et al. have set the middle wheel steering angle to half of the front wheel steering angle and controlled the rear wheel steering to minimize the side slip angle of a six-wheeled vehicle [Huh00]. Jackson and Crolla have adopted a yaw rate control method using the Direct Yaw Moment control (DYC) to improve the stability of their six-wheeled vehicle during cornering [Jackson02]. Chen et al. have controlled the middle and rear wheel steering angle using LQR technique with integral control [Chen06]. An et al. have controlled the front, middle and rear wheel steering angle and velocity [An06, An08].

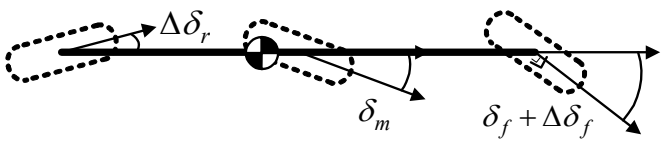

Figure 1.3 Active front and rear steering control for six wheeled vehicle

Vehicles used in previous research were equipped with engine, transmission and differential gears. For these vehicles, only brake torque is used to generate the desired yaw moment and output drive torques on each wheel for lateral or yaw stability, which cannot be controlled independently. A previous stability controller has been designed without the consideration of changes in each wheel load condition that is represented on the friction circle related to the

maximum force that can be generated. Performance of the stability controller is limited on low friction or severe maneuvering driving conditions.

1.2.2 Torque Vectoring Control System

Torque vectoring control system has been adopted and developed to improve performance of stability and maneuverability for all wheeled driving (AWD) vehicle. Torque vectoring is achieved by using redesigned differentials that can distribute power to the wheel or wheels that have traction. In general, two methods are used to generate the yaw moment for conventional four wheeled vehicle. One method is the lateral braking control and the other method is the torque vectoring. The lateral braking control applies different braking forces to the four wheels independently so as to produce a difference in braking force between the left and right wheels, which generates the yaw moment. As this control uses braking forces, it feels to the driver like deceleration, but the control is effective because it can generate yaw moment under a wide range of conditions of vehicle operation. On the other hand, the lateral torque vectoring control transfers the torque from the left to the right wheel, and vice versa, to generate an amount of braking torque on one wheel while generating the same amount of driving torque on the other wheel. The control of this type, therefore, can generate the yaw moment at any time regardless of the engine torque. Another advantage is that it does not affect the total driving and braking forces acting on the vehicle: no conflict with acceleration and deceleration operations.

Lateral braking control	Lateral torque vectoring control
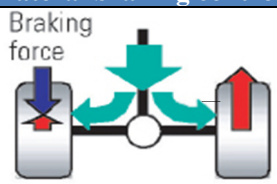	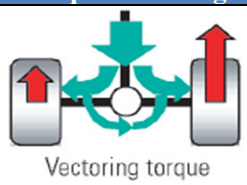
Different braking forces to generate yaw moment	Torque transfer from the left to right wheel

Figure 1.4 Concept of lateral braking and torque vectoring control

Moreover, torque vectoring control algorithm has been developed to control the skid based articulated vehicle equipped with in-wheel motors. In order to turn, independent output torque needs to be generated. To follow driver's command, the desired longitudinal net force and yaw moment should be calculated and different drive and braking forces need to be distributed independently. Therfore, this method can be regarded as torque vectoring control [Kang10].

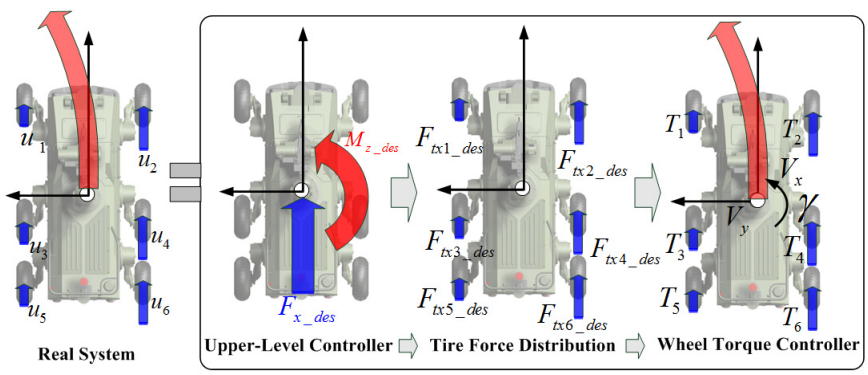

Figure 1.5 Drive, brake and turning control for skid based articulated vehicle

In this paper, the torque vectoring control algorithm has been included and developed to improve performance of maneuverability and stability of the vehicle equipped with in-wheel motors, which can generate drive and brake torque independently.

1.2.3 G-Vectoring Control System

The G-vectoring control algorithm was developed to satisfy improvement in vehicle agility and stability [Yamakado10]. In recent years, researches have been progressed about some benefits in terms of the interconnection and system control of the steering (lateral motion) and acceleration and brake systems (longitudinal motion) in vehicles. The G-vectoring control is based on the control that makes the direction of synthetic acceleration $G = G(G_x, G_y)$ on a 'g-g' diagram seamlessly change using the lateral jerk information. Figure 1.6 shows G-vectoring control scheme.

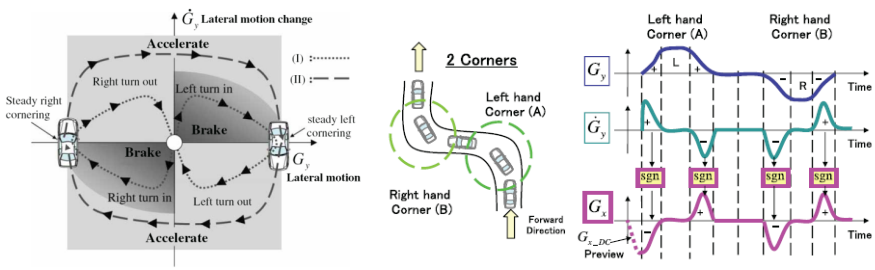

Figure 1.6 G-vectoring control for agility and lateral stability

The proposed G-vectoring control algorithm has been designed to prevent

rollover and lateral stability and it is based on the sliding control algorithm. The control $G = G(G_x)$ used in this paper is similar to previous research which has been developed. However, the control objective is different. The control law, longitudinal acceleration G_x, is determined to reduce excessive lateral acceleration which can make the vehicle unstable.

1.2.4 Control Allocation

Control allocation methods are suitable for implementing in automotive applications. Many studies related to control allocation have been conducted to control the aircraft position [Joseph01] and the stability of vehicles [Tondel05]. The control allocation for vehicle application distributes output brake wheel torques of an over-actuated system [Brad06].

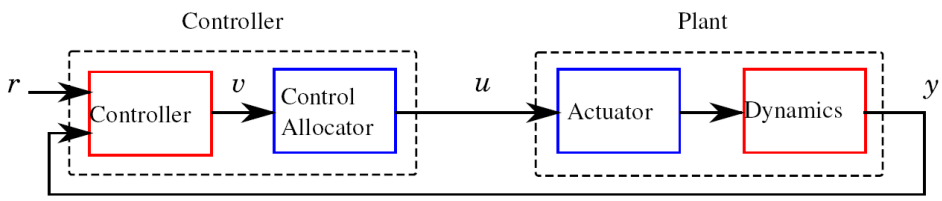

Figure 1.7 Control system structure with control allocation

Fundamentally, control allocation problems can be formulated as optimization problems, where the objective is typically to minimize the use of effort subject to actuator rate and position constraints. In contrast to previous research, modified control allocation of this paper for automotive distribution

solutions is a problem of producing a desired set of forces and moments from a set of actuators with constraints set by friction circles and the performance of power and rate limitations of the actuators. A control allocation method is used to improve performance of maneuvering and stability control. In this study, to apply control allocation algorithm to the proposed control system, the fixed-point [Burken99], interior-point [Vanderbei98], cascaded generalized inverse [Virnig94, Bordignon96] and weighted least square methods [Härkegård02] have been adopted to implement the control allocation algorithm. Proper control allocation method is selected for real-time simulation.

1.2.5 Power Management Control System

Energy optimization methods have been developed to improve energy efficiency in many previous researches. Many research have been studied to implement for parallel and series type hybrid vehicle [Gelb71, Miller05, Sasaki98, Hermance99, Kimura99, Abe00]. The rule-based algorithm [Brahma00, Perez06, Pisu07] and equivalent fuel consumption minimization strategy (ECMS) [Paganelli02] were developed and applied for various hybrid systems. Figure 1.8 shows trend of energy optimization control strategy.

The representative developed algorithms consist of the rule-based and optimization-based algorithm. The rule-based control based on engineer's experience, is handling switching operating modes. Therefore, performance of the optimization algorithm is limited and it is difficult to design algorithm which contains several states. Fuzzy logic technique that may have a degree

of truth between 0 and 1 is used for implementing rule-based method. On the other hand, the optimization-based algorithm determines optimal solutions in order to minimize the performance index defined in global and local time

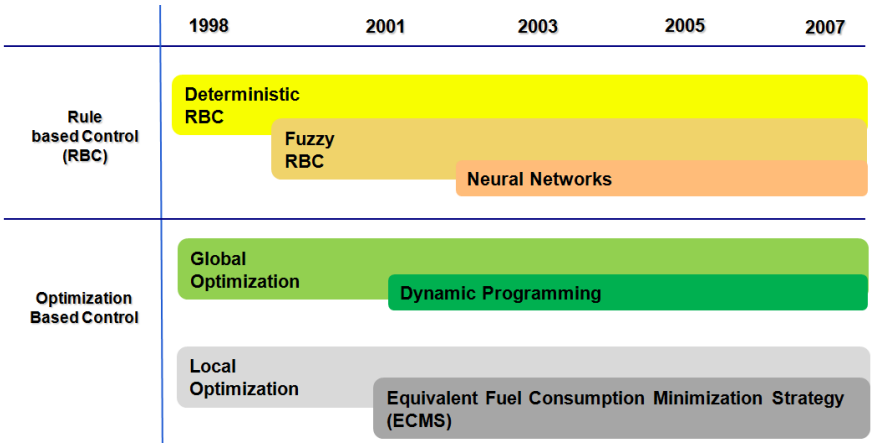

Figure 1.8 Trend of energy optimization control strategy

The dynamic programming (DP) is used to solve the global optimization problem and local optimization problem can be solved by the equivalent fuel consumption minimization (ECMS) algorithm. The DP algorithm can obtain the optimal solution that is the nearest real solution, taking global states into account. However, this method is not suitable for real-time implementation due to many numbers of iterations. The ECMS method is adopted to solve the optimized solution for real-time implementation. Not considering the global optimization, that calculated solution is almost identical to the real solution.

In this paper, to improve energy efficiency of the proposed power system, the power management algorithm should be included in the integrated control

algorithm. The ECMS algorithm is adopted and modified to be suitable for the proposed system.

1.3 Thesis Objectives

The objectives in this dissertation can be classified into three target performance. The first target performance is a maneuverability improvement. The proposed vehicle can drive and turn in severe road conditions such as sand, slippery mud, rock and climbing etc. Maneuverability performance focuses on tracking the desired dynamics that are determined by the driver. The desired dynamics consists of the desired yaw rate and vehicle velocity which are calculated by throttle, brake pedal position and steering wheel angle. Conventional vehicles are equipped with center and axle differential gears. Therefore, output torque applied to individual wheel is identical to each other. This method is named to even distribution. Just even distribution method cannot improve maneuverability performance. Therefore, integrated driving control algorithm needs to be designed to achieve enhanced turning and driving performance.

The second target performance is to guarantee the vehicle stability which includes lateral and yaw stability and rollover prevention. The proposed platform is developed to be suitable for high speed driving conditions. The lateral, yaw stability and rollover prevention are most important design factors. In order to guarantee the lateral stability and prevent rollover, the stability region has been defined by the lateral acceleration limit. And the G-vectoring

control has been developed to maintain stable region which is previously defined. It determines the desired longitudinal acceleration. Also, the yaw stability should be considered as essential factor for vehicle stability. The direct yaw moment control (DYC) algorithm is actively used in a field of conventional unified chassis control (UCC). As a results, functions of an electric stability control (ESC), traction slip control (TCS), anti-lock brake system (ABS), all-wheel drive system (AWD), and electric rollover mitigation system (ERM) have to be included in the proposed control algorithm.

Finally, the third target performance is energy efficiency improvement. Energy consumption minimization strategy should be designed to fit the proposed power system. This power system consists of two engines, generators and batteries. The ECMS algorithm has been adopted and modified to implement the proposed control system.

As a result, the effects of not only maneuverability and stability but also energy efficiency are very important factors to design the integrated driving control algorithm for series hybrid electric vehicle. In this paper, the design process of the integrated driving control algorithm will be explained in detail.

1.4 Thesis Outline

This dissertation can be organized in the following manner. In chapter 2, the control system architecture of the six wheeled steering and driving (6WD/6WS) electric vehicle equipped with series hybrid power system and independent driven in-wheel motors, as a target platform in this paper, is presented. Vehicle dynamic, actuators and power systems are modeled and configured to design the integrated control algorithm respectively.

Specifically, chapter 3 proposes the integrated driving control algorithm. The proposed control algorithm consists of four parts. It consists of the desired dynamics, upper level and lower level control and power management layer. The first part is description of the desired dynamics layer. It determines the desired longitudinal vehicle velocity and yaw rate through throttle, brake and steering wheel angle in order to satisfy the driver's intention. The second part is an upper level controller design for improvement of maneuverability and stability of the vehicle. The upper level control algorithm calculates the desired net force and yaw moment in order to follow the target velocity and yaw rate which are previously defined in the desired dynamics layer. Most importantly, the stability control algorithm is included to guarantee the lateral, yaw stability and rollover prevention in this layer. The G-vectoring and yaw moment control methods has been developed. In the third part, the lower level control layer is explained and based on the control allocation methods which contains fixed-point, cascaded generalized inverse, interior point and weighted least square method. The fixed-point control allocation is adopted to

implement real-time control system by analyzing computer simulations results. Control allocation algorithm is suitable for distribution of output wheel torque of over-actuated system. Finally, the fourth part is related to development of the power management algorithm that is based on the modified ECMS algorithm.

In chapter 4, an estimator needs to be designed to provide the proposed control algorithm with vehicle information. The longitudinal tire force and friction estimations are included and verified by conducting computer simulations.

Simulation has been conducted to verify performance of the integrated driving control algorithm. Turning performance, lateral stability, rollover prevention and energy efficiency improvement are verified.

The conclusions are presented in chapter 6, which also included the summary of the proposed integrated driving control algorithm and the future works to be done.

Chapter 2

Control System Modeling of 6WD/6WS Vehicle

2.1 Control System Overview

Drive/brake and steer-by-wire systems of a 6WD/6WS vehicle are able to control traction, braking, and steering independently. Therefore, in order to design a controller for maneuverability and stability of the vehicle, an integrated driving control algorithm needs to be developed. The integrated driving controller determines steering angles, drive torque, and brake torque on the six wheels independently. These are given from driver's intended steering wheel angle, throttle position, and brake pedal position. This system is equipped with six in-wheel motors and steering motors. The lateral motion of the vehicle is generated by the steering angle of each wheel. And output torque of the in-wheel motors generates tractive and brake forces in order to increase and decrease longitudinal vehicle velocity. The control inputs are the six motor torques and six steering angles which are generated by the integrated driving control algorithm as shown in figure 2.1 (a) and (b). Figure

2.1 (c) shows that integrated brake system is equipped with hydraulic and regenerative braking system. Power system consists of two engine/generator, battery and DC-DC converter. Output power of two engine/generator and battery is used to operate six in-wheel motors. Parameters of power system are expressed in section 2.3 in detail.

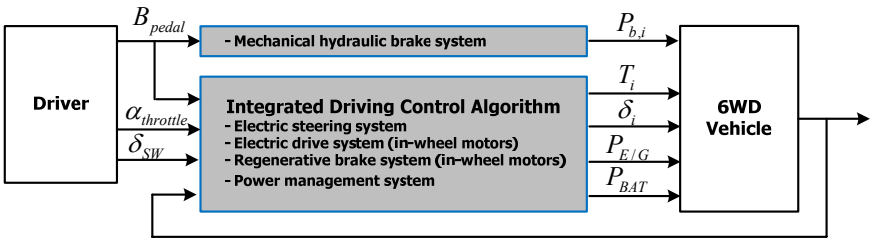

(a) Control Scheme

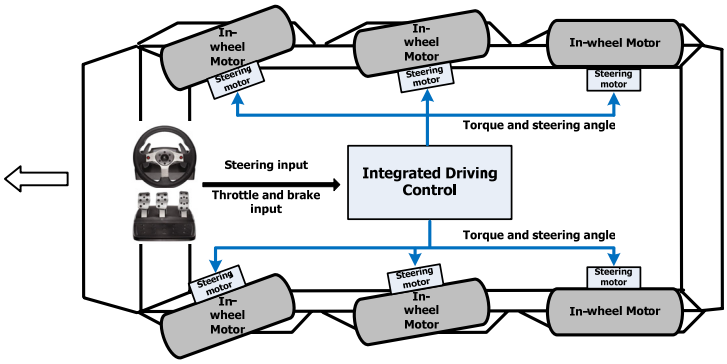

(b) Illustration of integrated driving controller and actuator modules

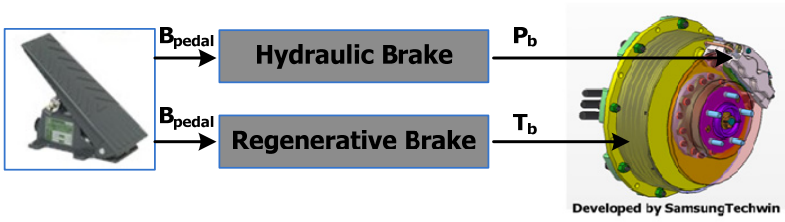

(c) Integrated brake system with hydraulic and regenerative braking

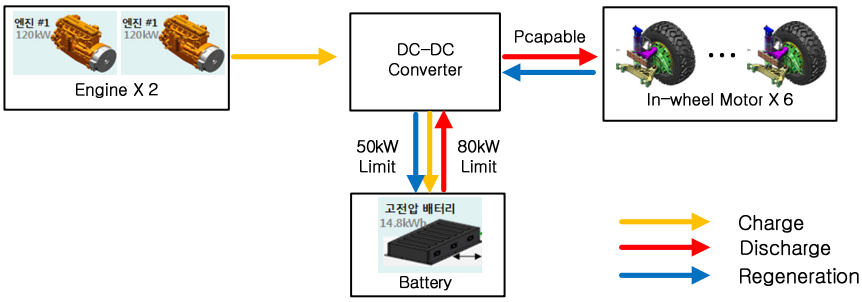

(d) Configuration of power systems

Figure 2.1 Control Scheme and Configuration of the Integrated Driving Control System

Capacity of engine/generator output power is 120 kW respectively. The maximum discharge power is 80 kW and maximum charge power is limited below 40 kW for protection from electric damages. Therefore, the integrated driving control algorithm needs to include distribution algorithm for considering power limitations.

2.2 Control System Architecture

The proposed 6WD/6WS vehicle with serial hybrid power system requires a driving control algorithm that can connect a driver with drive, brake, and steer-by-wire systems. The integrated driving control algorithm consists of a desired dynamics layer, an upper level control layer, and a lower level control layer as shown in figure 2.2. The desired dynamics layer determines the desired steering angle and acceleration/deceleration of the vehicle. The upper level control layer contains stability decision, yaw moment, and speed control algorithms. A main function of the lower level control layer is distribution of wheel torque so as to satisfy a driver's intention. In addition, the lower level control layer takes slip limitations and physical actuator limitations of the in-wheel motor and hydraulic brake system into account.

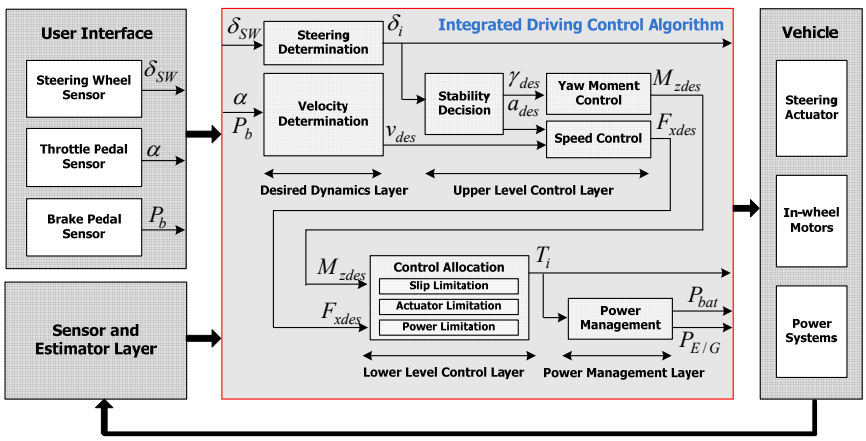

Figure 2.2 Control architecture of an integrated driving control algorithm

Input and output parameters with their classification and the names of their functions are described in table 2.1 in detail. The driver's steering, throttle, and brake commands are determined by a user interface. The integrated driving controller calculates wheel torques and steering angles of each wheel.

Table 2.1. Function table of the driving control algorithm

Classification	Function name	Function	Input parameters	Output parameters
Desired dynamics	Steering determination	Front, middle and rear wheel steering angle determination based on Ackerman steering method	- Driver's steering command	Steering angle each wheel (6 wheel)
	Desired velocity determination	Desired Acceleration/deceleration determination from driver's throttle and brake pedal commands	- Driver's throttle and brake commands - Vehicle velocity	Desired acceleration
Upper level	Stability decision	Lateral, yaw stability and rollover prevention	- Steering angles and desired acceleration - Vehicle acceleration	Desired yaw rate and desired acceleration
	Yaw moment control	Following the desired yaw rate for yaw stability control	- Desired yaw rate - Vehicle yaw rate	Desired net yaw moment
	Speed control	Following the desired vehicle speed for speed control	- Desired acceleration - Desired velocity - Vehicle velocity	Desired longitudinal net force
Lower level	Control allocation	Wheel torque distribution (fixed-point control allocation method)	- Desired net yaw moment - Desired longitudinal net force - Friction circle information	Wheel torque commands
	Slip limitation	Prevention of excessive wheel slip	- Wheel angular velocity - Vehicle velocity	Limitation input torques
	Actuator limitation	Actuator limitation of in-wheel motors and hydraulic brake system	- Vehicle velocity - Wheel angular velocity	Limitation input torques
	Power limitation	Power limitation according to capacity of generable and regenerative power	- Generable power - Regenerative power	Limitation input torques
Power management	ECMS	Reference power determination for improved energy efficiency	- Required power - SOC	Engine and battery power

2.3 Vehicle Dynamic, Actuators and Power System Model

2.3.1 Vehicle dynamic model

The TruckSim software package is used for simulation of dynamic modeling. The full vehicle dynamic model in TruckSim makes it possible to analyze a 6WD /6WS vehicle's maneuverability, such as in the case of a rollover maneuver shown in figure 2.3, and to study the control method for the integrated driving controller.

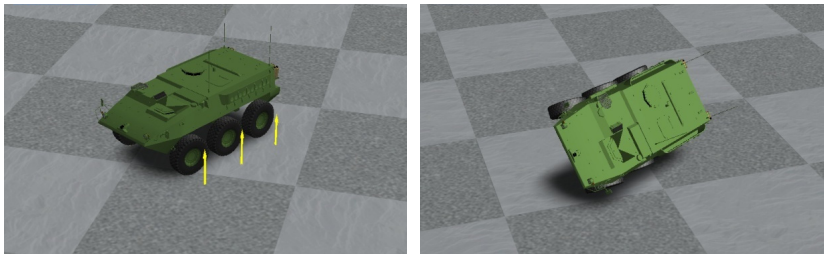

(a) Trucksim dynamic toolbox

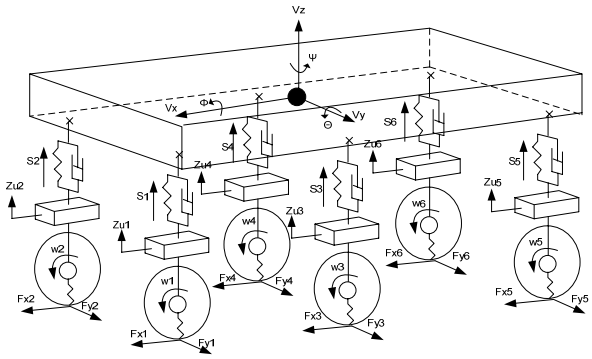

(b) Configuration of dynamic elements

Figure 2.3 TruckSim dynamic model for 6WD/6WS vehicle

A six-wheeled vehicle dynamic model consists of 24 DOF dynamic models that include translational and rotational dynamic models of the sprung mass, 6 suspension models, 6 wheel dynamics models, and 6 steering dynamic models. Wheel dynamics models contain in-wheel motor, brake system, and tire models.

Body dynamics

Body dynamics can be calculated by the Newton and Euler equations. The translational dynamic is based on the Newton equation and the rotational dynamic can be expressed by the Euler equation as follows:

$$\sum F = m_s a_G \tag{2.1}$$

where, $\Sigma F_x = m_s(a_x + v_z w_y - v_y w_z)$

$\Sigma F_y = m_s(a_y + v_x w_z - v_z w_x)$

$\Sigma F_z = m_s(a_z + v_y w_x - v_x w_y)$

$$\sum M = \dot{H}_g \tag{2.2}$$

where, $\Sigma M_x = I_x a_x + (I_z - I_y) w_y w_z$

$\Sigma M_y = I_y a_y + (I_x - I_z) w_z w_x$

$\Sigma M_z = I_z a_z + (I_y - I_x) w_x w_y$

Forces and moment that are applied to the vehicle body generate translation and rotation of the vehicle. The longitudinal and lateral tire forces can be generated by traction/brake torque and steering wheel angle. Also, the vertical tire force can be generated by gravity, vehicle status and road conditions. The suspension dynamics has an effect on vertical tire force determination. These dynamic relations are included in the Trucksim dynamic toolbox. Therefore, all parameters related to body dynamics can be calculated and monitored.

Tire model

Magic Formula tire model provides a method to calculate longitudinal and lateral tire force for a wide range of operating conditions, including large tire slip angle and ratio as well as combined lateral and longitudinal tire force generation [Pacejka02]. The assumption that the lateral tire forces are proportional to the tire slip angles will not be hold at large slip angles. In such cases, the lateral tire force will depend on tire slip angle, vertical tire force, friction coefficient, and also the magnitude of longitudinal tire force that is being simultaneously generated. Therefore, at large slip angles, the lateral tire force model will no longer be linear. When slip ratio is less than 0.2, the longitudinal tire force is proportional to slip ratio according to vertical tire force respectively. However, the longitudinal tire force is reduced according to the increase of the slip angle out of linear range which can be defined as slip angle from 0 to 0.2.

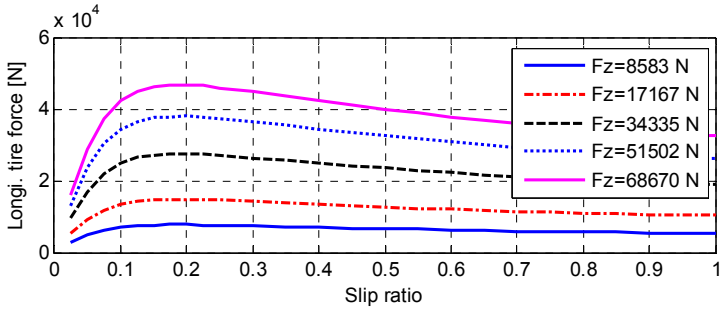

(a) Longitudinal tire force model

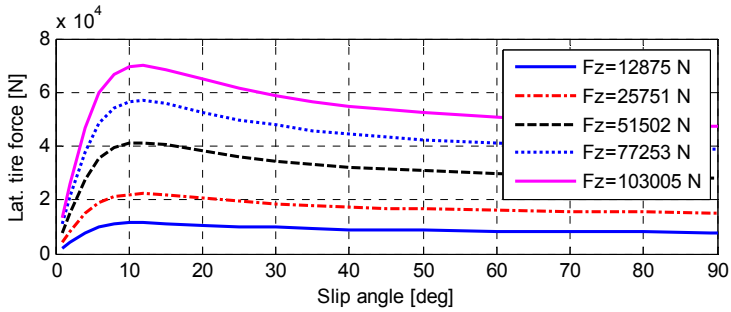

(b) Lateral tire force model

Figure 2.4 Pacejka tire model

Table 2.2 shows chassis specifications of a 6WD/6WS vehicle such as mass, tread, front/rear wheelbase, wheel radius, z-axis moment of inertia and others.

Table 2.2 Specification for a 6WD/6WS Vehicle

Vehicle Parameters	specifications
Sprung Mass (m_s)	7200 [kg]
Unsprung mass (m_u)	962.025 [kg]
Wheelbase (L)	4.6 [m]
Wheel moment inertia (J_w)	14 [kgm^2]
Suspension stiffness (K_{ti})	80000 [N/m]

Tire stiffness (K_r)	560000 [N/m]
Moment inertia (I_Z)	37303 [kgm^2]
Track width (t)	2.264 [m]
Tire radius (r_i)	0.56 [m]
Roll-bar stiffness (K_{ri})	326010 [Nm/rad]

2.3.2 Motor Dynamic model

A 6WD/6WS vehicle equipped with 6 in-wheel-motors is able to operate in differential driving and braking modes. The capacity of in-wheel motor is 50kW. Figure 2.5 (a) shows a performance curve and the efficiency of the in-wheel-motors, and (b) illustrates wheel-in-motor structure.

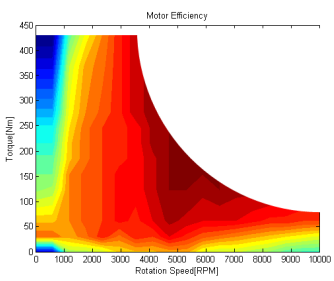

(a) Motor performance curve and efficiency

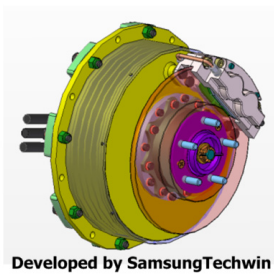

(b) Structure of in-wheel motors

Figure 2.5 Performance curve, efficiency and structure of in-wheel motors

The in-wheel-motor model operates in the following manner: the control input is the desired output torque which is distributed from the lower level controller, and the output of the motor model is the generated torque. The in-wheel-motor is modeled using a first order transfer function:

$$G(s) = \frac{output\ torque}{torque\ command} = \frac{1}{s \cdot \tau_{motor} + 1} \tag{2.3}$$

$$where,\ \tau_{motor} = 0.05$$

2.3.3 Power System Model

Engine power is not related to driving status of the vehicle. Because engine-generator set is not connected with driving shaft in the proposed 6WD/6WS vehicle. Engine-generator dynamics can be described as engine torque, generator torque, gear ratio, moment of inertia of engine shaft.

$$\dot{\omega}_{E/G} = \frac{1}{J_{E/G}}\left(T_{eng} - N \cdot T_{gen}\right) \tag{2.4}$$

Engine dynamic model can be expressed as first-order transfer function. It is assumed that engine control unit (ECU) is able to control required engine output torque. Transient engine torque error cannot affect fuel consumption significantly. Instead of using complicated engine model, fuel consumption map related to engine rotational velocity and output torque is used. Generator model is described by using efficiency map according to angular velocity and operating torque of the generator as follows:

$$P_{gen} = \begin{cases} \dfrac{1}{\eta_{gen}} T_{gen}\omega_{gen} & T_{gen}\omega_{gen} \geq 0 \\ \eta_{gen} T_{gen}\omega_{gen} & T_{gen}\omega_{gen} < 0 \end{cases} \tag{2.5}$$

where $\eta_{gen} = f\left(T_{gen}, \omega_{gen}\right)$, P_{gen} is generator power, ω_{gen} is generator angular velocity, T_{gen} is generated torque and η_{gen} is generator efficiency according to torque and angular velocity of the generator.

Battery power can be obtained by generative/regenerative power and efficiency of DC-DC converter instead of detailed DC-DC converter model.

$$P_{bat} = \begin{cases} \eta_{inv} \cdot \left(P_{gen} - P_{mot}\right) & if \;\; P_{gen} - P_{mot} \geq 0 \\ \dfrac{1}{\eta_{inv}} \cdot \left(P_{gen} - P_{mot}\right) & if \;\; P_{gen} - P_{mot} < 0 \end{cases} \tag{2.6}$$

where, P_{bat} is battery power, η_{inv} is inverter efficiency and P_{mot} is driving motor power.

Motor power dynamic model is designed to calculate operating motor power. Efficiency is determined by angular velocity and output torque of each in-wheel motor. Total required motor power is the sum of generative / regenerative power of each wheel as follows:

$$P_{mot\_i} = \begin{cases} \eta_{mot\_i} \cdot T_{mot\_i} \cdot \omega_{mot\_i} & if \;\; T_{mot\_i} \cdot \omega_{mot\_i} \geq 0 \\ \dfrac{1}{\eta_{mot\_i}} \cdot T_{mot\_i} \cdot \omega_{mot\_i} & if \;\; T_{mot\_i} \cdot \omega_{mot\_i} < 0 \end{cases} \tag{2.7}$$

where $\eta_{mot\_i} = f\left(T_{mot\_i}, \omega_{mot\_i}\right)$

$$P_{mot} = \sum_{i=1}^{6} P_{mot\_i} \tag{2.8}$$

Battery dynamic model is written by battery power, open circuit voltage and internal resistance with initial status of charge (SOC) as follows:

$$SOC(t) = SOC_0 - \frac{1}{Q_{bat}} \int I_{bat} dt \tag{2.9}$$

$$where\ V_{bat} = V_{b,oc} - R_{int} I_{bat},\ I_{bat} = \frac{P_{bat}}{V_{bat}}$$

SOC_0 denotes initial SOC, Q_{bat} is battery capacity. R_{int} is initial resistance, $V_{b,oc}$ is battery open circuit voltage, V_{bat} is battery terminal voltage and I_{bat} is battery current.

2.3.4 Planer Model for Control System Design

Due to absence of test vehicle, the Trucksim dynamic model has been used to design control system and verify the performance of the proposed control system under developing process. It is difficult to develop control algorithm based on complicated vehicle dynamics. For control system design, simplified dynamic model should be adopted. The lateral/longitudinal translation and rotation of z-axis are considered.

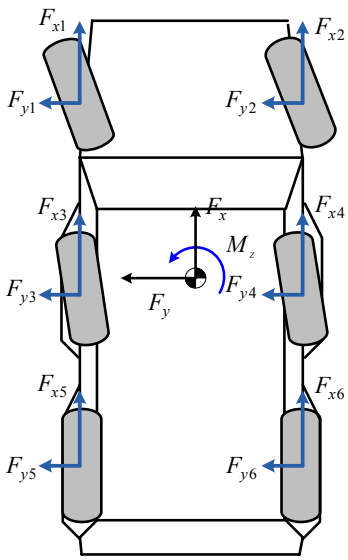

Figure 2.6 Planar model for 6WD/6WS vehicle

where, F_{xi} and F_{yi} represent the longitudinal and lateral tire force of i-th wheel respectively.

Taking derivative of the longitudinal and lateral vehicle velocity, state

equations can be obtained to design the proposed control algorithm. The longitudinal dynamics is related to lateral velocity and yaw rate. The amount of longitudinal tire forces generates longitudinal acceleration. In the same way, the lateral dynamics depends on longitudinal velocity and yaw rate. And the amount of lateral tire forces generates lateral acceleration of the vehicle. These relationships are written as follows:

$$\dot{v}_x = v_y \cdot \gamma + \frac{1}{m_s}\sum_{i=1}^{6} F_{xi} \tag{2.10}$$

$$\sum_{i=1}^{6} F_{xi} = F_{x1} + F_{x2} + F_{x3} + F_{x4} + F_{x5} + F_{x6}$$

$$\dot{v}_y = -v_x \cdot \gamma + \frac{1}{m_s}\sum_{i=1}^{6} F_{yi} \tag{2.11}$$

$$\sum_{i=1}^{6} F_{yi} = F_{y1} + F_{y2} + F_{y3} + F_{y4} + F_{y5} + F_{y6}$$

where, v_x denotes a longitudinal vehicle velocity and $\dot{v}_y$ is derivative of lateral velocity. γ is yaw rate at vehicle mass center point and m is vehicle mass.

Moment balance about the z axis yields the equation for the yaw dynamics as

$$\dot{\gamma} = \frac{1}{I_z} M_z \tag{2.12}$$

$$M_z = \frac{t}{2}\left(-F_{x1} + F_{x2} - F_{x3} + F_{x4} - F_{x5} + F_{x6}\right)$$
$$+ l_f\left(F_{y1} + F_{y2}\right) + l_m\left(F_{y3} + F_{y4}\right) - l_r\left(F_{y5} + F_{y6}\right)$$

where, I_z denotes moment of inertia of the vehicle and l_f, l_m and l_r are front, middle and rear wheel base which are distance from the vehicle mass center to each axles respectively.

For small slip angles, the lateral tire forces are given as follows:

$$F_{yf} = C_f \cdot \alpha_f,\ F_{ym} = C_m \cdot \alpha_m,\ F_{yr} = C_r \cdot \alpha_r \tag{2.13}$$

where, C_f, C_m and C_r denote cornering stiffness of front, middle and rear wheel respectively.

The lateral tire forces F_{yf}, F_{ym} and F_{yr} are proportional to the slip angle $\left(\alpha_{f,m,r}\right)$ for small slip angles. The slip angle of a tire is defined as the angle between the orientation of the tire and the orientation of the velocity vector of the wheel. Using average slip angles of the left and right tires, the slip angles of the front, middle and rear tires can be represented as follows:

$$\alpha_f = \delta_f - \frac{v_y + l_f \cdot \gamma}{v_x}$$
$$\alpha_m = \delta_m - \frac{v_y + l_m \cdot \gamma}{v_x} \tag{2.14}$$

$$\alpha_r = -\frac{v_y - l_r \cdot \gamma}{v_x}$$

where, δ_f, δ_m and δ_r represent steering angle of front, middle and rear wheel respectively.

For high speed stability of the vehicle, the longitudinal velocity should be controlled. Therefore, the derivative of the longitudinal velocity should be defined by lateral velocity and yaw rate. Substituting the expressions for the lateral tire forces into the equation (2.13) and (2.14), the dynamic state equations of vehicle model are rewritten as follows:

$$\dot{v}_x = v_y \cdot \gamma \tag{2.15}$$

$$\begin{aligned}\dot{v}_y = &-\left(\frac{2C_f + 2C_m + 2C_r}{m}\right)\cdot\frac{v_y}{v_x} \\ &-\left(v_x{}^2 + \frac{2C_f \cdot l_f + 2C_m \cdot l_m - 2C_r \cdot l_r}{m}\right)\cdot\frac{\gamma}{v_x} \\ &+\frac{2}{m}\left(C_f\delta_f + C_m\delta_m + C_r\delta_r\right)\end{aligned} \tag{2.16}$$

$$\begin{aligned}\dot{\gamma} = &-\left(\frac{2C_f \cdot l_f + 2C_m \cdot l_m - 2C_r \cdot l_r}{I_z}\right)\cdot\frac{v_y}{v_x} \\ &-\left(\frac{2C_f \cdot l_f{}^2 + 2C_m \cdot l_m{}^2 + 2C_r \cdot l_r{}^2}{I_z}\right)\cdot\frac{\gamma}{v_x} \\ &+\frac{2}{I_z}\left(C_f \cdot l_f \cdot \delta_f + C_m \cdot l_m \cdot \delta_m + C_r \cdot l_r \cdot \delta_r\right)\end{aligned} \tag{2.17}$$

Stability analysis of the proposed 6WD/6WS platform

The indirect method of Lyapunov is used to determine the local stability of the vehicle dynamic system without control systems. Consider the system

$$\dot{x} = f(x) \tag{2.18}$$

with $f(x', t) = 0$ for all $t \geq 0$. If the system is time-invariant, then the indirect method says that if the eigenvalues of

$$A_{system} = \left. \frac{\partial f(x)}{\partial x} \right|_{x=x'} \tag{2.19}$$

are in the open left half complex plane, then the origin is asymptotically stable. Equilibrium point x' (x_1', x_2', x_3') can be obtained using conditions of $f(x', t) = 0$ and satisfies

$$-a\frac{x_1'}{x_3'} - \left(x_3'^2 + b\right)\frac{x_2'}{x_3'} + M = 0 \tag{2.20}$$

$$-c\frac{x_1'}{x_3'} - d\frac{x_2'}{x_3'} + N = 0 \tag{2.21}$$

where, $a = \left(\frac{2C_f + 2C_m + 2C_r}{m} \right), b = \left(\frac{2C_f l_f + 2C_m l_m - 2C_r l_r}{m} \right)$

$$c = \left(\frac{2C_f l_f + 2C_m l_m - 2C_r l_r}{I_z} \right), d = \left(\frac{2C_f l_f^{\ 2} + 2C_m l_m^{\ 2} + 2C_r l_r^{\ 2}}{I_z} \right)$$

$$M = \frac{2}{m}\left(C_f \delta_f + C_m \delta_m + C_r \delta_r \right),$$
$$N = \frac{2}{I_z}\left(C_f L_f \delta_f + C_m L_m \delta_m + C_r L_r \delta_r \right)$$

Assuming that the sampling time is very short and derivative of velocity is zero, x_3' is set to constant value. Finally, x_1', x_2' is determined by equation (2.22) and (2.23).

$$x_1' = \frac{N}{c} x_3' - \frac{d}{c} x_2' \tag{2.22}$$

$$x_2' = \frac{1}{\left[\left(\frac{ad}{c} + b \right) \frac{1}{x_3'} + x_3' \right]} \left(-M + \frac{aN}{c} \right) \tag{2.23}$$

This system is regarded as time-invariant. Therefore, Jacobian matrix is defined on reasonable velocity range (1~100kph) and possible maximum steering angle (20 deg) as follows:

$$A_{system} = \left.\begin{bmatrix} \frac{\partial f_1}{\partial x_1} & \frac{\partial f_1}{\partial x_2} & \frac{\partial f_1}{\partial x_3} \\ \frac{\partial f_2}{\partial x_1} & \frac{\partial f_2}{\partial x_2} & \frac{\partial f_2}{\partial x_3} \\ \frac{\partial f_3}{\partial x_1} & \frac{\partial f_3}{\partial x_2} & \frac{\partial f_3}{\partial x_3} \end{bmatrix}\right|_{x=x'} \tag{2.24}$$

$$= \begin{bmatrix} -a\frac{1}{x_3'} & -c\frac{1}{x_3'} & x_2' \\ -\left(x_3'^2+b\right)\frac{1}{x_3'} & -d\frac{1}{x_3'} & x_1' \\ a\frac{x_1'}{x_3'^2}\dot{x}_3' - 2x_2' + \left(x_3'^2+b\right)\frac{x_2'}{x_3'^2}\dot{x}_3' & \frac{\dot{x}_3'}{x_3'^2}\left(cx_1'+dx_2'\right) & 0 \end{bmatrix}^T$$

Eigenvalues of Jacobian matrix A_{system} can be obtained as shown in table 2.3 and are in the open left half complex plane. And then the origin is asymptotically stable.

Table 2.3. Eigenvalues according to vehicle velocity

Eigen value	10 km/h	20 km/h	30 km/h	40 km/h	50 km/h	60 km/h	70 km/h	80 km/h	90 km/h
λ_1	-41.01	-20.70	-13.94	-10.51	-8.35	-6.76	-5.42	-4.02	-2.06
λ_2	-23.08	-11.31	-0.11	-0.25	-0.48	-0.84	-1.49	-1.99 + 0.71i	-2.53 + 1.40i
λ_3	- 0.0043	-0.03	-7.31	-5.25	-3.97	-3.06	-2.23	-1.99 - 0.71i	-2.53 - 1.40i

Increasing vehicle velocity, eigenvalues are changed based on dynamic features and still exist in the open left half complex plan. Trajectories of eigenvalues are expressed as shown in figure 2.7.

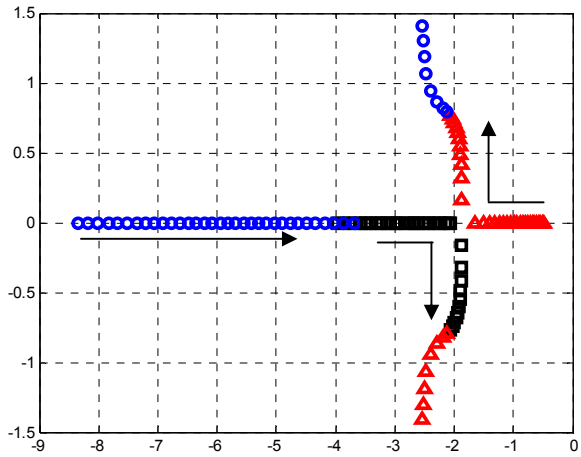

Figure 2.7 Eigenvalues according to increasing vehicle velocity

2.3.5 Bicycle Model for Direct Yaw Moment Control Design

Bicycle model has been used to design for direct yaw moment control (DYC) in many previous researches [Nagai99, Masao02, Toki01, An06]. The desired yaw rate can be easily and exactly calculated to guarantee yaw stability based on bicycle model through driver's steering intention. Assuming that vehicle velocity is constant and lateral velocity of the vehicle is very small, nonlinear planar model is replaced with bicycle model as follows:

$$\begin{aligned}\dot{\beta} = &-\left(\frac{2C_f + 2C_m + 2C_r}{m \cdot v_x}\right)\beta - \left(1 + \frac{2C_f \cdot l_f + 2C_m \cdot l_m - 2C_r \cdot l_r}{m \cdot v_x{}^2}\right)\gamma \\ &+ \frac{2}{m \cdot v_x}\left(C_f\delta_f + C_m\delta_m + C_r\delta_r\right)\end{aligned} \tag{2.25}$$

$$\begin{aligned}\dot{\gamma} = &-\left(\frac{2C_f l_f + 2C_m l_m - 2C_r l_r}{I_z}\right)\beta - \left(\frac{2C_f l_f{}^2 + 2C_m l_m{}^2 + 2C_r l_r{}^2}{I_z \cdot v_x}\right)\gamma \\ &+ \frac{2}{I_z v_x}\left(C_f l_f \delta_f + C_m l_m \delta_m + C_r l_r \delta_r\right)\end{aligned} \tag{2.26}$$

where, β denotes side slip angle which can be obtained by lateral velocity divided by longitudinal velocity. This bicycle model will be used to design the proposed yaw moment control algorithm in chapter 3.

Chapter 3

Integrated Driving Control Algorithm

The objective of the integrated driving control algorithm is to connect drivers with vehicles. The integrated driving control algorithm should be designed, because the proposed vehicle consists of steer-by-wire, throttle-by-wire and brake-by-wire system. As mentioned earlier, the integrated driving control algorithm comprises four parts: the desired dynamics, upper level control layer, lower level control layer and power management layer. The first part is description of the desired dynamics layer. It determines the desired longitudinal vehicle velocity and yaw rate through throttle, brake and steering wheel angle in order to satisfy the driver's intention. The second part is an upper level controller design for improvement of maneuverability and stability of the vehicle. The upper level control algorithm calculates the desired net force and yaw moment in order to follow the target velocity and yaw rate which are previously defined in the desired dynamics layer. Most importantly, the stability control algorithm is included to guarantee the lateral, yaw stability and rollover prevention in this layer. The G-vectoring and yaw

moment control methods has been developed. In the third part, the lower level control layer is explained and based on the control allocation methods which contains fixed-point, cascaded generalized inverse, interior point and weighted least square method. The fixed-point control allocation is adopted to implement real-time control system by analyzing computer simulations results. Control allocation algorithm is suitable for distribution of output wheel torque of over-actuated system. Finally, the fourth part is related to development of the power management algorithm that is based on the modified ECMS algorithm.

3.1 Desired Dynamics Layer

The desired dynamics layer determines the desired steering angle and velocity through driver's steering, throttle, and brake, commands. It is most important thing that the proposed desired dynamic algorithm satisfies the driver's intention. Determination of desired values should be based on the vehicle dynamics and driving features of conventional vehicles.

3.1.1 Desired steering angle determination

The desired steering angle needs to be calculated because the steering system is x-by-wire. The turning maneuver of the vehicle can be determined by the Ackerman steering method as shown in figure 3.1.

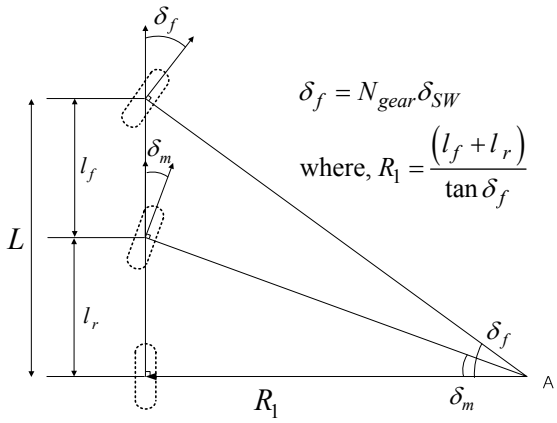

(a) Determination of steering angle and turning radius

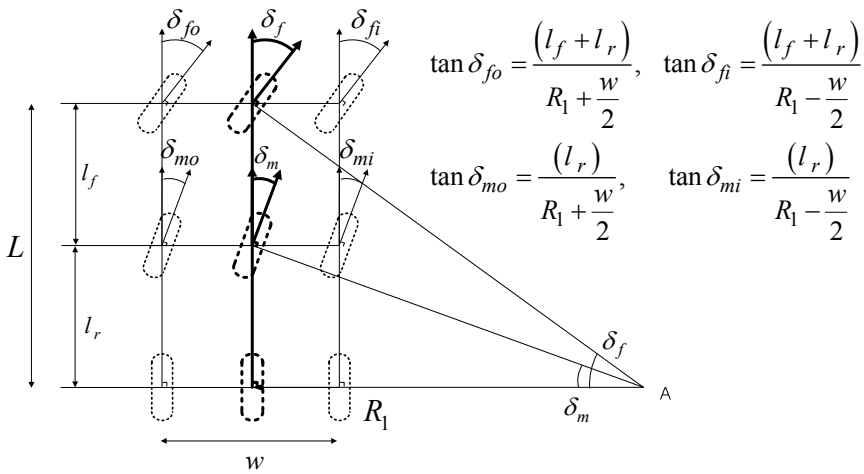

(b) Determination of steering angle of inner and outer wheel

Figure 3.1 Ackerman steering method

The Ackerman steering angles are determined as follows:

$$\tan\delta_{fo} = \frac{\left(l_f + l_r\right)}{R_1 + \frac{w}{2}}, \quad \tan\delta_{fi} = \frac{\left(l_f + l_r\right)}{R_1 - \frac{w}{2}},$$
$$\tan\delta_{mo} = \frac{\left(l_r\right)}{R_1 + \frac{w}{2}}, \quad \tan\delta_{mi} = \frac{\left(l_r\right)}{R_1 - \frac{w}{2}} \tag{3.1}$$
$$where\ R_1 = \frac{\left(l_f + l_r\right)}{\tan\delta_f}, \quad \delta_f = N_{gear}\delta_{SW}$$

where, N_{gear} denotes gear ratio of steering system. δ_{SW} is steering angle determined by driver. δ_{fo} and δ_{fi} represent outer and inner wheel of front wheels. The turning radius R_1 can be calculated by front steering angle and wheel base.

3.1.2 Desired velocity determination

The acceleration determination algorithm calculates the desired acceleration using throttle and brake pedal inputs. Figure 3.2 (a) shows the acceleration features of conventional vehicle. Drive (tractive) torque is proportional to the throttle input and is inversely proportional to vehicle velocity, whereas resistant torque increases with increases in vehicle velocity. The steady state velocity $\left(V_{ss}\right)$ is defined as when drive torque is identical to resistant torque. The desired velocity is set to the steady state velocity according to the throttle position as shown in figure 3.2 (b).

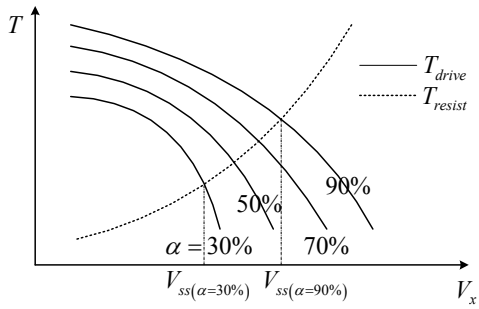

(a) Acceleration features of conventional vehicle

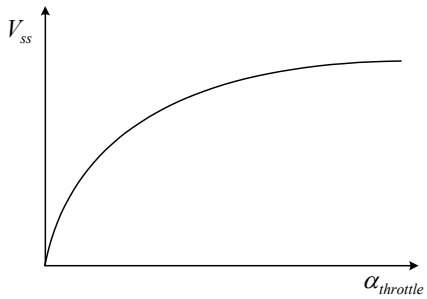

(b) Desired velocity according to throttle input

Figure 3.2 Desired velocity determination for drive condition

In braking situations, figure 3.3 shows the relation between brake pedal displacement and deceleration. The feature of this relation is not linear in order to apply actual hydraulic brake characteristics of conventional vehicle to the brake-by-wire system on proposed vehicle. The slope of the brake pedal-deceleration in the weak range is less than that of the strong range. The desired deceleration is determined by driver's brake pedal displacement command.

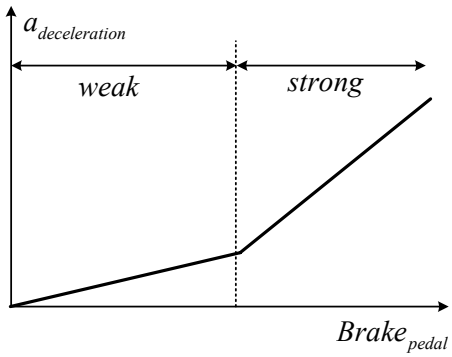

(a) Concept of braking strategy

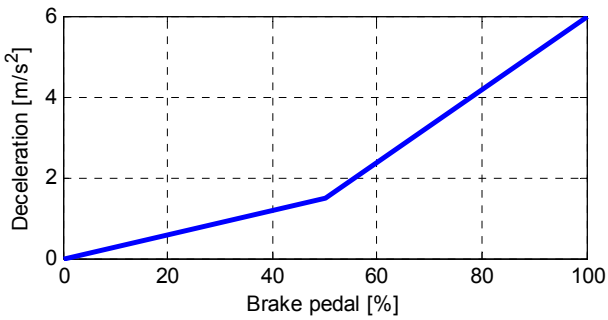

(b) Definition deceleration according to brake pedal

Figure 3.3 Desired deceleration determination for braking situation

The desired velocity for braking situation can be determined by initial velocity and the desired deceleration which defined by brake pedal position in continuous time domain.

$$v_{xd}(t) = v_{xi} + a_{deceleration} \cdot t \tag{3.2}$$

This algorithm should be implemented to real-time devices based on

discrete sampling time programming. In discrete time domain, the desired velocity can be calculated as follows :

$$v_{xd}\left(k+1\right)=v_{xd}\left(k\right)+a_{deceleration}\cdot\Delta T \tag{3.3}$$

where, $v_{xd}\left(1\right)=v_{x0}$, ΔT denotes sampling time.

3.2 Upper Level Control Layer

The upper level control layer consists of stability decision, yaw moment control, and speed control algorithms. The stability decision algorithm detects dangerous situations and determines the desired deceleration and the reference yaw rate necessary to guarantee vehicle stability. The yaw moment control algorithm applies a net yaw moment for tracking the reference yaw rate. The longitudinal required net force is calculated to follow the desired acceleration from the stability decision algorithm.

3.2.1 Stability decision algorithm

The stability decision algorithm is developed to enhance the performance of lateral yaw stability and rollover prevention. In driving conditions, intervention is not needed for vehicle stability. If the vehicle status is unstable, the stability decision algorithm determines the desired yaw rate and deceleration. Excessive lateral acceleration in turning maneuvers and small friction coefficient may give rise to serious problems with respect to roll and lateral motion. Therefore, the stability region is defined to ensure lateral stability and rollover prevention. Figure 3.4 illustrates the stable region with the limitation of acceleration on g-g diagram. The stable region is defined as the intersection of acceleration limitations which are related to rollover prevention $\left(a_{y\_ROM}\right)$ and lateral stability $\left(a_{y\_lateral\_stability}\right)$.

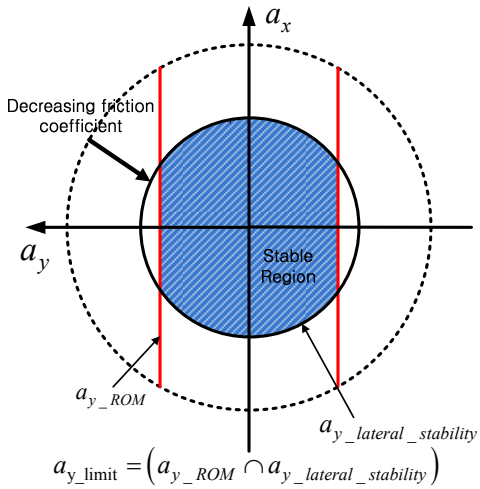

Figure 3.4 Definition of the stable region with respect to acceleration limitation on g-g diagram

Lateral acceleration for rollover mitigation is determined using the rollover index (RI) [Yoon09] defined as shown in figure 3.5.

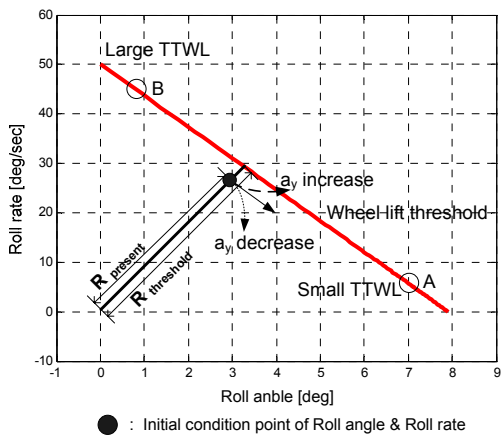

Figure 3.5 Important factors for rollover index calculation

Important factor that determines the RI from the present states of the vehicle are classified into three categories:

1) Measured states of roll angle and roll rate of the vehicle

: when the roll state of the vehicle is near the wheel lift threshold, the danger of rollover increases.

2) Measured lateral acceleration of the vehicle

: the trajectory of the roll state depends on the lateral acceleration may lead the trajectory of the vehicle toward the wheel-lift-threshold.

3) Time-to-wheel lift (TTWL)

: TTWL improves the accuracy of the RI. Although the roll states of the point A and B are on the wheel-lift threshold, the TTWL are different from each other. Compared to point B, the wheel lift is impending at point A, i.e., the time to wheel lift at point A is smaller than point B.

For instance, $RI \geq 1$ indicates wheel lift-off. RI can be calculated by using the measured lateral acceleration, a_y, the measured roll angle and roll rate, and their critical values as follows :

$$RI = \begin{cases} C_1\left(\dfrac{|\phi|\cdot\dot{\phi}_{th} + |\dot{\phi}|\cdot\phi_{th}}{\phi_{th}\cdot\dot{\phi}_{th}}\right) + C_2\left(\dfrac{|a_y|}{a_{y,c}}\right) + C_3\left(\dfrac{|\phi|}{\sqrt{\phi^2+\dot{\phi}^2}}\right), \\ \phi\cdot\left(\dot{\phi} - k_1\cdot\phi\right) > 0 \\ 0 \qquad\qquad\qquad\qquad\qquad\qquad , \ \phi\cdot\left(\dot{\phi} - k_1\cdot\phi\right) \le 0 \end{cases} \tag{3.4}$$

where, $C_1 + C_2 + C_3 = 1$ and C1, C2, and C3 are positive constants. ϕ_{th} and $\dot{\phi}_{th}$ are the critical values of the roll angle and roll rate, respectively, and $a_{y,c}$ is the critical value of the lateral acceleration. RI_{max} denotes the maximum rollover index and is design parameter. Using the RI, the maximum lateral acceleration for rollover prevention, a_{y_ROM}, can be calculated as follows:

$$a_{y\_ROM}\left(\phi,\ \dot{\phi}\right) = \frac{1}{C_2}\left(RI_{\max} - C_1\left(\frac{|\phi|\cdot\dot{\phi}_{th} + |\dot{\phi}|\cdot\phi_{th}}{\phi_{th}\cdot\dot{\phi}_{th}}\right) - C_3\left(\frac{|\phi|}{\sqrt{\phi^2+\dot{\phi}^2}}\right)\right)\cdot a_{y,c} \tag{3.5}$$

The desired acceleration and yaw rate are determined when the vehicle status becomes unstable. Activation conditions of the stable decision are written in table 3.1. When lateral acceleration measured by the acceleration sensor is less than the lateral acceleration limit, the desired acceleration is equal to the driver's acceleration command (a_{des}). On the other hand, when

the lateral acceleration is greater than the lateral acceleration limit, the desired acceleration (G_x) from the G-vectoring control is used to guarantee vehicle stability with respect to roll and lateral dynamics instead. When yaw rate error is greater than the defined threshold of yaw rate error, yaw rate control is activated.

Table 3.1 Activation condition of stability decision algorithm according to driving condition

Activation Condition	a_{xdes}	γ_{des}
$\left(\lvert a_y \rvert < a_{\text{y\_limit}}\right) \& \left(\lvert \gamma_d - \gamma \rvert < \gamma_{th}\right)$	*No Control*	*No Control*
$\left(\lvert a_y \rvert < a_{\text{y\_limit}}\right) \& \left(\lvert \gamma_d - \gamma \rvert > \gamma_{th}\right)$	*No Control*	*Active*
$\left(\lvert a_y \rvert > a_{\text{y\_limit}}\right) \& \left(\lvert \gamma_d - \gamma \rvert < \gamma_{th}\right)$	$G-vectoring\left(G_x\right)$	*No Control*
$\left(\lvert a_y \rvert > a_{\text{y\_limit}}\right) \& \left(\lvert \gamma_d - \gamma \rvert > \gamma_{th}\right)$	$G-vectoring\left(G_x\right)$	*Active*

3.2.2 G-vectoring control algorithm

G-vectoring control method has been developed to improve agility and stability of the vehicle [Yamakado10]. The control input of this method is identical to the proposed G-vectoring control in this paper as the longitudinal acceleration. However, control law is proportional to the lateral jerk of the vehicle for expert driving. In this paper, G-vectoring control (GVC) prevents excessive lateral acceleration below the predefined limitation of lateral acceleration. The aim of the GVC is to develop a stability control system for high speed driving conditions. Figure 3.6 illustrates the G-vectoring control strategy. When the vehicle starts cornering at section 1, lateral acceleration increases. At section 2, lateral acceleration drastically exceeds the limit of lateral acceleration. It is possible to cause very dangerous accidents in excessive lateral acceleration driving conditions. To guarantee stability of the 6WD/6WS vehicle, GVC applies longitudinal deceleration at section 3.

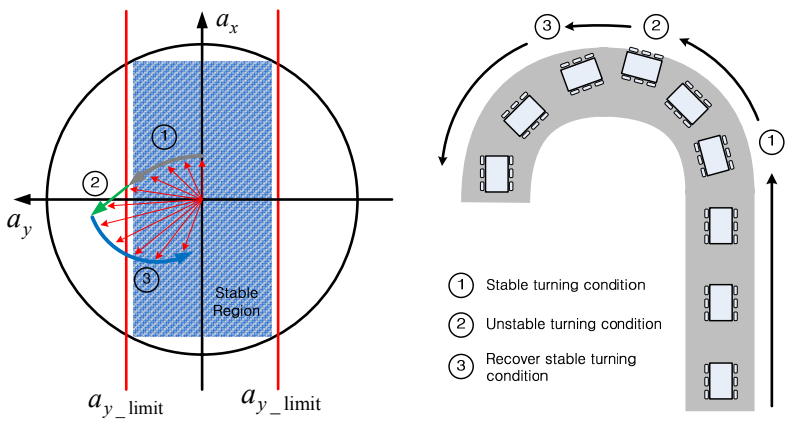

Figure 3.6 G-vectoring control strategy

The G-vectoring control algorithm determines the desired longitudinal deceleration in order to reduce excessive lateral acceleration that for lateral and rollover stability. Therefore, controllability should be performed to verify if it is possible to control the lateral acceleration of the vehicle through control input, the desired longitudinal deceleration. Due to nonlinear control system, controllability of this system cannot be verified directly. In this study, two methods have been used to investigate validity of the G-vectoring control algorithm. First, accessibility (local controllability) analysis based on Lie brackets method has been conducted. Also, controllability of linearized control system has been proved using Jacobian matrix which is defined as equation (2.24).

Accessibility of the G-vectoring control algorithm

The nonlinear vehicle dynamic model for the G-vectoring control used in this study can be represented as follows:

$$\dot{x} = f + d + gu \tag{3.6}$$

$$\frac{d}{dt}\underbrace{\begin{bmatrix} x_1 \\ x_2 \\ x_3 \end{bmatrix}}_{x} = \underbrace{\begin{bmatrix} -2\left(\dfrac{C_f + C_m + C_r}{m}\right)\cdot\dfrac{x_1}{x_3} - \left(x_3{}^2 + 2\dfrac{C_f l_f + C_m l_m - C_r l_r}{m}\right)\cdot\dfrac{x_2}{x_3} \\ -2\left(\dfrac{C_f l_f + C_m l_m - C_r l_r}{I_z}\right)\cdot\dfrac{x_1}{x_3} - 2\left(\dfrac{C_f l_f{}^2 + C_m l_m{}^2 + C_r l_r{}^2}{I_z}\right)\cdot\dfrac{x_2}{x_3} \\ x_1 x_2 \end{bmatrix}}_{f}$$

$$+\underbrace{\begin{bmatrix} \frac{2}{m}\left(C_f\delta_f + C_m\delta_m + C_r\delta_r\right) \\ \frac{2}{I_z}\left(C_f L_f\delta_f + C_m L_m\delta_m + C_r L_r\delta_r\right) \\ 0 \end{bmatrix}}_{d} + \underbrace{\begin{bmatrix} 0 \\ 0 \\ 1 \end{bmatrix}}_{g} u$$

where $x = \begin{bmatrix} v_y & \gamma & v_x \end{bmatrix}^T = \begin{bmatrix} x_1 & x_2 & x_3 \end{bmatrix}^T$, $g = \begin{bmatrix} 0 & 0 & 1 \end{bmatrix}^T$,

$d = function\left(\delta_f, \delta_m, \delta_r\right)$

For verifying controllability of G-vectoring control algorithm, two vector field $f(x)$ and $g(x)$ in $\Re^n$ need to be considered. Then the Lie bracket operation generates a new vector field:

$$[f,g] = \frac{\partial g}{\partial x} f - \frac{\partial f}{\partial x} g = -\begin{bmatrix} -A\frac{1}{x_3} & -C\frac{1}{x_3} & x_2 \\ -\left(x_3^2 + B\right)\frac{1}{x_3} & -D\frac{1}{x_3} & x_1 \\ -2x_2 & 0 & 0 \end{bmatrix} \cdot \begin{bmatrix} 0 \\ 0 \\ 1 \end{bmatrix} \qquad (3.7)$$

$$= \begin{bmatrix} -x_2 & -x_1 & 0 \end{bmatrix}^T$$

where, $\frac{\partial f}{\partial x} = \begin{bmatrix} \frac{\partial f_1}{\partial x_1} & \frac{\partial f_2}{\partial x_1} & \frac{\partial f_3}{\partial x_1} \\ \frac{\partial f_1}{\partial x_2} & \frac{\partial f_2}{\partial x_2} & \frac{\partial f_3}{\partial x_2} \\ \frac{\partial f_1}{\partial x_3} & \frac{\partial f_2}{\partial x_3} & \frac{\partial f_3}{\partial x_3} \end{bmatrix} = \begin{bmatrix} -a\frac{1}{x_3} & -c\frac{1}{x_3} & x_2 \\ -\left(x_3^2 + b\right)\frac{1}{x_3} & -d\frac{1}{x_3} & x_1 \\ -2x_2 & 0 & 0 \end{bmatrix}$, $\frac{\partial g}{\partial x} = 0$

$$a=\left(\frac{2C_f+2C_m+2C_r}{m}\right),\ b=\left(\frac{2C_f l_f+2C_m l_m-2C_r l_r}{m}\right)$$

$$c=\left(\frac{2C_f l_f+2C_m l_m-2C_r l_r}{m}\right),\ d=\left(\frac{2C_f {l_f}^2+2C_m {l_m}^2+2C_r {l_r}^2}{I_z}\right)$$

$$M=\frac{2}{m}\left(C_f\delta_f+C_m\delta_m+C_r\delta_r\right), N=\frac{2}{I_z}\left(C_f L_f\delta_f+C_m L_m\delta_m+C_r L_r\delta_r\right)$$

Also, higher order Lie brackets can be defined:

$$\left[ad_f^2,g\right]=\left[f,[f,g]\right]=\frac{\partial[f,g]}{\partial x}f-\frac{\partial f}{\partial x}[f,g] \tag{3.8}$$

$$=\begin{bmatrix}0&-1&0\\-1&0&0\\0&0&0\end{bmatrix}\begin{bmatrix}-a\cdot\frac{x_1}{x_3}-b\cdot\frac{x_2}{x_3}+M\\-c\cdot\frac{x_1}{x_3}-d\cdot\frac{x_2}{x_3}+N\\x_1x_2\end{bmatrix}-\begin{bmatrix}-a\frac{1}{x_3}&-c\frac{1}{x_3}&x_2\\-\left(x_3^2+b\right)\frac{1}{x_3}&-d\frac{1}{x_3}&x_1\\-2x_2&0&0\end{bmatrix}\begin{bmatrix}-x_2\\-x_1\\0\end{bmatrix}$$

$$=\begin{bmatrix}c\cdot\frac{x_1}{x_3}+d\cdot\frac{x_2}{x_3}-N\\a\cdot\frac{x_1}{x_3}+b\cdot\frac{x_2}{x_3}-M\\0\end{bmatrix}-\begin{bmatrix}a\frac{x_2}{x_3}+c\frac{x_1}{x_3}\\\left(x_3^2+b\right)\frac{x_2}{x_3}+d\frac{x_1}{x_3}\\2x_2^2\end{bmatrix}=\begin{bmatrix}\left(-a+d\right)\frac{x_2}{x_3}-N\\\left(a-d\right)\cdot\frac{x_1}{x_3}-x_2x_3-M\\-2x_2^2\end{bmatrix}$$

If controllability condition, accessibility distribution $C_{accessibility}$, spans n space, where n is the rank of $C_{accessibility}$ is defined by:

$$C_{\text{accessibility}} = \left[g, [f, g], [ad_f^2, g] \right] = \left. \begin{bmatrix} 0 & -x_2 & (-a+d)\dfrac{x_2}{x_3} - N \\ 0 & -x_1 & (a-d)\cdot\dfrac{x_1}{x_3} - x_2 x_3 - M \\ 1 & 0 & -2x_2^2 \end{bmatrix} \right|_{x=x'} \tag{3.9}$$

Because rank of this system is full, the proposed control system is accessible or locally controllable about equilibrium point x' that was previously defined as equation (2.22) and (2.23) in chapter 2.

Controllability of the G-vectoring control algorithm

The linearization system matrix of nonlinear dynamic model is used to verify controllability of the G-vectoring control algorithm and was previously defined as equation (2.24), Jacobian matrix, in chapter 2. Consider the linearized control system around the equilibrium point x'.

$$\dot{x} = A_{system} x + Bu \tag{3.10}$$

where,

$$A_{system} = \left.\frac{\partial f}{\partial x}\right|_{x=x'} = \left.\begin{bmatrix} \frac{\partial f_1}{\partial x_1} & \frac{\partial f_1}{\partial x_2} & \frac{\partial f_1}{\partial x_3} \\ \frac{\partial f_2}{\partial x_1} & \frac{\partial f_2}{\partial x_2} & \frac{\partial f_2}{\partial x_3} \\ \frac{\partial f_3}{\partial x_1} & \frac{\partial f_3}{\partial x_2} & \frac{\partial f_3}{\partial x_3} \end{bmatrix}\right|_{x=x'} = \left.\begin{bmatrix} -a\frac{1}{x_3} & -c\frac{1}{x_3} & x_2 \\ -\left(x_3^2+b\right)\frac{1}{x_3} & -d\frac{1}{x_3} & x_1 \\ -2x_2 & 0 & 0 \end{bmatrix}\right|_{x=x'}$$

, $B = g = \begin{bmatrix} 0 & 0 & 1 \end{bmatrix}^T$

The controllability matrix, $C_{controllability}$, can be obtained as follows :

$$C_{controllability} = \begin{bmatrix} B & A_{system}B & A_{system}{}^2B \end{bmatrix} \tag{3.11}$$

$$= \left.\begin{bmatrix} 0 & x_2 & -a\frac{x_2}{x_3} - c\frac{x_1}{x_3} \\ 0 & x_1 & -\left(x_3^2+b\right)\frac{x_2}{x_3} - d\frac{x_1}{x_3} \\ 1 & 0 & -2x_2^2 \end{bmatrix}\right|_{x=x'}$$

Rank of the matrix, $C_{controllability}$, in equation (3.11) is full. If a nonlinear system is first-order controllable at the equilibrium point x', it is locally controllable. Therefore, this control system is controllable at the equilibrium point x'.

Design of G-vectoring control algorithm based on sliding control method

The dynamic surface control method is used to design to G-vectoring control algorithm. The sliding surface is defined by lateral acceleration error as follows :

$$S_1 = \dot{x}_{1d} - |\dot{x}_1| \tag{3.12}$$

After taking a derivative of S_1 in equation (3.12), let $\dot{S}_1 \le -\eta_1 S_1$ in equation where η_1 is controller gain based on perfect dynamic system in order to make S_1 converge to zero.

$$\dot{S}_1 = \dot{x}_{1d} - \frac{d}{dt}|\dot{x}_1| = \dot{x}_{1d} - \frac{\dot{x}_1}{|\dot{x}_1|}\cdot\frac{d}{dt}\dot{x}_1 = \dot{x}_{1d} - \mathrm{sgn}(\dot{x}_1)\cdot\frac{d}{dt}\dot{x}_1 \tag{3.13}$$

$$= \dot{x}_{1d} - \mathrm{sgn}(\dot{x}_1)\cdot\left\{-A\cdot\frac{d}{dt}\left(\frac{x_1}{x_3}\right) - \frac{d}{dt}(x_2\cdot x_3) - B\cdot\frac{d}{dt}\left(\frac{x_2}{x_3}\right)\right\}$$

$$= \dot{x}_{1d} - \mathrm{sgn}(\dot{x}_1)\cdot\left\{\left(A\cdot\frac{1}{x_3^{\,2}}\cdot x_1 + B\cdot\frac{1}{x_3^{\,2}}\cdot x_2 - x_2\right)\dot{x}_3 - \frac{A}{x_3}\cdot\dot{x}_1 - x_3\cdot\dot{x}_2 - \frac{B}{x_3}\cdot\dot{x}_2\right\}$$

$$= -\eta_1|S_1|$$

$$where\ A = \left(\frac{2C_f + 2C_m + 2C_r}{m}\right),\ B = \left(\frac{2C_f l_f + 2C_m l_m - 2C_r l_r}{m}\right)$$

The total mass of the proposed target vehicle can be changed to install other devices for weapon, detection and defense systems. There is a difference between dynamic model and real dynamic system. Also, lateral dynamics should contain turning maneuvers that is generated by steering angle dominantly. Due to steer-by-wire control system, steer angle errors (e_δ) are considered and defined as disturbance uncertainty. In general, control gain margin (b) is useful for adaptation of control gain for consideration of various driving load conditions such as climbing and descent roads. In this paper, assumed that driving conditions are flat roads, control gain margin is set to 1. To design the control gain (K_1) with consideration of model, disturbance uncertainty and gain margin, feasible range of the control gain can be obtained as follows:

$$K_1 \geq b^{-1}\hat{b}\left(F+\eta_1+\kappa\right)+\left|b^{-1}\hat{b}-1\right|\cdot\left|-\hat{f}_1+\dot{x}_{1d}\right| \tag{3.14}$$

where $\left|\hat{f}_1-f_1\right|$

$$=\left|\left(\frac{2}{\hat{m}}-\frac{2}{m}\right)\left\{-\left(C_f+C_m+C_r\right)\cdot\frac{x_1}{x_3}-\left(C_f l_f+C_m l_m-C_r l_r\right)\cdot\frac{x_2}{x_3}\right\}\right|\leq F_1$$

$$\left|\hat{d}_1-d_1\right|=2\left|C_f\left(\frac{\hat{\delta}_f}{\hat{m}}-\frac{\delta_f}{m}\right)+C_m\left(\frac{\hat{\delta}_m}{\hat{m}}-\frac{\delta_m}{m}\right)+C_r\left(\frac{\hat{\delta}_r}{\hat{m}}-\frac{\delta_r}{m}\right)\right|\leq\kappa$$

$$\hat{m}=\sqrt{m_{\min}\cdot m_{\max}},\ \hat{\delta}=\sqrt{\left(\delta+e_\delta\right)\left(\delta-e_\delta\right)},\ \hat{C}_i=\sqrt{C_{i\max}\cdot C_{i\min}}$$
$$\left(i=f,m,r\right)$$

Bounded parameter (F_1) related to model error can be calculated by nominal vehicle mass ($\hat{m}$), cornering stiffness, wheel base, vehicle velocity, yaw rate and lateral velocity.

Table 3.2 Nominal values and bounded parameters for gain calculation of sliding control

Vehicle Parameters	values	Nominal Parameters	values
Minimum Vehicle Mass (m_{min})	7200 [kg]	Nominal Vehicle Mass ($\hat{m}$)	8270.4 [kg]
Maximum Vehicle Mass (m_{max})	9500 [kg]		
Minimum Vehicle Inertia (Iz_{min})	33573 [kgm^2]	Nominal Vehicle Inertia ($\hat{I}_z$)	38564 [kgm^2]
Maximum Vehicle Mass (Iz_{max})	44297 [kgm^2]		
Min Cornering Stiffness ($C_{i\min}$)	125380 [N/rad]	Nominal Cornering Stiffness ($\hat{C}_i$)	174120 [N/rad]
Max Cornering Stiffness ($C_{i\max}$)	241800 [N/rad]		
Steering angle error (e_δ)	0.2 [deg]		
Required Driving Conditions	**Specifications**	**Bounded Parameters**	**Specifications**
Maximum vehicle velocity	100 [km/h]	F_1 (model error)	7.1465
Maximum vehicle yaw rate	30 [deg/s]	κ (disturbance error)	2.5615
Maximum lateral velocity	5 [km/h]		

The dynamics f_1 is not exactly known, but can be estimated as $\hat{f}_1$. The estimation error is assumed to be bounded by F. The disturbance error is also bounded by κ. Related parameters and conditions are expressed as shown in table 3.2 in detail.

The control law related to the desired longitudinal acceleration (G_x) is defined by longitudinal, lateral velocity and yaw rate, lateral acceleration, yaw angular acceleration and derivative of desired lateral acceleration as follows:

$$u = G_x = \frac{1}{h}\left\{\dot{x}_{1d} + \operatorname{sgn}\left(\dot{x}_1\right)\left(\frac{a'}{x_3}\dot{x}_1 + x_3\dot{x}_2 + \frac{b'}{x_3}\dot{x}_2\right) + K_1 sat\left(\frac{S_1}{\Phi_1}\right)\right\} - x_1 x_2 \quad (3.15)$$

$$where,\ h = \operatorname{sgn}\left(\dot{x}_1\right)\left(\frac{a'}{x_3^{\ 2}}x_1 + \frac{b'}{x_3^{\ 2}}x_2 - x_2\right)$$

$$a' = \left(\frac{2\hat{C}_f + 2\hat{C}_m + 2\hat{C}_r}{\hat{m}}\right),\ b' = \left(\frac{2\hat{C}_f l_f + 2\hat{C}_m l_m - 2\hat{C}_r l_r}{\hat{m}}\right)$$

, Φ_1 is control boundary which is determined to eliminate high frequency chattering.

3.2.3 Yaw moment control algorithm

In many studies on conventional vehicles, a bicycle model is used to define the desired dynamic model as equation (2.25) and (2.26) in chapter 2. Assuming that vehicle velocity variation is small during the yaw moment control, the 6WD/6WS vehicle model is simply defined as linearized bicycle model as follows:

$$\begin{bmatrix} \dot{\beta} \\ \dot{\gamma} \end{bmatrix} = \begin{bmatrix} a_{11} & a_{12} \\ a_{21} & a_{22} \end{bmatrix} \begin{bmatrix} \beta \\ \gamma \end{bmatrix} + \begin{bmatrix} b_{11} \\ b_{21} \end{bmatrix} \delta_f + \begin{bmatrix} b_{12} \\ b_{22} \end{bmatrix} \delta_m \tag{3.16}$$

$$= \begin{bmatrix} a_{11} & a_{12} \\ a_{21} & a_{22} \end{bmatrix} \begin{bmatrix} \beta \\ \gamma \end{bmatrix} + \begin{bmatrix} b_{11} + b_{12}\left(\dfrac{L_m + L_r}{L}\right) \\ b_{21} + b_{22}\left(\dfrac{L_m + L_r}{L}\right) \end{bmatrix} \delta_f$$

where, $a_{11} = \dfrac{-2\left(C_f + C_m + C_r\right)}{mv_x}$, $a_{12} = \dfrac{-2\left(l_f C_f + l_m C_m - l_r C_r\right)}{mv_x{}^2} - 1$

$$a_{21} = \frac{-2\left(l_f C_f + l_m C_m - l_r C_r\right)}{I_z} \quad , \quad a_{22} = \frac{-2\left(l_f{}^2 C_f + l_m{}^2 C_m - l_r{}^2 C_r\right)}{I_z v_x}$$

$$b_{11} = \frac{2C_f}{mv_x} \ , b_{12} = \frac{2C_m}{mv_x}, b_{13} = \frac{2C_r}{mv_x},$$
$$b_{21} = \frac{2l_f C_f}{I_z}, b_{22} = \frac{2l_m C_m}{I_z}, b_{23} = \frac{2l_r C_r}{I_z} \ .$$

The state β is called side slip angle and can be obtained as the lateral velocity divided by the longitudinal velocity. The gain (k) of the steady state

yaw rate (γ_{ss}) can be obtained by excluding transient terms from the bicycle dynamic model as in equation (3.16) and by substituting side slip angle for yaw rate. It is given as follows:

$$\frac{\gamma_{ss}}{\delta_f} = k = \frac{a_{22}\left(b_{21} + b_{22}\frac{l_m + l_r}{L}\right) - a_{21}\cdot\left(b_{11} + b_{12}\frac{l_m + l_r}{L}\right)}{\left(a_{12}a_{21} - a_{11}a_{22}\right)} \tag{3.17}$$

A desired yaw rate is determined by k and a first-order transfer function expressed as the time constant.

$$\gamma_{des} = \frac{k}{1 + \tau_{yaw}s}\delta_f \tag{3.18}$$

where, time constant τ_{yaw} can be experimentally determined by comparing between measured and calculated yaw rate from the bicycle model as shown in figure 3.7.

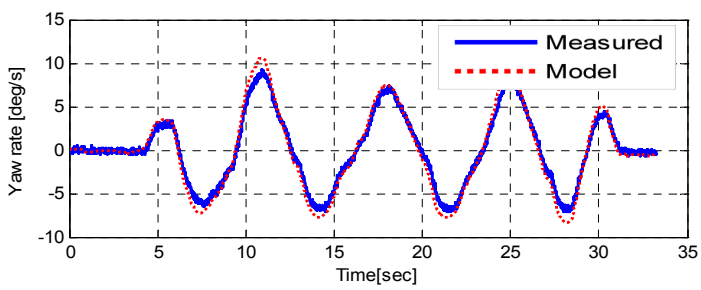

Figure 3.7 Validation for desired yaw rate model design

Assuming constant lateral velocity, equation (3.17) provides a theoretical limit to the yaw rate that is achievable at the current friction condition between tire and road. Therefore, the desired reference yaw rate is reasonably constrained by the physical limit of tire-road friction as follows :

$$\left|\gamma_{des}\right| \le \frac{\mu g}{v_x} \tag{3.19}$$

where $\left|ma_y\right| = \left|mv_x\gamma_{des}\right| \le m\mu g = \left|\sum_{i=1}^{6}\left(\mu_i F_{zi}\right)\right|$

The friction coefficient, μ cannot measure directly using sensors or measurement devices. Therefore, the friction circle information needs to be used to obtain the friction circle information. The friction circle estimation will be explained in chapter 4.

To track the proposed desired yaw rate, a yaw stability control algorithm is designed based on a 2 degree of freedom (D.O.F.) bicycle model. The yaw stability controller generates a net yaw moment in order to stabilize the yaw behavior of a vehicle. The equation of yaw motion is:

$$\dot{\gamma} = -\frac{2\left(C_f l_f + C_m l_m - C_r l_r\right)}{I_z}\beta - \frac{2\left(C_f l_f^2 + C_m l_m^2 + C_r l_r^2\right)}{I_z v_x}\gamma \tag{3.20}$$
$$+\frac{2C_f l_f}{I_z}\delta_f + \frac{2C_m l_m}{I_z}\delta_m + \frac{M_z}{I_z}$$

Sliding surface is defined as yaw rate error, which is the difference between

the actual yaw rate and the desired one:

$$s_2 = \gamma - \gamma_{des}. \tag{3.21}$$

The control objective is to keep the scalar s_2 at zero which can be achieved by choosing a control law satisfying the following sliding condition.

$$\frac{1}{2}\frac{d}{dt}s_2{}^2 \le -\eta_2 |s_2| \text{ where, } \eta_2 > 0 \tag{3.22}$$

The sliding control law is obtained from the desired yaw moment:

$$M_z = 2\hat{I}_z \left\{ \frac{\left(\hat{C}_f l_f + \hat{C}_m l_m - \hat{C}_r l_r\right)}{\hat{I}_z}\beta + \frac{\left(\hat{C}_f l_f^2 + \hat{C}_m l_m^2 + \hat{C}_r l_r^2\right)}{\hat{I}_z v_x}\gamma \right.$$
$$\left. -\frac{\hat{C}_f l_f}{\hat{I}_z}\hat{\delta}_f - \frac{\hat{C}_m l_m}{\hat{I}_z}\hat{\delta}_m - K_2 \cdot sat\left(\frac{s_2}{\Phi_2}\right) \right\} \tag{3.23}$$

where Φ_2 is control boundary which is determined to eliminate high frequency chattering. Assuming that the nominal value of yaw moment of inertia ($\hat{I}_z$) is the geometric mean of the upper and lower bounds of moment of inertia of the vehicle, $I_{z,\min}$ and $I_{z,\max}$, as follows :

$$\hat{I}_z = \sqrt{I_{z,\min} \cdot I_{z,\max}} \tag{3.24}$$

The estimation error is bounded by F_2. To design the control gain (K_2) with consideration of model, feasible range of the control gain can be obtained as follows:

$$K_2 \geq \left(F_2 + \eta_2\right) \tag{3.25}$$

Nominal cornering stiffness and steering error have been considered to design the yaw rate control algorithm. And $\hat{C}_i$ and $\hat{\delta}_i$ (*i=f,m,r*) are defined by equation (3.14) in G-vectoring section. F_2 can be calculated as 11.1270 using $\hat{I}_z$, $\hat{C}_i$ and $\hat{\delta}_i$ in table 3.2.

Performance Verification based on Frequency Analysis

Performance verification based on frequency analysis has been conducted using linearized control system as shown in figure 3.8. Yaw moment control consists of vehicle dynamic model P1, P2, sliding controller C1, motor controller C2 and desired vehicle dynamic model D.

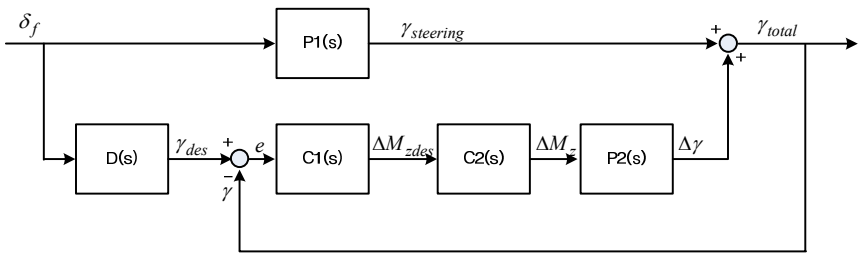

Figure 3.8 Function block diagram of yaw moment control system

Transfer functions and parameters are defined as shown in table 3.3. Steering model transfer function (P1) and desired dynamic model (D) calculate yaw rate and the desired yaw rate of the 6WD/6WS vehicle using steering angle input based on steady state bicycle model. Yaw moment model (P2) determines additional yaw rate using calculated additional yaw moment. Sliding controller for direct yaw moment control (C1) is linearized and transfer function can be defined as sliding gain and boundary layer. Transfer function of motor controller (C2) contains motor dynamics. This control system can be formulated as

$$G(s)=\frac{\gamma_{total}(s)}{\delta_f(s)}=\frac{P_1+DC_1C_2P_2}{1+C_1C_2P_2} \tag{3.26}$$

Table 3.3 Transfer function definition of yaw moment control system

Function Block	Input	Output	Transfer Function	Parameters
P1 – Vehicle Dynamic Model	Steering angle	Yaw rate	$\gamma_{steering}=\frac{k_{P1}}{\tau_{P1}\cdot s+1}\cdot\delta_f$	τ_{P1} : system delay $k_{P1}=3.328$: steady state yaw rate gain
P2 – Vehicle Dynamic Model	Additional moment	Additional yaw rate	$\Delta\gamma=\frac{1}{I_z\cdot s}\cdot\Delta M_z$	
C1 – Sliding Controller	Sliding surface	Additional desired yaw rate	$\Delta M_{zdes}=\left(\frac{I_z\cdot k_{sliding}}{\Phi}\right)\cdot e$	$k_{sliding}=5$: sliding gain $\Phi=1$: boundary layer
C2 – Motor Controller	Desired yaw moment	Yaw Moment	$\Delta M_z=\frac{1}{\tau_{C2}\cdot s+1}\cdot\Delta M_{zdes}$	$\tau_{C2}=0.01$
D – Desired Vehicle Dynamic Model	Steering angle	Desired yaw rate	$\frac{k_D}{\tau_D\cdot s+1}$	$\tau_D=0.3$ $k_D=3.328$:steady state desired yaw rate gain

Vehicle dynamic and control systems have been defined as transfer function based on Laplace transformation method. Substituting transfer functions such as P1, P2, C1, C2 and D, the overall transfer function $G(s)$ can be calculated to obtain the poles and zeros of the linearized control system.

$$G(s)=\frac{\dfrac{k_{P1}}{\tau_{P1}\cdot s+1}+\dfrac{k_D}{\tau_D\cdot s+1}\cdot\dfrac{I_z\cdot k_{sliding}}{\Phi}\cdot\dfrac{1}{\tau_{C2}\cdot s+1}\cdot\dfrac{1}{I_z\cdot s}}{1+\dfrac{I_z\cdot k_{sliding}}{\Phi}\cdot\dfrac{1}{\tau_{C2}\cdot s+1}\cdot\dfrac{1}{I_z\cdot s}} \tag{3.27}$$

In the case of dangerous driving condition such as obstacle avoidance and severe lane change, a rate of steering input increases. Increasing frequency of sinusoidal steering input, difference of yaw rate response between linear and real vehicle dynamic model becomes large. Because tire model used to linear bicycle model does not consider saturation of tire forces. Therefore, due to saturated lateral tire force in real environment, time delay should be considered to verify accurate performance of the yaw moment control algorithm. Time constant of linear vehicle dynamic model with first order transfer function is determined to reflect the response of non linear dynamic model as illustrated in figure 3.9.

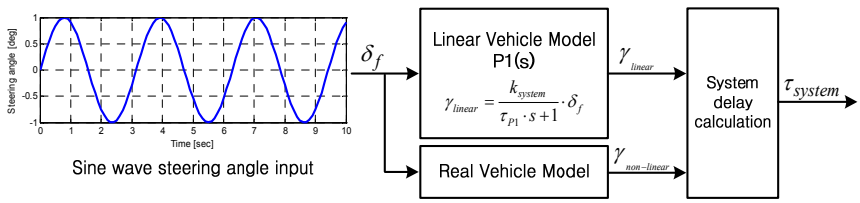

Figure 3.9 System delay determination illustration

Vehicle velocity is 60 km/h for frequency analysis. When frequency of sinusoidal steering input is increasing, time constant of system delay, τ_{P1}, increases quadratically as shown in figure 3.10.

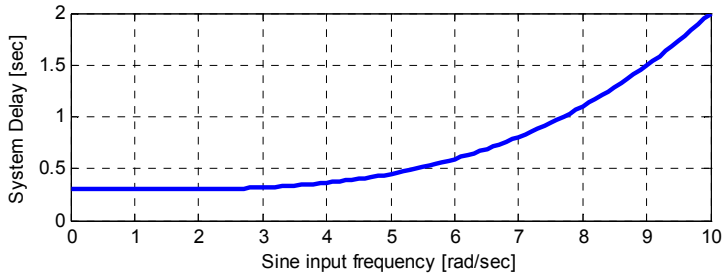

Figure 3.10 System delay according to sinusoidal steering input frequency

Assuming that frequency of steering input is 7 rad/s for avoiding dangerous situations, system delay of linear vehicle dynamic model τ_{P1} can be defined as 0.8 for verification of frequency analysis. Using the determined system delay, the transfer function of the yaw moment control system is written as

$$G(s) = \frac{0.00009984s^4 + 0.0203s^3 + 1.198s^2 + 16.81s + 16.64}{0.000024s^5 + 0.00491s^4 + 0.2741s^3 + 2.375s^2 + 6.55s + 5} \quad (3.28)$$

Poles of this control system represent features of dynamic response and system stability. It is necessary that poles are located in left half plane for verifying the system stability. Table 3.4 shows poles of the yaw moment control system. It is shown that all of poles are negative values.

Table 3.4 Poles of the yaw moment control system

Pole	*Value*
λ_1	-100.00
λ_2	-94.7214

λ_3	-5.2786
λ_4	-3.3333
λ_5	-1.2500

Figure 3.11 is root-locus of the proposed control system and shows that poles are located and zeros are located in left half plane. From this result, the proposed control system is stable.

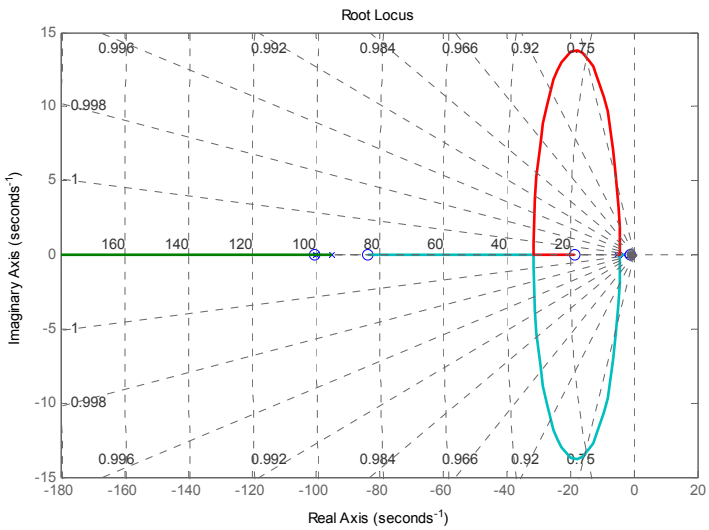

Figure 3.11 Root-locus of the yaw moment control system

Based on Bode analysis method, bandwidth of the proposed control system is greater than that of no control case as shown in figure 3.12. This result shows that vehicle stability can be guaranteed according to severe steering input for avoiding dangerous situations in yaw moment control case.

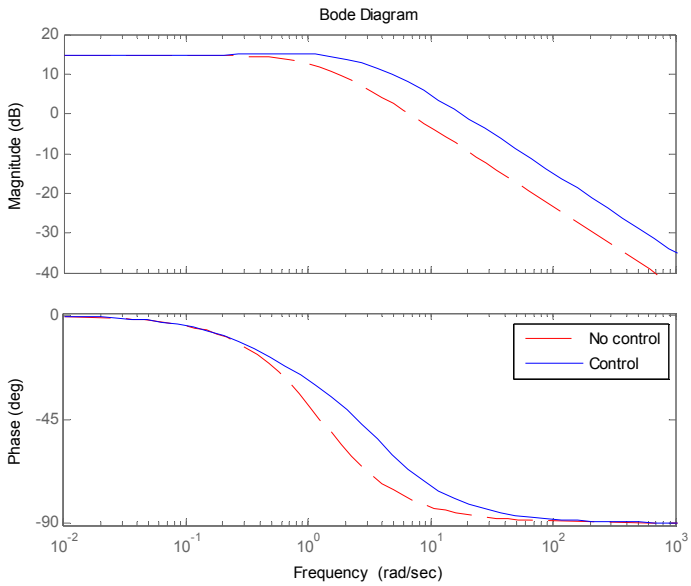

Figure 3.12 Frequency analysis of yaw moment control

3.2.4 Speed Control Algorithm

A speed control algorithm has been designed to track the desired velocity which is determined to satisfy the driver's intention and to follow the desired longitudinal acceleration in order to guarantee the vehicle stability based on the G-vectoring control (GVC) algorithm. The speed control algorithm consists of the velocity and acceleration tracking algorithm. The desired longitudinal net force based on the velocity tracking algorithm, F_{xd_vel}, is determined. Also, the desired longitudinal net force based on the acceleration tracking algorithm, F_{xd_accel}, is calculated to execute the G-vectoring control in dangerous situations. From the GVC, stability decision signal choose the desired longitudinal net force from the desired dynamics or the G-vectoring control algorithm. The speed control algorithm block diagram is illustrated in figure 3.13.

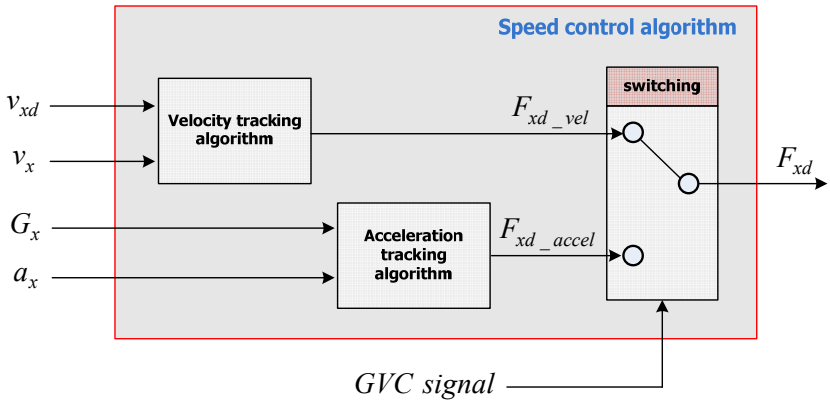

Figure 3.13 Block diagram of the speed control algorithm

Velocity tracking algorithm

A velocity tracking control algorithm is designed to calculate the desired longitudinal net force in order to force the vehicle to follow the desired velocity. The desired longitudinal net force for yielding the desired velocity can be calculated based on the sliding mode control method using a planar dynamic model defined in equation (2.1). Longitudinal dynamics is written as follows:

$$\dot{v}_x = v_y \cdot \gamma + \frac{1}{m} F_{xd} \tag{3.29}$$

The objective of the velocity tracking algorithm is minimizing the speed error. Therefore, the sliding surface and conditions are defined as follows:

$$s_3 = v_x - v_{xd} \tag{3.30}$$

$$\frac{1}{2}\frac{d}{dt}s_3^2 = s_3\dot{s}_3 \le -\eta_3 \left|s_3\right| \tag{3.31}$$

where, η_3 is positive constant

The desired longitudinal net force can be obtained by equation (3.29) and sliding control gain (K_3) has to be greater than η_3. Φ_3 is defined to eliminate high frequency chattering.

$$F_{xd} = \hat{m}\left(-v_y \cdot \gamma + \dot{v}_{xd} - K_3 sat\left(\frac{s_3}{\Phi_3}\right)\right) \tag{3.32}$$

where, $K_3 \geq \eta_3$

Acceleration tracking algorithm

An acceleration tracking algorithm is designed to calculate the desired longitudinal net force in order to force the vehicle to follow the desired acceleration from the G-vectoring algorithm for vehicle roll stability. The desired longitudinal net force for yielding the desired longitudinal acceleration can be calculated based on the PID control method in order to regulate the acceleration error. The desired longitudinal net force is determined as follows:

$$F_{xd} = \left[K_P\left(G_x - a_x\right) + K_I\int\left(G_x - a_x\right)dt + K_D\frac{d}{dt}\left(G_x - a_x\right)\right] \tag{3.33}$$

Switching algorithm

In general, the GVC signal is zero during stable driving conditions. The desired longitudinal net force from the desired dynamics is chosen. If vehicle rollover status is unstable, the GVC signal becomes 1 in order to activate the G-vectoring control. Then, F_{xd_accel} should be applied to the lower level control algorithm.

3.2.5 Stability analysis of the proposed control system

In previous section, control inputs have been defined to track the target yaw rate for the yaw moment control (DYC or ESC) and the desired longitudinal velocity for velocity control or net force for preventing rollover using the G-vectoring control (GVC). Nonlinear system can be expressed as follows :

$$\dot{x} = f(x) + d + u \text{ , where } x = \begin{bmatrix} v_y & \gamma & v_x \end{bmatrix}^T = \begin{bmatrix} x_1 & x_2 & x_3 \end{bmatrix}^T \tag{3.34}$$

$$\frac{d}{dt}\begin{bmatrix} x_1 \\ x_2 \\ x_3 \end{bmatrix} = \underbrace{\begin{bmatrix} -2\left(\dfrac{C_f + C_m + C_r}{m}\right)\cdot\dfrac{x_1}{x_3} - \left(x_3^{\,2} + 2\dfrac{C_f l_f + C_m l_m - C_r l_r}{m}\right)\cdot\dfrac{x_2}{x_3} \\ -2\left(\dfrac{C_f l_f + C_m l_m - C_r l_r}{I_z}\right)\cdot\dfrac{x_1}{x_3} - 2\left(\dfrac{C_f l_f^{\,2} + C_m l_m^{\,2} + C_r l_r^{\,2}}{I_z}\right)\cdot\dfrac{x_2}{x_3} \\ x_1 x_2 \end{bmatrix}}_{f(x)}$$

$$+ \underbrace{\begin{bmatrix} \dfrac{2}{m}\left(C_f\delta_f + C_m\delta_m + C_r\delta_r\right) \\ \dfrac{2}{I_z}\left(C_f L_f\delta_f + C_m L_m\delta_m + C_r L_r\delta_r\right) \\ 0 \end{bmatrix}}_{d} + \underbrace{\begin{bmatrix} 0 \\ \dfrac{M_z}{I_z} \\ \dfrac{F_x}{m} \end{bmatrix}}_{u}$$

where, M_z is the direct yaw moment control input and F_x represents the desired longitudinal net force for the G-vectoring and velocity control. Lateral tire forces which are generated by steering angle can be defined as disturbance of the control system.

The proposed control system contains the direct yaw moment and velocity control which includes the G-vectoring control. Therefore, the desired yaw moment and longitudinal net force are determined to satisfy the driver's intention. Stability analysis of the proposed control system should be conducted. For performance verification of the proposed controller, stability analysis based for the closed-loop error dynamics including the control law is provided. The closed-loop error dynamics can be written as

$$\begin{cases} e_1 = v_x - v_{xd} \\ e_2 = \gamma - \gamma_d \end{cases} \tag{3.35}$$

Using the definitions of error dynamics, state equations can be written as follows:

$$\begin{aligned} \dot{e}_1 &= \dot{v}_x - \dot{v}_{xd} = v_y \cdot \gamma + \frac{1}{m} F_{xd} - \dot{v}_{xd} \\ \dot{e}_2 &= \dot{\gamma} - \dot{\gamma}_d = \frac{-2\left(C_f l_f + C_m l_m - C_r l_r\right)}{I_z} \cdot \frac{v_y}{v_x} \\ &\quad - \frac{2\left(C_f l_f^2 + C_m l_m^2 + C_r l_r^2\right)}{I_z} \cdot \frac{\gamma}{v_x} + \frac{2C_f l_f}{I_z}\delta_f + \frac{2C_m l_m}{I_z}\delta_m + \frac{M_{zd}}{I_z} - \dot{\gamma}_d \end{aligned} \tag{3.36}$$

The desired longitudinal net force $\left(F_{xd}\right)$ and yaw moment $\left(M_{zd}\right)$ have been previously defined in equation (3.32) and (3.23). Taking these control law equations, error dynamics can be rewritten as

$$\dot{e}_1 = v_y \cdot \gamma + \frac{1}{m}\hat{m}\left(-v_y \cdot \gamma + \dot{v}_{xd} - K_3 \cdot e_1\right) - \dot{v}_{xd} \tag{3.37}$$

$$= -\frac{\hat{m}}{m} \cdot K_3 \cdot e_1 + \left(1 - \frac{\hat{m}}{m}\right) \cdot v_y \cdot e_2 + \left(1 - \frac{\hat{m}}{m}\right) \cdot v_y \cdot \gamma_d - \left(1 - \frac{\hat{m}}{m}\right) \cdot \dot{v}_{xd}$$

$$\dot{e}_2 = \left\{\left(-c + \hat{c}\right) \cdot v_y + \left(-d + \hat{d}\right) \cdot e_2 + \left(-d + \hat{d}\right) \cdot \gamma_d\right\} \frac{1}{e_1 + v_{xd}} - \frac{\hat{I}_z}{I_z} \cdot K_2 \cdot e_2$$

$$+ \left(-C_f + \hat{C}_f\right) \frac{2 l_f \delta_f}{I_z} + \left(-C_m + \hat{C}_m\right) \frac{2 l_m \delta_m}{I_z} - \dot{\gamma}_d$$

where, $c = \left(\frac{2C_f l_f + 2C_m l_m - 2C_r l_r}{I_z}\right)$, $d = \left(\frac{2C_f {l_f}^2 + 2C_m {l_m}^2 + 2C_r {l_r}^2}{I_z}\right)$

$$\hat{c} = \frac{2\left(\hat{C}_f l_f + \hat{C}_m l_m - \hat{C}_r l_r\right)}{I_z}, \quad \hat{d} = \frac{2\left(\hat{C}_f l_f^2 + \hat{C}_m l_m^2 + \hat{C}_r l_r^2\right)}{I_z}$$

The points $e' \in \mathbb{R}^2$ are equilibrium points for error dynamic equation. The equilibrium points can be obtained to satisfy below equation (3.38).

$$f\left(e'\right) = 0 \tag{3.38}$$

First of all, the equilibrium point e_1' of the first error state e_1 is expressed by that of the second error state e_2 as follows:

$$e_1' = E \cdot v_y \cdot e_2' + E \cdot v_y \cdot \gamma_d - E \cdot \dot{v}_{xd} \tag{3.39}$$

$$where,\ E = \frac{m}{\hat{m} \cdot K_3}\left(1 - \frac{\hat{m}}{m}\right)$$

The second equilibrium point e_2' of the second error state can be written as follows:

$$e_2' = \frac{(c - \hat{c})v_y + \left(d - \hat{d}\right)\gamma_d - Fe_1' - Fv_{xd}}{\left(-d + \hat{d}\right) - \frac{\hat{I}_z}{I_z} \cdot K_2 \cdot e_1' - v_{xd} \cdot \frac{\hat{I}_z}{I_z} \cdot K_2} \tag{3.40}$$

$$where,\ F = \left(-C_f + \hat{C}_f\right)\frac{2l_f\delta_f}{I_z} + \left(-C_m + \hat{C}_m\right)\frac{2l_m\delta_m}{I_z} - \dot{\gamma}_d$$

Substituting equation (3.39), the equation (3.30) is rewritten as

$$-\frac{\hat{I}_z}{I_z}K_2 E v_y (e_2')^2 + \left\{\left(-d + \hat{d}\right) - \frac{\hat{I}_z}{I_z}K_2\left(Ev_y\gamma_d - E\dot{v}_{xd} + v_{xd}\right) + FEv_y\right\}e_2'$$

$$-(c - \hat{c})v_y - \left(-d + \hat{d}\right)\gamma_d + FEv_y\gamma_d + FE\dot{v}_{xd} + Fv_{xd} = 0 \tag{3.41}$$

Using above equation (3.41), the equilibrium point e_2' can be determined by quadratic formula.

$$e_2' = \frac{-\bar{B} \pm \sqrt{\bar{B}^2 - 4\bar{A}\bar{C}}}{2\bar{A}} \tag{3.42}$$

where, $\bar{A} = -\frac{\hat{I}_z}{I_z} K_2 E v_y$

$$\bar{B} = \left(-d + \hat{d}\right) - \frac{\hat{I}_z}{I_z} K_2 \left(E v_y \gamma_d - E\dot{v}_{xd} + v_{xd}\right) + FEv_y$$

$$\bar{C} = -\left(c - \hat{c}\right) v_y - \left(-d + \hat{d}\right)\gamma_d + FEv_y\gamma_d + FE\dot{v}_{xd} + Fv_{xd}$$

After calculating the equilibrium point of error e_2', the equilibrium point of error e_1' can be determined using the equation (3.39).

The obtained error dynamics is nonlinear system. Therefore, the indirect method of Lyapunov is adopted to prove the local stability of the proposed control system. The linearized control system can be obtained by Jacobian matrix as follows:

$$A_{control\_system} = \left.\begin{bmatrix} \frac{\partial f_1}{\partial e_1} & \frac{\partial f_1}{\partial e_2} \\ \frac{\partial f_2}{\partial e_1} & \frac{\partial f_2}{\partial e_2} \end{bmatrix}\right|_{e=e'}, \text{ where } f_1 = \dot{e}_1, f_2 = \dot{e}_2 \tag{3.43}$$

$$= \left.\begin{bmatrix} -\frac{\hat{m}}{m} \cdot K_3 & \varepsilon_m \cdot v_y \\ \frac{-\left(\varepsilon_d \cdot e_2 + \varepsilon_d \cdot \gamma_d + \varepsilon_c \cdot v_y\right)}{\left(e_1 + v_{xd}\right)^2} & \frac{\varepsilon_d}{\left(e_1 + v_{xd}\right)} - \frac{\hat{I}_z}{I_z} \cdot K_2 \end{bmatrix}\right|_{e=e'}$$

where, $\varepsilon_c = \left(-c + \hat{c}\right)$, $\varepsilon_d = \left(-d + \hat{d}\right)$, $\varepsilon_m = \left(1 - \frac{\hat{m}}{m}\right)$, e' denotes equilibrium point.

Assuming that cornering stiffness, moment of inertia and mass of the vehicle are constant values, ε_c , ε_d and ε_m can be determined. Used nominal parameters were defined in table 3.2. Eigenvalues of Jacobian matrix $A_{control\_system}$ can be obtained and are in the open left half complex plane. Therefore, the behavior of the system in the neighborhood of each equilibrium points (e_1' , e_2') can be verified as stable.

3.3 Lower Level Control Layer

A proposed lower level control layer is based on a control allocation method and suitable for an independent driving vehicle equipped with 6 in-wheel motors. The lower level control layer is designed to distribute the longitudinal wheel torque inputs at each wheel in order to satisfy the desired longitudinal net force and yaw moment calculated by the upper level control layer. Distributed wheel torque inputs are determined proportionally to the friction circle according to changing driving conditions under estimation of the size of the friction circle. Excessive wheel slip makes the vehicle unstable and dangerous. Therefore, wheel torque distribution methods need to take into account wheel slip conditions. For protection of power electric elements, power and actuator limitations are considered. Amount of the generable and regenerative power should be limited to distribute wheel torque.

3.3.1 Control Allocation Formulation

The role of the control allocation is to obtain actual controls which give rise to the desired virtual controls. In general, the relationship is $v(t) = g(u(t))$ where $v(t) \in \Re^k$ are the virtual controls, $u(t) \in \Re^m$ denotes the actual controls and $g : \Re^m \to \Re^k$ is the mapping from actual to virtual controls, where $m > k$ (over actuated system). The majority of the literature deals with the linear case [Härkegård02], where the actual and virtual controls are related

by a control effectiveness matrix B.

$$v(t) = Bu(t) \tag{3.44}$$

The control allocation problem is an under-determined, and often constrained problem. A common approach is to formulate an optimization problem in which the magnitude of the allocation error:

$$\varepsilon = \left\| Bu(t) - v(t) \right\|_p, \; p = 1, 2, ... \tag{3.45}$$

is minimized, subject to constraints and possibly additional costs on actuator purpose. An important requirement imposed on the control allocation algorithm is that it must be implementable in a real-time environment. This is particularly important in automotive contexts, where sample times are typically of the order of 5~10ms. Algorithms with high levels of computational complexity are therefore not well suited to the application.

In order to use optimization for control allocation, it is necessary to construct convex optimization problems. The general form of a convex optimization problem is :

$$\begin{aligned} &\text{minimize} \;\; f_0(x) \\ &\text{subject to} \;\; f_i(x) \le b_i, \; i = 1, 2, ..., m \end{aligned} \tag{3.46}$$

in which the cost function $f_0(x)$ and the constraints $f_i(x) \le b_i$ are convex functions. The feasible set P of the optimization problem is the region in which the constraints are satisfied. The optimum x^* is the point in the feasible set where the cost function is minimized as shown in figure 3.14.

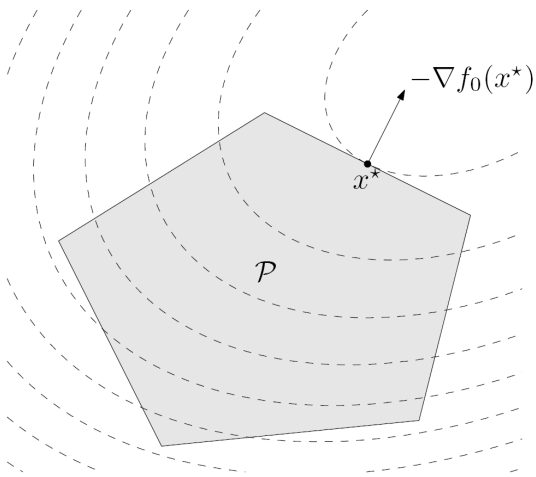

Figure 3.14 Interpretation of the solution of a QP problem

Cost Function and Constraints Definition for Control Allocation Problem Formulation

In this paper, control allocation method is useful for independent driving systems equipped with more than six in-wheel motors and used to design the lower level control layers of 6WD/6WS vehicles for optimal distribution. The control inputs are the driving torques (T_i, i=1,…,6) of the in-wheel motors and can generate the desired net longitudinal force and yaw moment which is

determined by the upper level control layer. The maximum generable and regenerative power should be considered to protect electric power circuits for allocation of wheel torques. The desired dynamics and control inputs are related as follows :

$$\begin{bmatrix} F_x \\ M_z \\ P \end{bmatrix} = \begin{bmatrix} \frac{\cos\delta_f}{r_w} & \frac{\cos\delta_f}{r_w} & \frac{\cos\delta_m}{r_w} & \frac{\cos\delta_m}{r_w} & \frac{1}{r_w} & \frac{1}{r_w} \\ \frac{\left(L_f \sin\delta_f - t_w \cos\delta_f\right)}{r_w} & \frac{\left(L_f \sin\delta_f + t_w \cos\delta_f\right)}{r_w} & \frac{-t_w \cos\delta_m}{r_w} & \frac{t_w \cos\delta_m}{r_w} & \frac{-t_w}{r_w} & \frac{t_w}{r_w} \\ k_1 r_{w1}\omega_1 & k_2 r_{w2}\omega_2 & k_3\omega_3 & k_4\omega_4 & k_5\omega_5 & k_6\omega_6 \end{bmatrix} \cdot \begin{bmatrix} T_1 & T_2 & T_3 & T_4 & T_5 & T_6 \end{bmatrix}^T = B \cdot u \tag{3.47}$$

The control input (u) of control allocation is determined to minimize the performance index as follows :

$$u(t) = \arg\min\left[\varepsilon \left\| W_u \cdot u \right\|^2 + \left\| W_v \left(Bu - v_d \right) \right\|^2 \right] \tag{3.48}$$

subject to $u_{\min} < u < u_{\max}$

$where,\ u = \begin{bmatrix} T_1 & T_2 & T_3 & T_4 & T_5 & T_6 \end{bmatrix}^T$

$v_d = \begin{bmatrix} F_{xd} & M_{zd} & P_{capable} \end{bmatrix}^T$

$$P_{capable} \begin{cases} \left(P_{E/G}\right)_{capable} + \left(P_B\right)_{capable} & \text{if traction control} \\ \left(P_B\right)_{regen} & \text{if braking control} \end{cases}$$

$$B = \frac{1}{r_w}\begin{bmatrix} \cos\delta_f & \cos\delta_f & \cos\delta_m & \cos\delta_m & 1 & 1 \\ \left(L_f \sin\delta_f - t_w \cos\delta_f\right) & \left(L_f \sin\delta_f + t_w \cos\delta_f\right) & -t_w \cos\delta_m & t_w \cos\delta_m & -t_w & t_w \\ k_1 r_{w1}\omega_1 & k_2 r_{w2}\omega_2 & k_3 r_{w3}\omega_3 & k_4 r_{w4}\omega_4 & k_5 r_{w5}\omega_5 & k_6 r_{w6}\omega_6 \end{bmatrix}$$

where ε is a small value used to balance between allocation error and actuation cost. $u_{\min}$ and $u_{\max}$ denote the lower and upper bounds of actuation magnitude limits, respectively. These limits depend on not only wheel speed conditions but also wheel slip condition of in-wheel motors. Wheel conditions related to angular velocity, tire normal force, and the friction coefficient between the tire and road. v_d denotes the desired dynamic matrix, and the B matrix represents relation between the desired dynamics and control inputs. Efficiency of in-wheel motors is defined according to driving and regenerative conditions respectively as follows :

$$k_i = \begin{cases} k_i = \dfrac{1}{\eta_i} & \text{if driving conditions} \\ k_i = \eta_i & \text{if regenerative condition} \end{cases} \tag{3.49}$$

Weighting factors need to be defined to take into account friction circle information and balance between desired longitudinal net force and yaw moment as follows:

$$W_u = diag\left[\frac{1}{(\mu_1 F_{z1})_n} \quad \frac{1}{(\mu_2 F_{z2})_n} \quad \frac{1}{(\mu_3 F_{z3})_n} \quad \frac{1}{(\mu_4 F_{z4})_n} \quad \frac{1}{(\mu_5 F_{z5})_n} \quad \frac{1}{(\mu_6 F_{z6})_n}\right]$$

$$where,\ \left(\mu_i F_{zi}\right)_n = \frac{\left(\mu_i F_{zi}\right)_{est}}{\left(\mu_i F_{zi}\right)_{ss}} \tag{3.50}$$

To improve performance of turning and uphill driving, control inputs are proportional to the size of the friction circle. In the case of turning driving conditions, the friction circle of outer wheel is greater than that of inner wheel due to mass transfer. And, the friction circle of front wheel is less than that of rear wheel due to gravity in climbing conditions. Therefore, weighting factor related to friction circle information is defined as steady state friction circle $\left(\mu_i F_{zi}\right)_{ss}$ and estimated friction circle $\left(\mu_i F_{zi}\right)_{est}$.

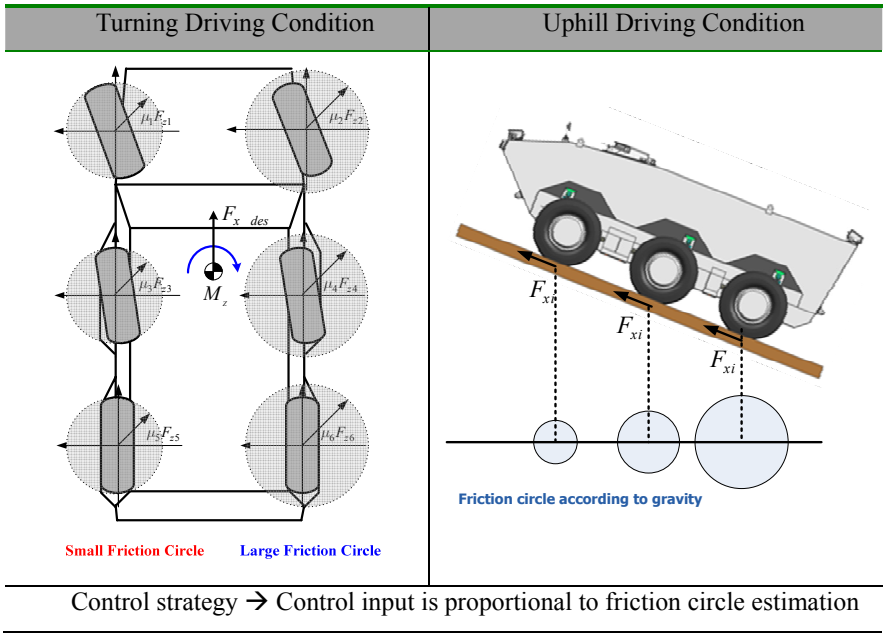

Figure 3.15 Definition of weighting factor related to friction circle information

The friction circle information will be estimated in chapter 4. Normalization of the friction circle for the i-th wheel $\left(\mu_i F_{zi}\right)_n$ is defined as steady state and estimated friction circle information. Steady state friction circle information cannot be statically indeterminate and the normal forces under the tires cannot be determined by static equilibrium equations. It is necessary to consider the suspensions' deflection to determine their applied forces.

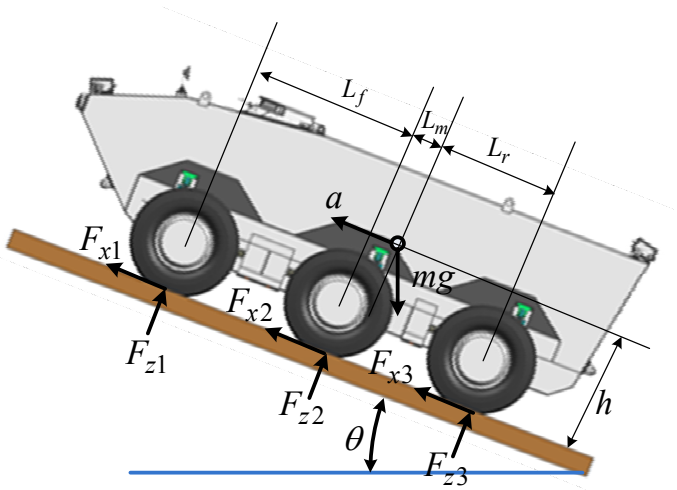

Figure 3.16 Calculation of steady state friction circle information

The n normal forces F_{zi}, under the tires can be calculated using the following n algebraic equations.

$$2F_{x1} + 2F_{x1} + 2F_{x1} - mg\sin\theta = ma \tag{3.51}$$

$$2F_{z1} + 2F_{z2} + 2F_{x3} - mg\cos\theta = 0 \tag{3.52}$$

$$2F_{z1}x_1 + 2F_{z2}x_2 + 2F_{x3}x_3 + 2h\left(F_{x1} + F_{x2} + F_{x3}\right) = 0 \tag{3.53}$$

$$\frac{1}{x_2 - x_1}\left(\frac{F_{z2}}{k_2} - \frac{F_{z1}}{k_1}\right) - \frac{1}{x_3 - x_1}\left(\frac{F_{z3}}{k_3} - \frac{F_{z1}}{k_1}\right) = 0 \tag{3.54}$$

To obtain steady state friction circle information, the set of equations for wheel loads is linear and may be arranged in a matrix form as follows :

$$[A]\cdot[X] = [B] \tag{3.55}$$

where, $[A] = \begin{bmatrix} 2 & 2 & 2 \\ 2x_1 & 2x_2 & 2x_3 \\ k_2k_3(x_2 - x_1) & k_1k_3(x_3 - x_1) & k_1k_2(x_1 - x_2) \end{bmatrix}$

$[X] = [F_{z1} \quad F_{z2} \quad F_{z3}]^T$

$[B] = \begin{bmatrix} mg\cos\theta \\ -hm(a + g\sin\theta) \\ 0 \end{bmatrix}^T$

$x_1 = L_f$, $x_2 = L_m$, $x_3 = -L_r$, k_i : suspension stiffness

Weighting matrix (W_v) consists of weighting factors (w_{Fx}, w_{Mz}) related to desired net force and yaw moment and power limitation weighting factor(w_P) which has been included to consider limit of amount of the required power for protection from electric damages through over voltage or current.

$$W_v = \begin{bmatrix} w_{Fx} & 0 & 0 \\ 0 & w_{Mz} & 0 \\ 0 & 0 & w_P \end{bmatrix} \tag{3.56}$$

where, w_{Fx} : net force weighting, w_{Mz} : yaw moment weighting,
w_P: related to generable and required power

Weighting factor (w_P) related to power control is determined by regenerative brake power or difference between generable and required power. When regenerative power is greater than -50 kW, weighting factor w_P increases significantly in severe braking condition. Then, power limitation has an effect on torque distribution dominantly. When differences between required and generable power is greater than zero, weighting factor w_P increases as shown in figure 3.17.

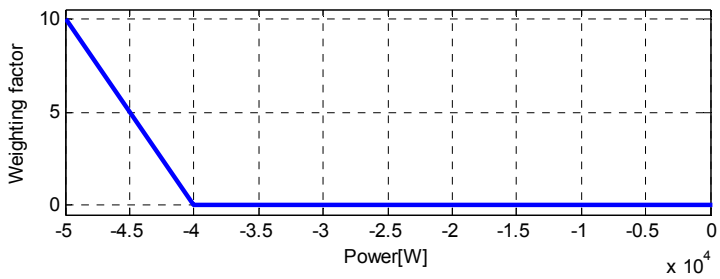

(a) Weighting factor (w_P) on braking driving conditions

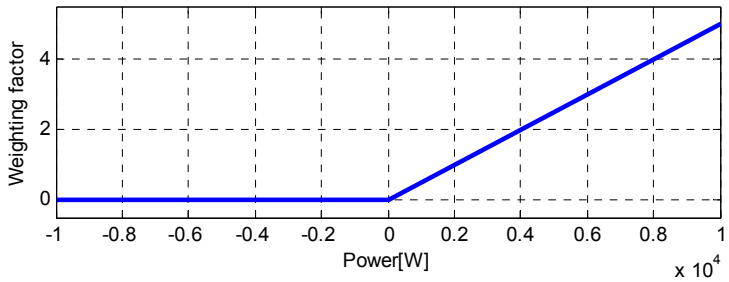

(b) Weighting factor (w_P) according to difference between the required and generable power on traction driving conditions $(P_{req} - P_{generable})$

Figure 3.17 Weighting factors (w_P) definition according to driving conditions

Braking simulation has been conducted to verify performance of power limitation. Initial velocity is 60 km/h and braking deceleration is 3m/s^2. In the beginning of braking situation, the regenerated power becomes greater than the maximum regenerated power. Therefore, the regenerated power should be limited to protect electric devices. Figure 3.18 (a) and (b) show the longitudinal vehicle velocity and deceleration during power limit simulations. Figure 3.18 (c) and (d) show that regenerated power is limited and is not greater than 50kW. Though in-wheel motors can afford to generate power greater than 60kW, the integrated driving control algorithm limits regenerated power to bounded values for protection of electric devices. Due to power limitation, braking deceleration is slightly reduced. Because output torques have been limited, generated net force is also bounded as shown in figure 3.18 (e). Figure 3.18 (g) shows how weighting factor w_p changes according to regenerated power.

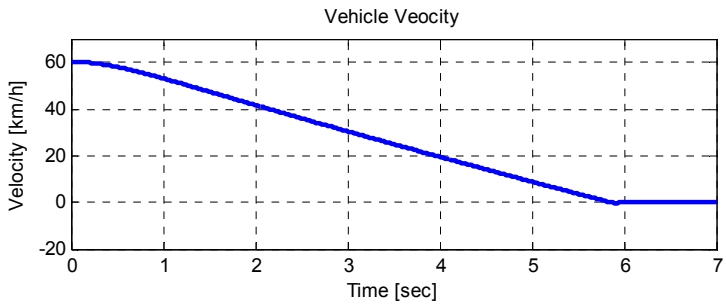

(a) Vehicle velocity [km/h]

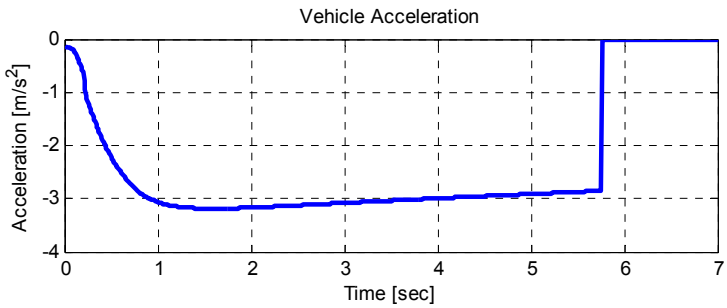

(b) Acceleration [m/s^2]

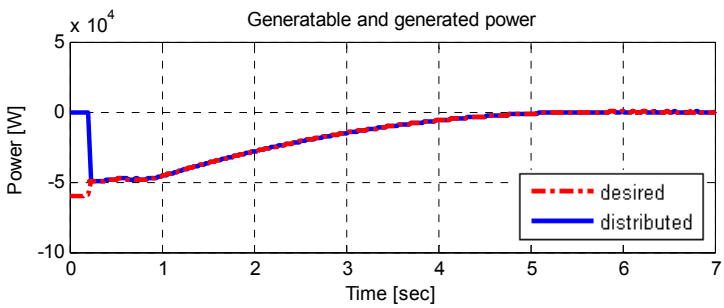

(c) Regenerated power [W]

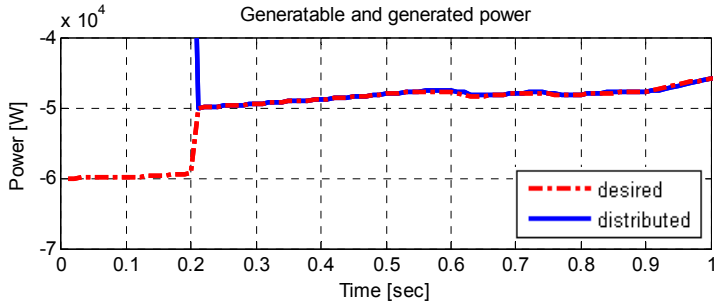

(d) Regenerated power (0~1 seconds) [W]

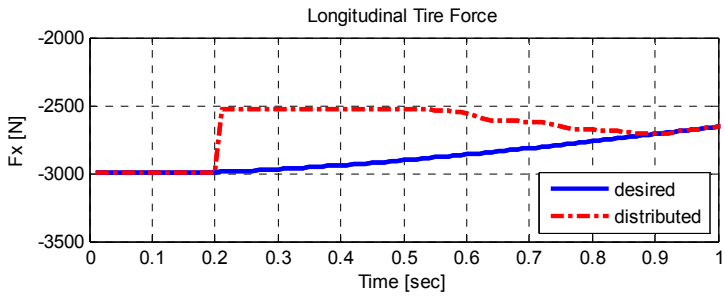

(e) Limited longitudinal net force [N]

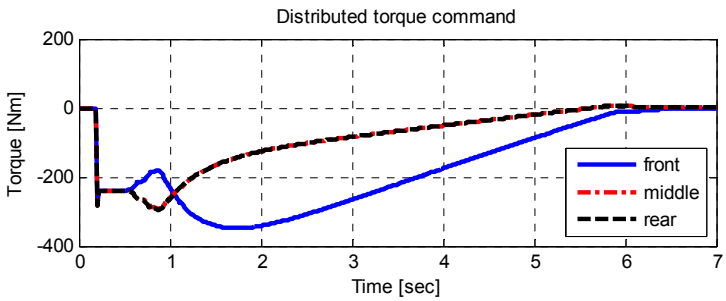

(f) Distributed torque [Nm]

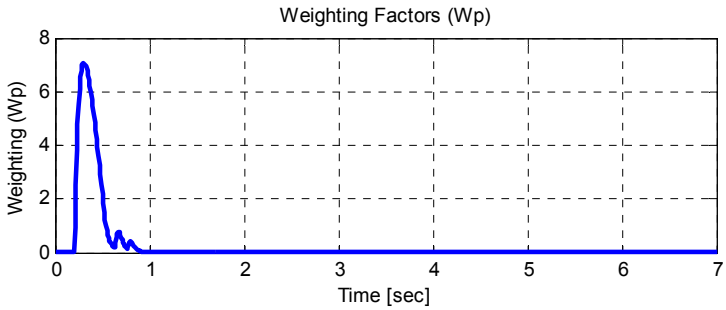

(g) Weighting factor (W_p)

Figure 3.18 Simulation results for consideration of power limit

Actuator Limitation Algorithm

Actuator limitation includes magnitude and rate limitation according to driving conditions.

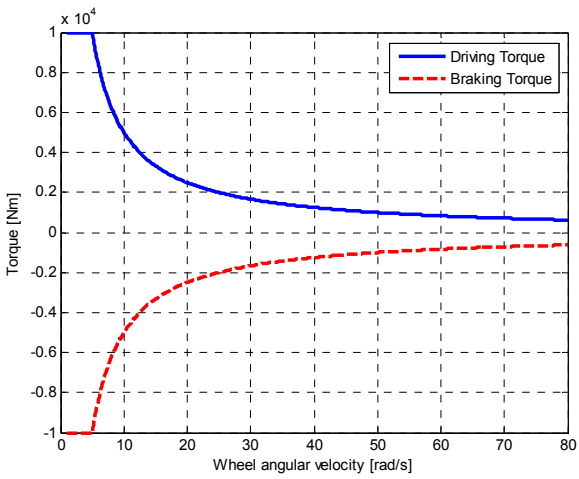

Figure 3.19 Performance curve of the in-wheel motors

The maximum and minimum output torque is bounded by wheel angular velocity according to performance curve of in-wheel motors as shown in figure 3.19.

Rate constraints in the actuators may be taken into account in the control allocation problem by modifying the constraints at each sampling time.

$$r_{\min} \le \dot{u}(t) \le r_{\max} \tag{3.57}$$

Approximating the derivative with the backward difference method :

$$\dot{u}(t) \approx \frac{u(t) - u\left(t - T_{sampling}\right)}{T_{sampling}} \tag{3.58}$$

where $T_{sampling}$ is the sampling time period allows the rate constraints to be rewritten as position constraints. The new constraints are given by:

$$u_{\min} = \max\left[u_{\min}, u\left(t - T_{sampling}\right) + T_{sampling} \cdot r_{\min}\right] \tag{3.59}$$

$$u_{\max} = \min\left[u_{\max}, u\left(t - T_{sampling}\right) + T_{sampling} \cdot r_{\max}\right] \tag{3.60}$$

Slip Limitation Algorithm

The wheel slip limitation algorithm is designed to keep the slip ratio of each wheel below the maximum slip ratio so as to guarantee lateral tire force for stable turning motion. Figure 3.20 shows the strategy of the wheel slip control algorithm.

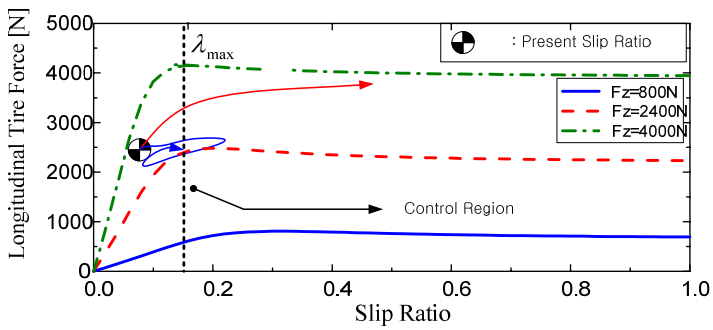

Figure 3.20 Strategy of the wheel slip limitation algorithm

The maximum wheel slip ratio is set to 0.2 in order to guarantee sufficient lateral tire forces for vehicle turning motion. The desired wheel speed is determined using vehicle and wheel velocity information differently depending on the driving conditions:

$$\omega_{id} = \begin{cases} \dfrac{v_i}{r_i(1-\lambda_{\max})} & \text{if } (\lambda > \lambda_{\max}) \text{ Driving} \\ \dfrac{v_i}{r_i}(1-\lambda_{\max}) & \text{if } (\lambda < -\lambda_{\max}) \text{ Braking} \end{cases} . \tag{3.61}$$

If the defined wheel angular velocity for prevention of excessive wheel slip is larger than the measured wheel angular velocity, input constraints related to actuator limitations need to be modified to implement slip control similar to traction control (TCS) and anti-lock brake systems (ABS). In traction conditions, input constraint is defined as follows :

$$u_{\max} = \min\left[u_{\max}, u\left(t - T_{sampling}\right) + T_{sampling} \cdot r_{\max}, u_{\max\_\text{slip}}\right] \quad (3.62)$$

$$where, \begin{cases} u_{\max\_\text{slip}} = u_{\max} & if \ \omega_{id} \le \omega_i \\ u_{\max\_\text{slip}} = 0 & if \ \omega_{id} > \omega_i \end{cases}$$

Under braking conditions, minimum input torque needs to be set to zero in order to prevent excessive wheel slip as follows :

$$u_{\min} = \max\left[u_{\min}, u\left(t - T_{sampling}\right) + T_{sampling} \cdot r_{\min}, u_{\min\_\text{slip}}\right] \quad (3.63)$$

$$where, \begin{cases} u_{\min\_\text{slip}} = u_{\min} & if \ \omega_{id} \le \omega_i \\ u_{\min\_\text{slip}} = 0 & if \ \omega_{id} > \omega_i \end{cases}$$

Lane change simulation has been conducted to verify performance of slip limitation algorithm. Initial velocity is 60 km/h and friction coefficient is 0.6. Due to drastically severe steering input, drive and brake torque are applied to guarantee yaw stability of the vehicle. In the case of low friction coefficient, excessive wheel slip can be easily generated by large drive and brake torque. Figure 3.21 (d) and (e) show remarkable slip limitation algorithm

performance. In the case of no slip limitation control, wheel slip conditions become high. However, slip limitation algorithm regulates excessive wheel slip condition.

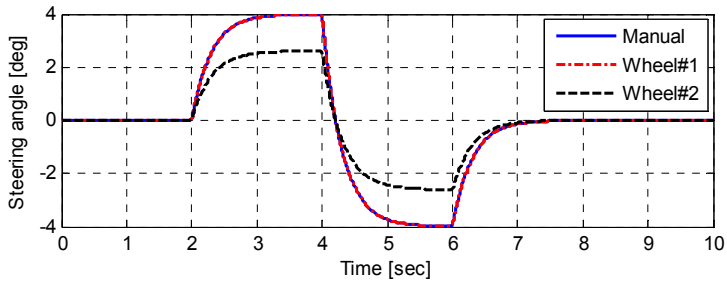

(a) Steering angle [deg]

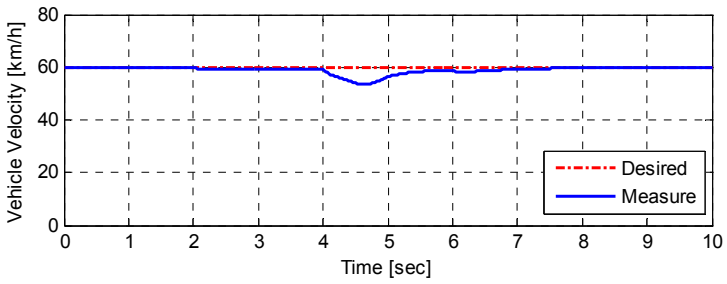

(b) Vehicle velocity [km/h]

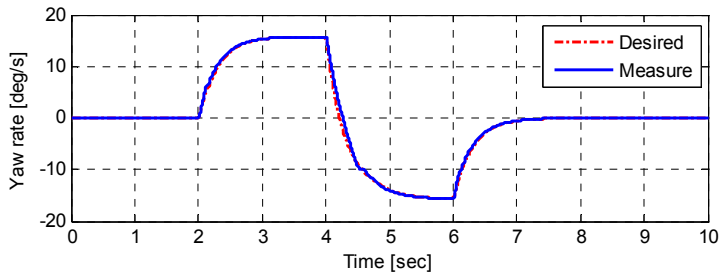

(c) Yaw rate [deg/s]

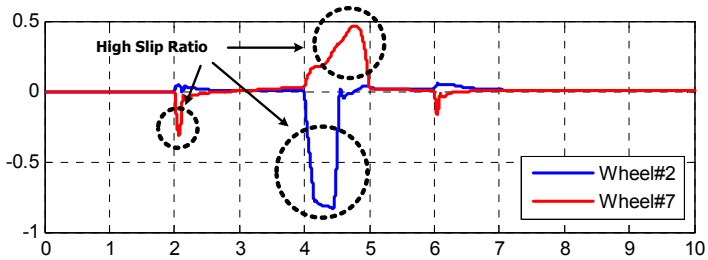

(d) Wheel slip ratio in the case of no slip limitation control

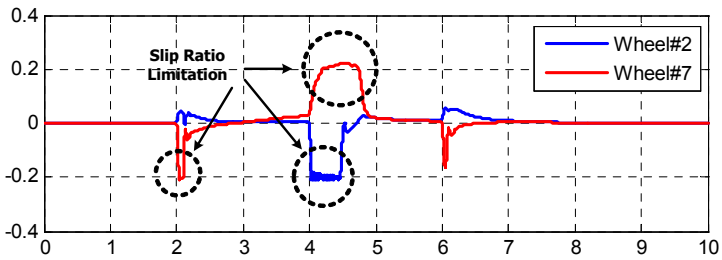

(e) Wheel slip ratio in the case of slip limitation control

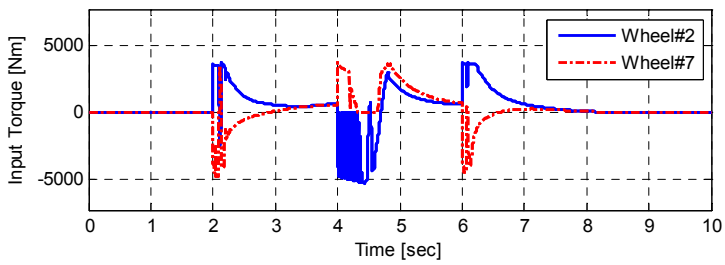

(f) Distributed torque [Nm]

Figure 3.21 Simulation results of slip limitation algorithm

3.3.2 Fixed-point (FXP) control allocation method

For solving control allocation problems, we need to select the proper algorithm. The fixed-point algorithm is the most simple among other solver methods. Many of computations need to be performed only once before iterations starts. Remarkably, the algorithm also provides an exact solution to the optimization problem, and it is guaranteed to converge. Its drawback is that convergence of the algorithm can be very slow and strongly dependent on the problem. The number of iterations required can vary by orders of magnitude depending on the desired vector. In addition, the choice of the parameter ε is delicate, as affects the objectives, as well as the convergence of the algorithm. A fixed-point control allocation (CA) method originally proposed by Burken was used to solve the control allocation problem with respect to nonlinear system control for aircraft [Burken99]. Wang later applied this method to optimal distribution for ground vehicles [Wang06]. The fixed-point method finds the control input vector $u(t)$ that minimizes :

$$u(t) = \arg\min\left[\varepsilon\left\|W_u \cdot u\right\|^2 + (1-\varepsilon)\left\|W_v\left(Bu - v_d\right)\right\|^2\right] \tag{3.64}$$

subject to $u_{\min} < u < u_{\max}$

The fixed-point control allocation algorithm iterates according to the following equation:

$$u_{k+1} = sat\left[\left(1-\varepsilon\right)\eta B_{k-1}{}^{T} W_v v_d - \left(\eta T - I\right)u_k\right] \tag{3.65}$$

where,

$$T = \left(1-\varepsilon\right)\eta B_{k-1}{}^{T} W_v B_{k-1} + \varepsilon W_u, \quad \left\|T\right\|_F = \left(\sum_{i=1}^{p}\sum_{j=1}^{p} t_{ij}{}^{2}\right)^{\frac{1}{2}}, \quad \eta = 1/\left\|T\right\|_F$$

T is a symmetric matrix, $\eta = 1/\left\|T\right\|_F$, t_{ij} are the elements of matrix T, with $\left\|T\right\|_F$ being the Frobenius norm of matrix T. The saturation function, sat, clips the elements of the control vector according to:

$$sat\left(u\right) = \begin{cases} \overline{u}_i, & u_i \geq \overline{u}_i \\ u_i, & \underline{u}_i \leq u_i \leq \overline{u}_i, \quad i = 1, 2, ..., p \\ \underline{u}_i, & u_i \leq \overline{u}_i \end{cases} \tag{3.66}$$

The convergence can through be very slow. Therefore it is essential to find a proper value ε. There is a trade-off; a large value speeds up the convergence but makes it hard for the algorithm to find the exact solution. A small value for ε leads to slightly slower convergence but the algorithm converges closer to its optimal solution. Compared with other QP-based control allocation methods such as active-set and primal-dual interior-point, one of the advantages of the fixed-point method is its extremely low computational effort, which is very attractive for real-time control systems.

3.3.3 Cascaded Generalized pseudo-inverse (CGI) method

Most existing methods for control allocation can be classified as pseudo-inverse methods. In general, control inputs for quadratic program solutions are obtained using these equations as follows:

$$\begin{aligned} u &= \arg\min_{u=\Omega} \left\| W_u \left(u - u_d \right) \right\|_p \\ \Omega &= \arg \min_{u_{\min} \le u \le u_{\max}} \left\| W_v \left(Bu - v \right) \right\|_p \end{aligned} \tag{3.67}$$

If the actuators constraints are disregarded, equation (3.67) can be simplified and rewritten as shown in equation (3.68).

$$\min_u \left\| W_u \left(u - u_d \right) \right\|_2 , \text{ subject to } Bu = v \tag{3.68}$$

which has an explicit solution given by

$$u = \left(I - GB \right) u_d + Gv \tag{3.69}$$

where $G = W_u^{-1} \left(BW_u^{-1} \right)^{\dagger} = W_u^{-1} \left(BW_u^{-1} \right)^T \left\{ \left(BW_u^{-1} \right) \left(BW_u^{-1} \right)^T \right\}^{-1}$

Here "$\dagger$" is the pseudo-inverse operator. The allocation efficiency depends on the choice of the pseudo-inverse matrix G. Durham [Durham93] considered the case u_d=0, and posed the question as to whether there was any

G that solved the control allocation problem for the entire attainable moment subset (AMS). In order to improve the allocation efficiency of the algorithm, Virning and Bodden [John04] proposed a redistributed pseudo-inverse (RPI) scheme, in which all control inputs that violated their limits in the pseudo inverse solution equation (3.69) were saturated and removed from the optimization. Then the control allocation problem was resolved with only the remaining control inputs as free variables. Specific steps are as follows:

Cascaded Generalized pseudo-inverse method

Step 1. Use pseudo-inverse method to distribute the desired moments v and get the distribution result $u = Gv$.

Step 2. According to whether the control variables exceed the actuator limits, divide the control variables into two groups. The first group u_1 is beyond constraints Ω. The second group u_2 does not exceed the limits for the control variables. Correspondingly, control efficiency matrix B is also divided into two parts: B_1 and B_2.

Step 3. Set the control variables of u_1 at the corresponding minimum or maximum value. So the maximum virtual control that u_1 can afford is $v_1 = B_1 u_1$. Then remaining undistributed virtual control $v_2 = v - v_1$.

Step 4. Solve the problem $v_2 = B_2 u_2$ through the generalized inverse method. Then the solution of $Bu = v$ is $u = \begin{bmatrix} u_1 & u_2 \end{bmatrix}^T$.

Figure 3.22 Pseudo-code for cascaded generalized inverse method

3.3.4 Interior point (IP) method

In general, there is no guarantee that v is attainable or that the solution is unique. If the solution is not unique, a secondary objective is to minimize the magnitude of the control vector, or its distance from the reference control value, u_d. Combining two objectives is known as mixed optimization, and can be expressed as the quadratic programming problem

$$\min_u J = \left\| (Bu - v_d) \right\|_2^2 + h \left\| (u - u_d) \right\|_2^2 \tag{3.70}$$

subject to $u_{\min} \le u \le u_{\max}$

where $h > 0$. The factor h is used to adjust the relative weighting of the secondary criteria and is usually chosen to be small. Equation (3.70) can be converted to a standard quadratic problem formulation. Let

$$\begin{cases} x = u - u_{\min} \\ x_d = u_d - u_{\min} \\ x_{\max} = u_{\max} - u_{\min} \\ v_0 = v_d - Bu_{\min} \end{cases} \tag{3.71}$$

The resulting constraint set is

$$x + w = x_{\max},\ where\ x \geq 0,\ w \geq 0 \tag{3.72}$$

where w is a slack variable used to guarantee the upper bound on x. J can be expanded to

$$\begin{aligned} J &= \left(Bx - v_0\right)^T \left(Bx - v_0\right) + h\left(x - x_d\right)^T \left(x - x_d\right) \\ &= \frac{1}{2} x^T Hx + c^T x + k \end{aligned} \tag{3.73}$$

where $H = 2\left(B^T B + hI\right),\ c^T = -2\left(v_0 B + hx_0^T\right)$, and $k = v_0^T v_0 + hx_0^T x_0$.

Since a constant in the cost function does not affect the optimal solution, k is dropped and the final form is

$$\begin{aligned} &\min_u J = \frac{1}{2} x^T Hx + c^T x \\ &\text{subject to } x + w = x_{\max},\ where\ x \geq 0,\ w \geq 0 \end{aligned} \tag{3.74}$$

If the weighting factor, h, is greater than zero, or if B has full row rank, H will be positive definite. Under this condition, the cost function equation (3.74) is convex and the Karush-Kuhn-Tucker (KKT) optimality conditions apply globally. Making use of logarithmic barrier functions to satisfy the lower bound constraints, the Lagrangian of equation (3.75) is expressed as

follows:

$$L = \frac{1}{2}x^T Hx + c^T x + z^T \left(x + w - x_{\max}\right) - \mu \sum_{i=1}^{n} \log\left(x_i\right) - \mu \sum_{i=1}^{n} \log\left(w_i\right) \tag{3.75}$$

where $\mu > 0$. From the Lagrangian, the first-order optimality conditions are derived as follows:

$$\begin{aligned} &Hx + c + z - s = 0 \\ &x + w - x_{\max} = 0 \\ &Xs - \mu e = 0 \\ &Wz - \mu e = 0 \\ &\text{where } x > 0,\ w > 0,\ z > 0,\ s > 0 \end{aligned} \tag{3.76}$$

where X and W are diagonal matrices whose diagonal elements are x and w, respectively. e is defined as a column vector of ones. s and z are vectors used for convenience and are defined as $s_i = \mu / x_i$ and $z_i = \mu / w_i$. To satisfy the KKT conditions, equation (3.76) must hold with $\mu = 0$. In this case, $Xs = 0$ and $Wz = 0$, which are known as the complementary conditions. The parameter μ is referred to as the complementary gap and is used to guide the solution along a trajectory called the central path. The central path is a sequence of solutions that leads to the optimal point. Path-following methods attempt to travel in the neighborhood of the central path until a solution is near optimum.

Primal-dual interior point method

Given v_d, $u_{\min}$, $u_{\max}$ and B

Convert the control allocation problem to a quadratic program

Choose values for parameters ρ and the stopping tolerance ε_s

Compute starting point, (x, s, w, z), e.g. $x = w = 0.5x_{\max}$, $s = z > 0$

Compute complementary gap,

$$\mu = \min(0.1, 100\gamma), \ where \ \gamma = \frac{x^T s + w^T z}{2n}$$

Compute feasibility residuals $(r_c,\ r_{xs},\ r_{wz}$ and $r_u)$

While $\mu > \varepsilon_s$

Solve for the step direction

$$\begin{bmatrix} \Delta x \\ \Delta w \\ \Delta s \\ \Delta z \end{bmatrix} = \begin{bmatrix} D\left(r_c + W^{-1} r_{wz} - X^{-1} r_{xs} - W^{-1} Z r_u\right) \\ -\Delta x - r_u \\ -X^{-1} r_{xs} - X^{-1} S \Delta x \\ -W^{-1} r_{wz} - W^{-1} Z \Delta w \end{bmatrix}$$

where, $D = \left(H + X^{-1} S + W^{-1} Z\right)^{-1}$

Compute the step size

$$\alpha_p = \min\left\{ \left[-\frac{p_i}{\Delta p_i}, 1 \right] \middle| \Delta p_i < 0,\ i = 1, \ldots, n \right\} \text{ for } p \in \{x, w, s, z\}$$

$$\alpha = \min\{\alpha_x, \alpha_w, \alpha_s, \alpha_z\}$$

Update the variables x, w, s, z

$$x = x + \rho \alpha \Delta x$$

$w = w + \rho\alpha\Delta w$

$s = s + \rho\alpha\Delta s$

$z = z + \rho\alpha\Delta z$

Compute complementary gap

Compute feasibility residuals

End while

Compute control vector, $u = x + u_{\min}$

Figure 3.23 Pseudo-code for primal-dual interior point method

The steps to a primal-dual interior point algorithm are shown in figure 3.23 encapsulates the algorithm in pseudo-code.

Step 1. Step direction : $\{s + \Delta s, w + \Delta w, x + \Delta x, z + \Delta z\}$ is used to get the step direction instead of $\{s, w, x, z\}$ and drop the second-order terms to arrive at

$$\begin{aligned}
\Delta x &= D\left(r_c + W^{-1} r_{wz} - X^{-1} r_{xs} - W^{-1} Z r_u\right) \\
\Delta w &= -\Delta x - r_u \\
\Delta s &= -X^{-1} r_{xs} - X^{-1} S \Delta x \\
\Delta z &= -W^{-1} r_{wz} - W^{-1} Z \Delta w
\end{aligned} \tag{3.77}$$

where $D = \left(H + X^{-1} S + W^{-1} Z\right)^{-1}$ and the residuals are defined as follows :

$$\begin{aligned}
r_c &= Hx + c + z - s \\
r_u &= x + w - x_{\max} \\
r_{xs} &= Xs - \mu e \\
r_{wz} &= Wz - \mu e.
\end{aligned} \tag{3.78}$$

Z and S are defined as diagonal matrices with elements of z and s along the diagonal, respectively. These residuals make initialization a simple matter by allowing infeasible starting points, i.e., points that do not satisfy the equality constraints, as opposed to feasible points which can be difficult to determine.

Step 2. Step size : Since the variables are coupled through the equation $r_c = Hx + c + z - s$, a common step size must be used in the updates of all variables. To satisfy the inequality constraints, the maximum allowable step size α must be determined. The update law is expressed as follows :

$$x = x + \rho\alpha\Delta x \tag{3.79}$$

$$w = w + \rho\alpha\Delta w$$

$$s = s + \rho\alpha\Delta s$$

$$z = z + \rho\alpha\Delta z$$

where, $\alpha = \min\{\alpha_x, \alpha_w, \alpha_s, \alpha_z\}$ and $\alpha_p = \min\left\{\left[-\frac{p_i}{\Delta p_i}, 1\right] \middle| \Delta p_i < 0,\ i = 1,\ldots,n\right\}$

for $p \in \{x, w, s, z\}$. The term ρ must be in the range $0 < \rho < 1$, but is usually chosen above 0.9 for fast convergence. ρ is set to 0.9995 for implementation.

Step 3. Computation of μ : As μ goes to zero, the iterates converge to an optimal point. In an attempt to keep the variables in the proximately of the

central path, the elements of Xs and Wz are reduced to zero at a similar rate. This can be accomplished by computing μ using the average of the complementarity conditions as follows:

$$\Upsilon = \frac{x^T s + w^T z}{2n}, \ \mu = \sigma\Upsilon \tag{3.80}$$

where $0 < \sigma < 1$. σ can be chosen dynamically to improve convergence as suggested by Vanderbei [Vanderbei98] and Zhang [Zhang95].

Step 4. Stopping criteria : From KKT criterion, the optimal solution occurs when all the residuals and the complementarity gap is zero. The residuals r_c and r_u can be forced to be zero at initialization. With r_c and r_u both zero, the only errors left in the system are directly related to μ. Therefore, when μ has converged closed to zero, the algorithm is terminated.

Step 5. Starting Point: the presence of H in the matrix D has a stabilizing effect on the conditioning of the system, as well as adding robustness to the starting point. Setting initial values of $x = w = 0.5x_{\max}$ and $s = z > 0$, forces $r_c = r_u = 0$ so that the equation (3.77) may be simplified.

3.3.5 Weighted least square method (active set method)

The control allocation problem is often stated as a constrained least squares problem. In this section, active set method is used to solve the l_2 - optimal

control allocation problem :

$$u = \arg \min_{u_{\min} \le u \le u_{\max}} \left\| W_u \left(u - u_d \right) \right\|^2 + \Upsilon \left\| W_v \left(Bu - v \right) \right\|^2 \tag{3.81}$$

Considering the bounded and equality constrained least square problem, the control allocation solution can be obtained using simplified cost function equation as follows :

$$\begin{aligned} &\min_{\underline{u} \le u \le \overline{u}} \left\| Au - b \right\|^2 \\ &Bu = v \\ &Cu \ge U \end{aligned} \tag{3.82}$$

where, $\left\| W_u \left(u - u_d \right) \right\|^2 + \Upsilon \left\| W_v \left(Bu - v \right) \right\|^2 = \left\| \underbrace{\begin{pmatrix} \Upsilon^{\frac{1}{2}} W_v B \\ W_u \end{pmatrix}}_{A} u - \underbrace{\begin{pmatrix} \Upsilon^{\frac{1}{2}} W_v v \\ W_u u_d \end{pmatrix}}_{b} \right\|^2$

$$C = \begin{bmatrix} I \\ -I \end{bmatrix}, \; U = \begin{bmatrix} \underline{u} \\ -\overline{u} \end{bmatrix}$$

An active set method solves this problem by solving a sequence of equality constrained problems. In each step some of the inequality constraints are regarded as equality constraints, and form the working set *W*, while the remaining inequality constraints are disregarded. The working set at the optimum is known as the active set of the solution. The active set method is similar to the cascaded generalized inverse method. The difference is that an active set method is more careful regarding which variables to saturate, and

has the ability to free a variable that was saturated in a previous iteration. To check optimal solution, the KKT conditions are used. If Lagrange multipliers of the active inequalities are positive, obtained solution can be regarded to optimal point [Härkegård02]. Figure 3.24 describes an active set algorithm for solving. The Lagrangian multipliers used to for optimality checking as follows :

$$A^T\left(Au-b\right)=\begin{pmatrix}B^T & C_0^T\end{pmatrix}\begin{pmatrix}\mu\\ \lambda\end{pmatrix} \tag{3.83}$$

where C_0 contains the rows of C that corresponds to constraints in the working set. μ is associated with equality constraints and λ with the active set constraints in inequality constraints of equation (3.83).

Active set algorithm

1. Let W be the resulting working set from the previous sampling instant, and assign u_0.

2. Rewrite the cost function as

$$\left\|W_u\left(u-u_d\right)\right\|^2+\Upsilon\left\|W_v\left(Bu-v\right)\right\|^2=\left\|\underbrace{\begin{pmatrix}\Upsilon^{\frac{1}{2}}W_vB\\ W_u\end{pmatrix}}_{A}u-\underbrace{\begin{pmatrix}\Upsilon^{\frac{1}{2}}W_vv\\ W_uu_d\end{pmatrix}}_{b}\right\|^2$$

and solve

$$u=\arg\min_u\left\|Au-b\right\|,\ \text{subject to } \underline{u}\le u\le\overline{u}$$

3. Let u_0 be a feasible starting point. A point is feasible if it satisfies

$Bu = v$

$Cu \geq U$ where, $C = \begin{bmatrix} I \\ -I \end{bmatrix}$, $U = \begin{bmatrix} \underline{u} \\ -\overline{u} \end{bmatrix}$

Let the working set W contain (a subset) the active inequality constraints at u_0

for $i = 0,1,2,...$

Given a suboptimal iterate u^i, find the optimal perturbation p, considering the inequality constraints in the working set as equality constraints and disregarding the remaining inequality constraints. Solve

$$\min_p \left\| A\left(u^i + p\right) - b \right\|$$
$$Bp = 0,\ p_i = 0,\ i \in W$$

if $u^i + p$ is feasible

Set $u^{i+1} = u^i + p$ and compute the Lagrange multipliers λ

if all $\lambda \geq 0$

u^{i+1} is the optimal solution. Stop with $u = u^{i+1}$.

else

Remove the constraint associated with the most negative λ from the working set.

else

Determine the maximum step length α such that $u^{i+1} = u^i + \alpha p$ is feasible. Add the bounding constraint at u^{i+1} to the working set.

end

Figure 3.24 Pseudo-code for active set algorithm

Perturbation p and λ needs to be calculated to obtain least square problem.

$$\min_{p} \|Ap - b\| \tag{3.84}$$

Perturbation p is determined as follows:

$$p = (A)^{+} b \tag{3.85}$$

Assumed that p is partitioned as $p = \begin{pmatrix} p_f \\ 0 \end{pmatrix}$, where p_f are the free variables. Let $\dim(p_f) = m_f$ and $A = (A_f \quad A_0)$. This yields

$$\left\| A\left(u^i + p\right) - b \right\| = \left\| A_f p_f - d \right\| \tag{3.86}$$

where $d = b - Au^i$. For $m_f \le k$, the unique minimization given by

$$p_f = \left(A_f\right)^{-1} d \tag{3.87}$$

For $m_f > k$, a parameterization of the minimizing solutions can be obtained from the QR decomposition of A_f^T.

$$p_f = Q_1 \left(R_1^T\right)^{-1} d \tag{3.88}$$

where, $A_f^T = QR = (Q_1 \quad Q_2)\begin{pmatrix} R_1 \\ 0 \end{pmatrix} = Q_1 R_1$

Lagrange multipliers can be obtained as follows:

$$\lambda = C_0 A^T \left(Au - b \right) \tag{3.89}$$

where, $A^T \left(Au - b \right) = C_0^T \lambda$ and $C_0 C_0^T = I$

3.3.6 Implementation of control allocation

An important requirement imposed on the control allocation algorithm is that it should be implementable in a real-time environment. For real-time implementation of control allocation, four algorithms have been previously introduced. The normalizing error is used to gauge control accuracy

$$\varepsilon_a = \frac{\left\| v_d - Bu \right\|_2 - \left\| v_d - Bu_{opt} \right\|_2}{\left\| B \right\|_2} \tag{3.90}$$

The u_{opt} can be determined from the weighted least square (WLSQ) active set method because it converges to the exact solution in a finite number of steps. In this paper, iteration number is set to 100000. Severe turning driving simulation condition is used to verify performance of control allocation methods.

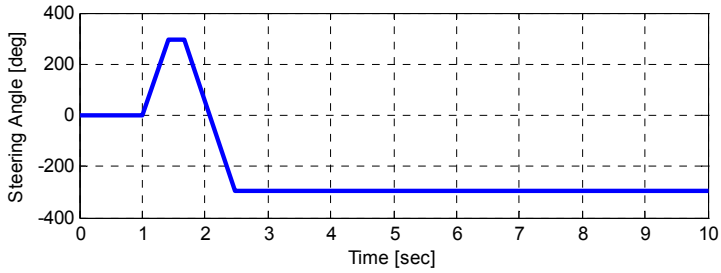

Figure 3.25 Open loop steering input for performance verification of control allocation methods

To verify feasibility of control allocation methods, two simulations with different vehicle velocity conditions have been conducted. In the case of low speed condition, allocated control inputs are unsaturated and less than the actuator limit. If vehicle velocity is fast, control allocation methods may iterate many times to find the optimal solutions. Therefore, execution time of each method on saturated condition is longer than that of the unsaturated condition. For real-time simulation, a step execution time should be shorter than several milliseconds at least. The proper method can be adopted to implement the proposed algorithm for the real-time simulations and tests.

Unsaturated condition of control inputs

Unsaturated control inputs are determined in the case of low vehicle velocity. The initial velocity is 40 km/h. Control inputs of FXP, IP, CGI and WLS are practically similar to the optimal solution which has been obtained by the WLS method with defining maximum iteration as 100,000. The allocated optimal control inputs are determined and less than the actuator limit

according to driving conditions as shown in figure 3.26.

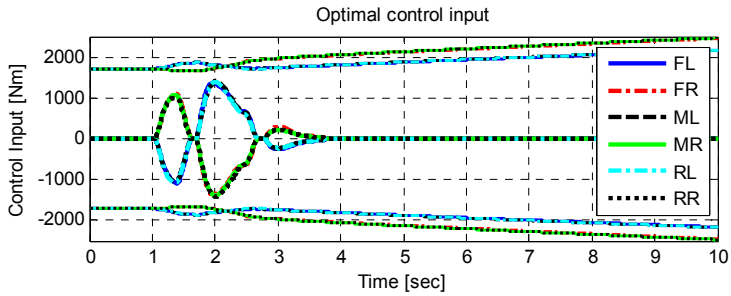

Figure 3.26 Optimal control inputs of control allocation methods (unsaturated condition)

Iteration number of the FXP method is set to constant as 50. And maximum iteration of IP, CGI and WLS is defined as 1000. In unsaturated conditions, control allocation solution can be obtained within several iteration times, excepting the FXP method. The sampling time of all methods is less than 600 microseconds as shown in figure 3.27. Therefore, all methods are suitable for real-time control implementation in the case of unsaturated conditions.

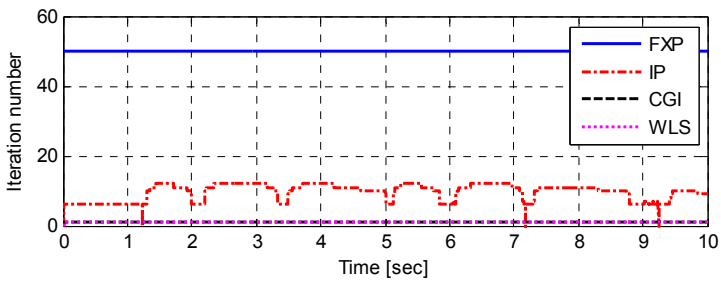

(a) Iteration number

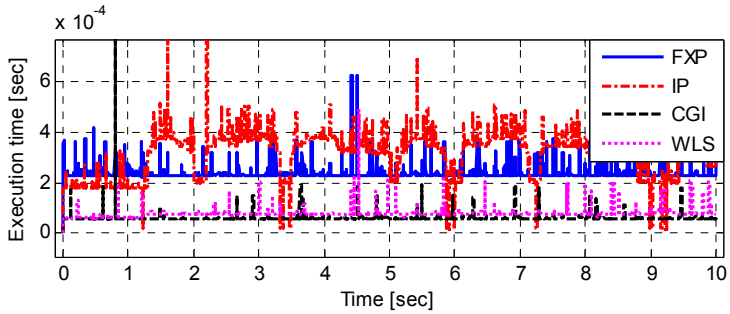

(b) Execution time [sec]

Figure 3.27 One step calculation time for each quadratic problem solver on unsaturated controls

The FXP method calculates the control allocation solution within a feasible period for real-time control systems. Other methods can also determine the solution in less than approximately maximum 500 μs . The average sampling time and mean iteration number are written in detail as shown in table 3.5.

Table 3.5 Mean time and iteration number on unsaturated conditions

Method	Mean time [sec]	Mean iteration
FXP	1.4141e-4	50
IP	3.1666e-4	9.5830
CGI	6.1498e-5	1
WLS	8.6597e-5	1

Saturated condition of control inputs

Saturated control inputs may have to be determined in the case of high vehicle velocity due to high wheel angular velocity and large control inputs. The initial velocity is 60 km/h. Control inputs of FXP, IP, CGI and WLS are almost similar to the optimal solution which has been obtained by the WLS method with defining maximum iteration as 100,000. However, some differences among these control allocation methods exist. The allocated optimal control inputs are saturated by the actuator limit as shown in figure 3.28. Figure 3.28 (a) shows optimal control inputs previously mentioned. Figure 3.28 (b), (c), (d) and (e) represent allocated control inputs and actuator limits of FXP, IP, CGI and WLS.

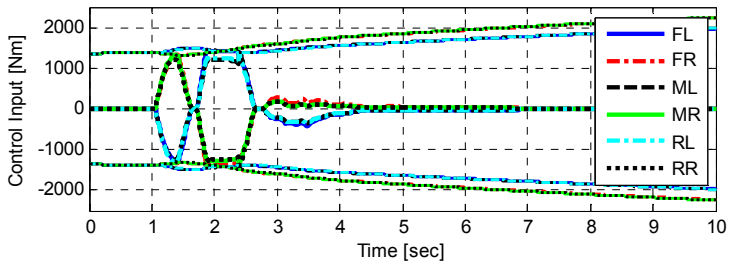

(a) Optimal control inputs [Nm]

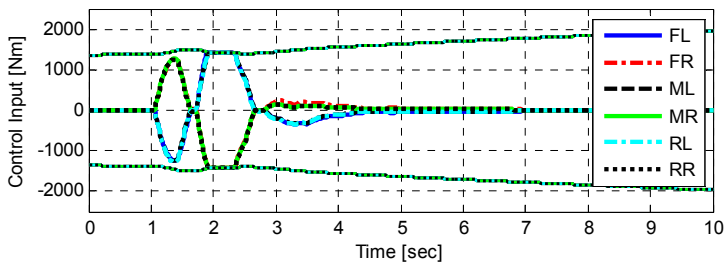

(b) Fixed-point (FXP) control inputs [Nm]

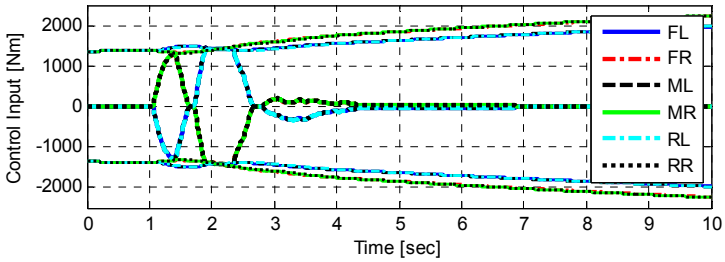

(c) Interior-point (IP) control inputs [Nm]

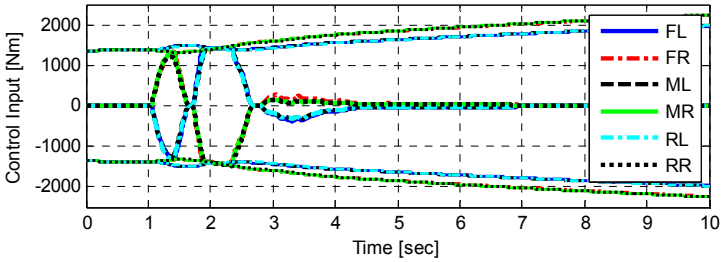

(d) Cascaded generalized inverse (CGI) control inputs [Nm]

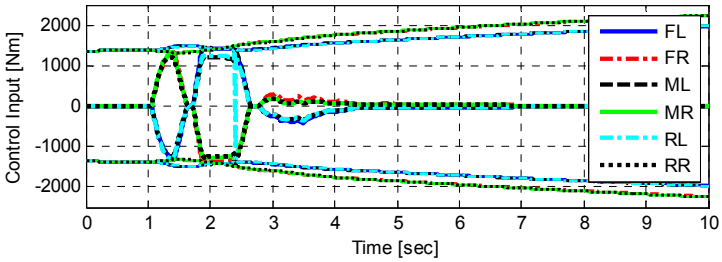

(e) Weighted least square (WLS) control inputs [Nm]

Figure 3.28 Control inputs of control allocation methods includes FXP, IP, CGI and WLS

Normalized error is determined by equation (3.90) and shown in figure 3.29 (a). The WLS error is small compared with errors of other methods. Yaw rate error of optimal control allocation is approximately identical to that of other methods. Deviation of yaw rate error can be defined by subtracting yaw rate error through optimal control inputs from that of other methods. Deviation of yaw rate error can be guaranteed with small values less than 2 deg/s. It is shown that control performance of four control allocation methods is not problem for stability controller of the vehicle.

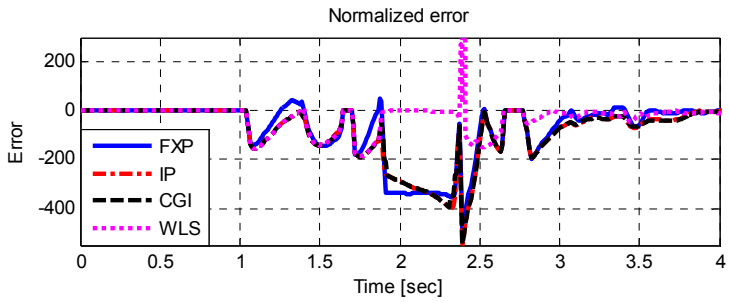

(a) Normalized error

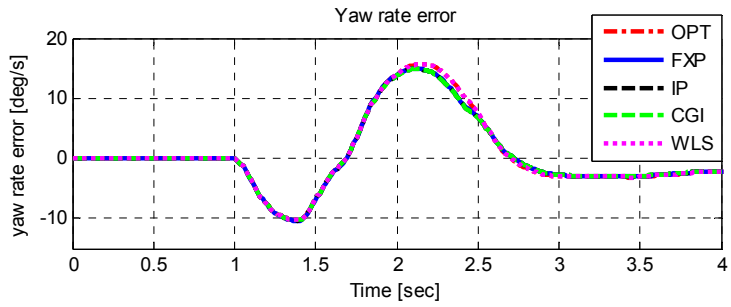

(b) Yaw rate error [deg/s]

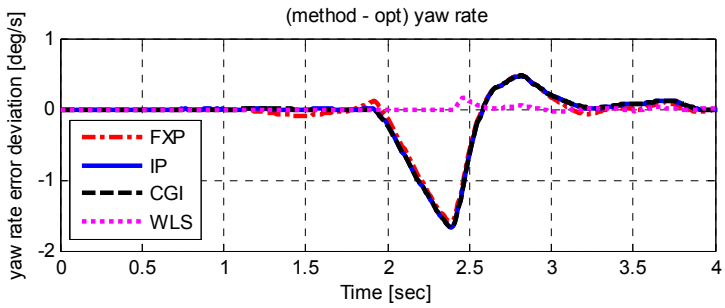

(c) Yaw rate error deviation from the optimal yaw rate error [deg/s]

Figure 3.29 Error comparison among control allocation methods includes FXP, IP, CGI and WLS

Calculation time for finding optimal solutions is important to verify performance of implementing the proposed algorithm to the real-time controller. In the case of saturated conditions, the WLS, IP and CGI methods may have to iterate many times in order to find the solution nearest the optimal one. On the other hand, the FXP method iterates fifty times. Therefore, calculation time is not changed. Figure 3.30 shows iteration number and execution time for conducting a step calculation of this simulation.

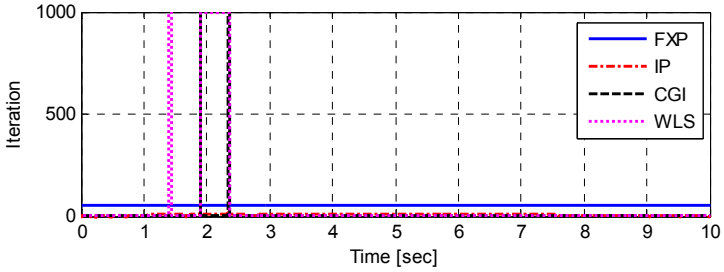

(a) Iteration number

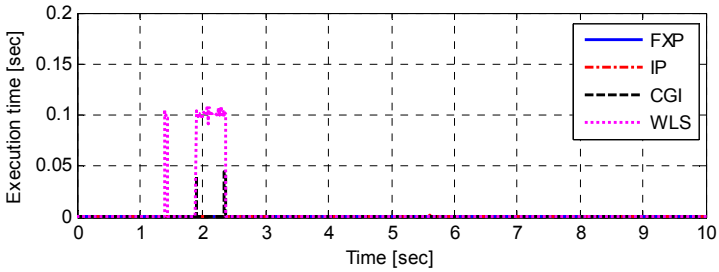

(b) Execution time [sec]

Figure 3.30 One step calculation time for each quadratic problem solver on saturated controls

Table 3.6 represents mean time, maximum time and mean iteration for one step iteration according to control allocation solving methods respectively. The maximum calculation time of IP, CGI and WLS methods is greater than forty milliseconds. It is not suitable for real-time implementation. In this paper, the FXP control allocation method is adopted to develop the proposed control algorithm.

Table 3.6 Mean time and iteration number on saturated conditions

Method	Mean time [sec]	Max time [sec]	Mean iteration
FXP	1.3558e-4	4.6982e-4	50
IP	4.8143e-4	0.0414	8.8929
CGI	1.5419e-4	0.0435	3.0069
WLS	0.0054	0.1393	52.9454

3.4 Power Management Layer

To control series hybrid electric vehicles, power management algorithm should be designed to achieve improved performance of energy efficiency with power distribution of engine/generator, battery and electric in-wheel motors. The power management control layer determines required driving power using motor status information from the driving motor controller and calculates generative engine/generator and battery power.

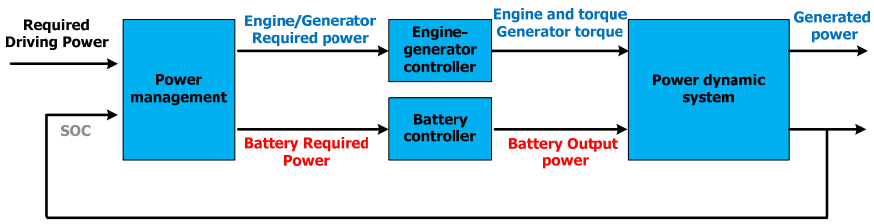

Figure 3.31 Scheme of the power management control layer

3.4.1 Equivalent fuel consumption minimization strategy (ECMS)

To assign the optimized power of each power element, Equivalent Fuel Consumption Minimization Strategy (ECMS) [Paganelli02] is used to reduce fuel consumption in the proposed systems. The power management control system is illustrated as shown in figure 3.32 in detail.

The main objective of the ECMS algorithm is minimizing fuel consumption. This algorithm should coordinate an amount of assigned power of engine/generator and battery in accordance with information of the required

driving power and status of charge (SOC). Engine/generator makes energy to drive the vehicle and charge battery from irreversibly consuming diesel fuel. In general, energy efficiency of engine/generator is relatively less than that of batteries, ultra-capacitors and other electric devices. Batteries can be charged and discharged according to driving conditions. When the vehicle needs to increase velocity significantly, batteries should generate large energy rapidly. On the other hand, batteries can discharge regenerative energy from decelerating motors during braking conditions in order to improve energy efficiency. However, batteries systems cannot generate energy by itself. And it causes energy dissipation related to internal resistance which can be changed in accordance with life cycle and environmental temperature. And then engine/generator should charge batteries. In these features of power system, optimized output power of the engine and batteries should be determined to improve energy efficiency.

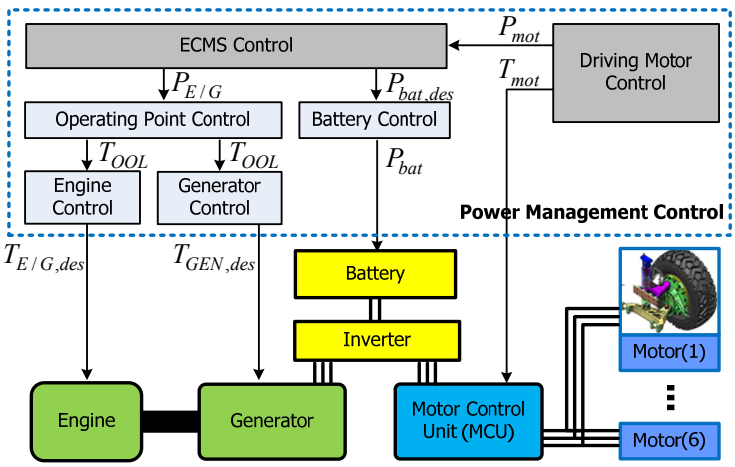

Figure 3.32 Block diagram of power management control system

Map that includes engine/generator and battery information is used to design ECMS algorithm as shown in figure 3.33.

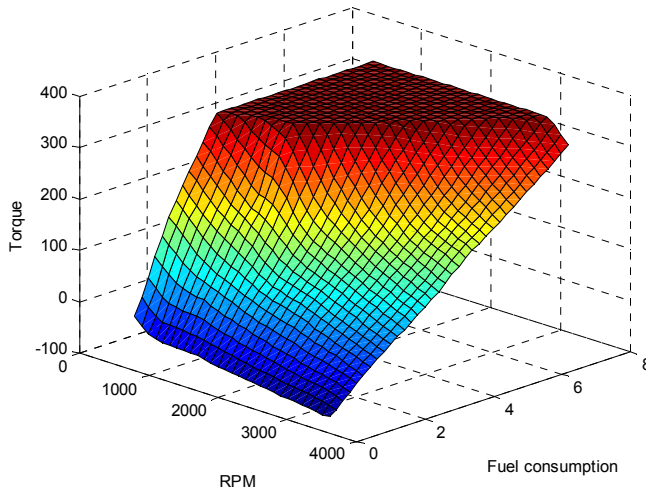

(a) Torque map according to fuel consumption and RPM

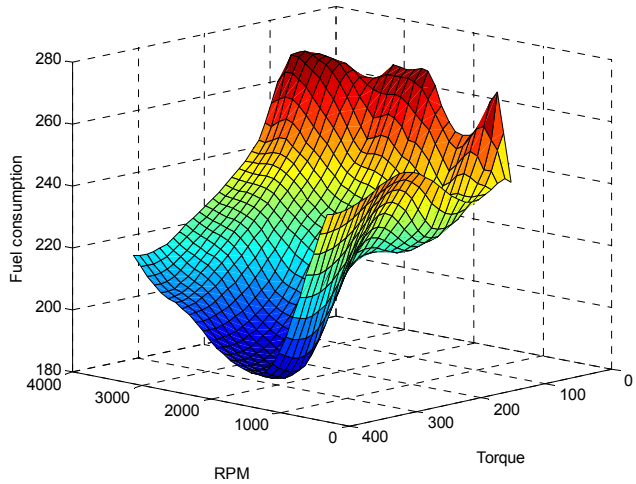

(b) Fuel consumption according to RPM and torque

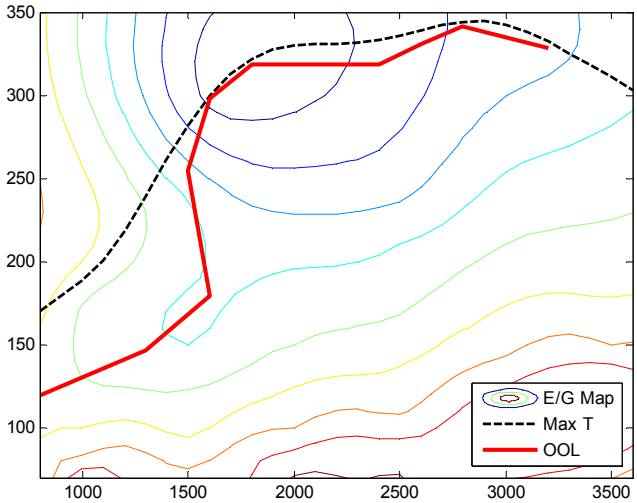

(c) Optimal operating line (OOL)

Figure 3.33 Engine maps and optimal operating line (OOL)

Performance index of ECMS algorithm consists of equivalent fuel consumption for expression of battery energy flow, penalty function related to SOC and diesel fuel consumption of engine as follows:

$$J = \dot{m}_f + \dot{m}_{f,eq} = \dot{m}_f + f_{pen} \cdot S_{bat} \cdot \frac{P_{bat,re}}{H_{LHV}} \tag{3.91}$$

where, $\dot{m}_f$ denotes diesel engine fuel consumption. $\dot{m}_{f,eq}$ is equivalent fuel consumption and can be obtained by conversion efficiency (S_{bat}), battery output power ($P_{bat,re}$) and low heating value (H_{LHV}). The penalty function (f_{pen}) needs to be defined to guarantee battery life cycle as shown in figure 3.34. In general, it is recommended that battery SOC maintain reasonable

voltage level which is determined in accordance with battery characteristics. When SOC level is greater than 0.4 and less than 0.8, penalty function is set to one. In the case of low SOC, penalty function is determined to be greater than one. Then, battery power flow status is charge dominantly. And Engine/ generator needs to generate required driving power and battery charge power simultaneously. On the other hand, when battery SOC is greater than 0.8, most required driving power is generated in battery.

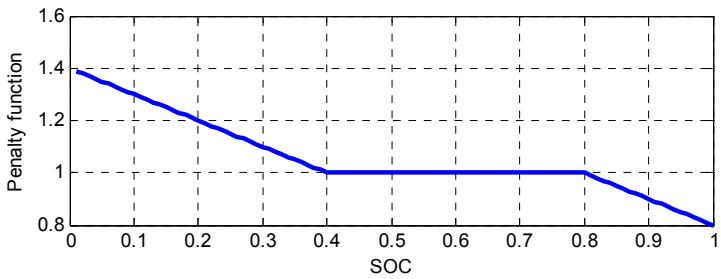

Figure 3.34 Penalty function according to SOC

The optimized control input u denotes the required engine/generator output power. In a very short time, the required driving power is determined as constant value. Then the ECMS control algorithm calculates minimum fuel consumption solution among combinations of feasible generated engine/generator and battery power. Therefore, the ECMS algorithm does not take time-variant power system features in real-time implementation system into account. The control input (engine/generator output power) is determined by using performance index as follows:

$$u = \arg\min_{u \in U} J = \arg\min_{u \in U} \left[\dot{m}_f + f_{pen} \cdot \dot{m}_{f,eq} \right] \tag{3.92}$$

where, $u = P_{req} - P_{bat} = P_{E/G}$

ECMS map definition sequence can be expressed in detail as shown in figure 3.35. In each SOC, ECMS map needs to be defined and selected to improve energy efficiency.

Equivalent Fuel Consumption Minimization Strategy (ECMS) Map Define Sequence

1. Creates combination of generable engine/generator and battery power

$$u = P_{req} - P_{bat} = P_{E/G}$$

For example, total required driving power is 200 [kW]. Generable set is shown in below.

E/G power [kW]	0	1	2	…	199	200
Battery power [kW]	200	199	198	…	1	0

2. Determines equivalent fuel consumption with SOC and required battery power information

$$\dot{m}_{f,eq} = f_{pen} \cdot S_{bat} \cdot \frac{P_{bat,re}}{H_{LHV}}$$

3. In each generable engine/generator power, feasible set of torque and angular velocity is written as follows:

<table>
<tr><td>Battery power [kW]</td><td>200</td><td>199</td><td>198</td><td>…</td><td>1</td><td>0</td></tr>
<tr><td>E/G power [kW]</td><td>0</td><td>1</td><td>2</td><td>…</td><td>199</td><td>200</td></tr>
<tr><td rowspan="5">feasible torque & angular velocity</td><td></td><td>T=1N
ω=1
[rad/s]</td><td>T=1N
ω=2
[rad/s]</td><td></td><td>T=1N
ω=199
[rad/s]</td><td>T=1N
ω=200
[rad/s]</td></tr>
<tr><td></td><td></td><td>T=2N
ω=1
[rad/s]</td><td></td><td>T=2N
ω=99.5
[rad/s]</td><td>T=2N
ω=100
[rad/s]</td></tr>
<tr><td></td><td></td><td></td><td></td><td>…</td><td>T=3N
ω=66.6
[rad/s]</td></tr>
<tr><td></td><td></td><td></td><td></td><td>T=199N
ω=1
[rad/s]</td><td>…</td></tr>
<tr><td></td><td></td><td></td><td></td><td></td><td>T=200N
ω=1
[rad/s]</td></tr>
</table>

4. Using engine and generator efficiency map, fuel consumption is calculated by defined feasible torque and angular velocity in each generable engine/generator output power.

5. Total fuel consumption can be obtained by the sum of the fuel consumption of engine and equivalent fuel consumption multiplied by penalty function.

$$u = \arg\min_{u \in U} J = \arg\min_{u \in U} \left[\dot{m}_f + f_{pen} \cdot \dot{m}_{f,eq} \right]$$

6. Finally, optimal engine/generator output power is selected in each

required driving power on the minimum fuel consumption point.

In the case of 200 kW total required driving power → get optimal engine/generator power **160 kW**

Battery power [kW]	200	…	**40**	…	0
Equivalent fuel [g/s]	48	…	**8**		0
E/G power [kW]	0	…	**160**	…	200
Fuel [g/s]	0	…	**30**		57
Total fuel consumption	48	…	**38**		57

7. Iterates above step with total required driving power range (0 ~ 200 [kW])

8. Iterates above step with SOC range (0.1~0.9)

Figure 3.35 Map definition sequence for the ECMS Algorithm

In the case of low SOC level (SOC < 0.4), engine/generator needs to generate the sum of the required driving power and battery charge power. If SOC level is greater than 0.4 and less than 0.8, amount of engine/generator and battery power are distributed for improving energy efficiency. On the other hand, battery power is dominantly used to satisfy the required driving power in high voltage level (SOC > 0.8). The ECMS maps are determined as shown in figure 3.36. The proposed power system consists of two diesel engines. Therefore, ECMS algorithm takes two engine/generator systems into account and distributes each generable engine/generator power as shown in figure 3.36 (d). If the required engine power is less than 75 kW, one engine is

used to generate the required power. If the required engine/generator power is greater than 75 kW, two engine/generators operate respectively and make identical output power.

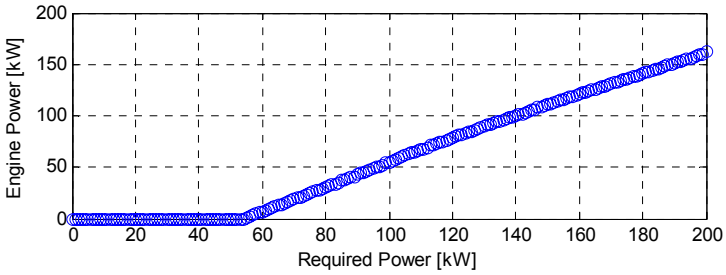

(a) Distributed engine/generator power [kW] (SOC < 0.4)

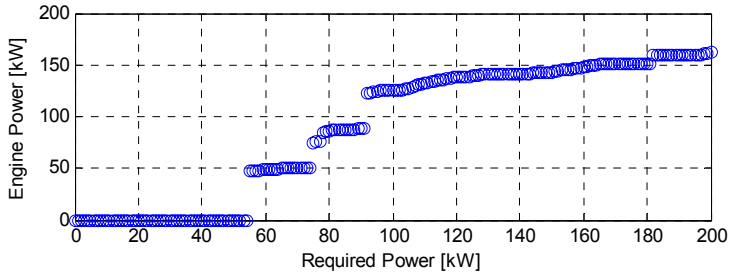

(b) Distributed engine/generator power [kW] (0.4 < SOC < 0.8)

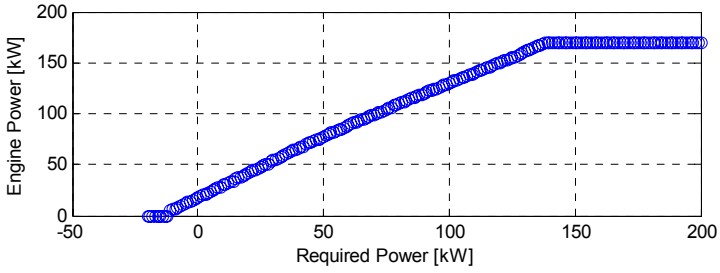

(c) Distributed engine/generator power [kW] (SOC > 0.8)

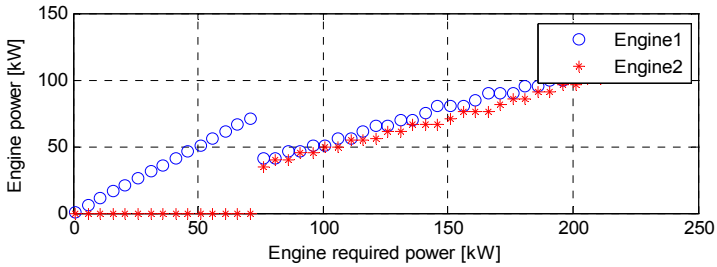

(d) Coordinated engine/generator power (each engine) [kW]

Figure 3.36 ECMS analysis results

3.4.2 Design of engine/generator control algorithm

For ECMS control, engine/generator control is very important. OOL tracking has a large effect on performance of ECMS. In the engine/generator controller, the operating point of engine/generator should be located in the optimal operating line (OOL) defined by efficiency map data in order to improve energy efficiency. The OOL was defined as shown in figure 3.33 (c). The optimal operating torque and angular velocity of engine shaft have been determined by the desired engine/generator output power and OOL map information.

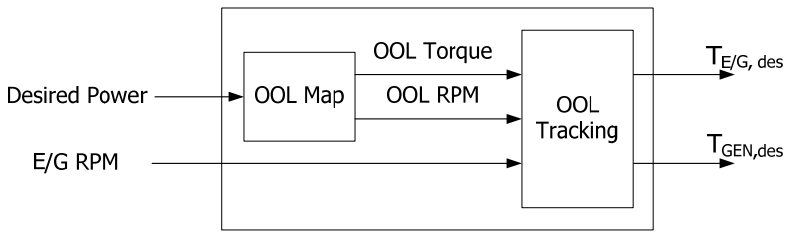

Figure 3.37 Block diagram of engine/generator control algorithm

In general, it is difficult to control the engine torque and speed because response of engine dynamics is relatively slow, compared to response of motor dynamics. For fast OOL tracking, angular velocity control of engine/generator shaft should be conducted. To control angular velocity of engine/generator shaft, the desired generator torque needs to be represented as follows :

$$T_{E/G,des} = T_{OOL} \tag{3.93}$$

$$T_{GEN,des} = -T_{OOL} + PID\left(\omega_{OOL} - \omega_{E/G}\right) \tag{3.94}$$

where, T_{OOL} is optimal operating torque and ω_{OOL} indicates optimal operating angular velocity.

Chapter 4

Estimator Design

For the implementation of the optimal coordination controller, it is necessary to measure vertical tire forces and friction coefficient. The information of the vertical tire forces and the friction coefficient are important in the computation of the optimized additional tire forces. However, these are difficult or very expensive to be measured directly. The friction circle is defined as the maximum tire force which can be generated on each wheel. In other words, the friction circle represents multiplication of the vertical tire force and friction coefficient. Estimating the friction circle is more convenient than estimating the vertical tire force and the friction coefficient separately on off-road driving conditions [Kim10].

The estimator consists of longitudinal tire force estimation, slip ratio estimation and friction circle estimation as shown in figure 4.1. The available sensor signals are the longitudinal vehicle velocity, wheel speed, wheel angular acceleration and wheel torque. The longitudinal vehicle velocity can be obtained from GPS/INS integration system implemented with the

6WD/6WS vehicle.

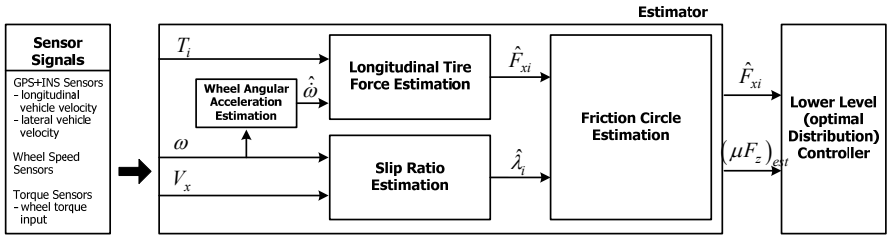

Figure 4.1 The structure of the proposed estimator

Vehicle sensors are interfaced with the controllers using Control Area Network (CAN). Because of measured discrete digital signal from the sensors, the friction circle estimator should take the resolution and noise of sensors into account.

$$\begin{aligned} \hat{v}_x &= \bar{v}_x + n_{v_x} \;, \quad N_x - (0, 0.01) \\ \hat{v}_y &= \bar{v}_y + n_{v_y} \;, \quad N_y - (0, 0.01) \\ \hat{\gamma} &= \bar{\gamma} + n_\gamma \;, \quad N_\gamma - (0, 0.01) \end{aligned} \tag{4.1}$$

4.1 Longitudinal tire force estimation

The longitudinal tire force can be simply estimated using the wheel input torque and wheel angular acceleration based on the wheel dynamics, as shown in equation (4.2).

$$\hat{F}_{xi} = \frac{\hat{T}_i}{r_i} - \frac{J_{\omega i}}{r_i}\dot{\hat{\omega}}_i \tag{4.2}$$

The wheel angular acceleration can be estimated by measuring wheel angular velocity and wheel dynamic equation. The discrete-time state equation of the estimation of the wheel angular acceleration is obtained from the Taylor formula of wheel angular velocity as follows :

$$\omega(t+\Delta T)=\omega(t)+\Delta T\cdot\dot{\omega}(t)+\frac{\Delta T^2}{2}\ddot{\omega}(t)+d_1 \tag{4.3}$$

$$\dot{\omega}(t+\Delta T)=\dot{\omega}(t)+\Delta T\cdot\ddot{\omega}(t)+d_2 \tag{4.4}$$

$$\ddot{\omega}(t+\Delta T)=\ddot{\omega}(t)+d_3 \tag{4.5}$$

where, ΔT is measuring update period and $d_i(k)$ represents higher order terms. The wheel angular velocity can be measured as

$$y(t)=\begin{bmatrix}1 & 0 & 0\end{bmatrix}\cdot\begin{bmatrix}\omega_i(t) & \dot{\omega}_i(t) & \ddot{\omega}_i(t)\end{bmatrix}^T \tag{4.6}$$

As a result, the state equation is expressed by discretizing equation (4.4), (4.5) and (4.6) as (4.7).

$$x(k+1)=\begin{bmatrix}1 & \Delta T & \Delta T^2/2\\ 0 & 1 & \Delta T\\ 0 & 0 & 1\end{bmatrix}\cdot x(k)+\begin{bmatrix}1 & 0 & 0\\ 0 & 1 & 0\\ 0 & 0 & 1\end{bmatrix}\cdot\begin{bmatrix}d_1\\ d_2\\ d_3\end{bmatrix} \tag{4.7}$$

where $x(k)=\begin{bmatrix}\hat{\omega}(k) & \hat{\dot{\omega}}(k) & \hat{\ddot{\omega}}(k)\end{bmatrix}^T$

$$y(k)=\begin{bmatrix}1 & 0 & 0\end{bmatrix}\cdot x(k)+v(k) \tag{4.8}$$

In equation (4.8), $v(k)$ is measurement noise. Suppose $d_i(k)$ and $v(k)$ are zero-mean white noise separately, whose covariance values are $Q(k)$ and $R(k)$ as follows:

$$Q(k) = diag[0 \quad 0 \quad q], \quad R(k) = r \tag{4.9}$$

The angular acceleration can be estimated using Kalman Filter, where $L(k)$ denotes Kalman Filter gain. Finally, the wheel angular acceleration can be obtained with equation (4.10).

$$\hat{x}(k|k) = A_{esti} \cdot \hat{x}(k-1|k-1) + L(k) \cdot \{y(k) - H \cdot A_{esti} \cdot \hat{x}(k-1|k-1)\}$$

$$where,\ A_{esti} = \begin{bmatrix} 1 & \Delta T & \Delta T^2/2 \\ 0 & 1 & \Delta T \\ 0 & 0 & 1 \end{bmatrix},\ H = \begin{bmatrix} 1 & 0 & 0 \end{bmatrix} \tag{4.10}$$

4.2 Friction circle estimation

The slip ratio is estimated by using the longitudinal vehicle velocity and wheel angular velocity. The slip ratio is defined as follows :

$$\begin{cases} \hat{\lambda}_{traction} = \dfrac{r_i\omega_i - \hat{v}_x}{r_i\omega} & \text{(Traction)} \\ \hat{\lambda}_{braking} = \dfrac{-r_i\omega_i + \hat{v}_x}{\hat{v}_x} & \text{(Braking)} \end{cases} \tag{4.11}$$

The friction circle can be estimated using the estimated longitudinal tire force and slip ratio. First, the longitudinal tractive/braking stiffness is defined to grasp road friction conditions and the applied vertical tire force. The longitudinal tractive/braking stiffness changes according to the size of the friction circle. In the case of large friction circle which represents the high friction condition and the applied vertical tire force, the longitudinal tractive/braking stiffness has large value. On the other hand, the small friction circle decreases the longitudinal tractive/braking stiffness. It means that the size of the friction circle is proportional to the longitudinal tractive/braking stiffness which is a gradient of slip ratio-longitudinal tire force relation (Magic formula). The longitudinal tractive/braking stiffness is calculated as follows :

$$C_{xi} = \frac{\hat{F}_{xi}}{\hat{\lambda}_i}. \tag{4.12}$$

The relationship between the estimated friction circle and nominal friction circle as follows :

$$\left(\mu F_z\right)_{est} : \left(\mu F_z\right)_{\text{nominal}} = \left(\frac{\hat{F}_x}{\hat{\lambda}_i}\right) : \left(\frac{F_x}{\lambda_i}\right)_{\text{nominal}} = C_{xi} : C_{x\text{nominal}}. \quad (4.13)$$

The nominal friction circle is defined by friction coefficient and static vertical tire force, which can be measured by tire test and simulation. The size of the friction circle can be determined using proportional relationship between the size of friction circle and longitudinal tractive/braking stiffness. In order to calculate the size of estimated friction circle, the nominal friction circle and nominal longitudinal tractive/braking stiffness are used as a basis. Friction circle can be estimated as follows :

$$\left(\mu F_z\right)_{est} = K \cdot C_{xi} \quad (4.14)$$

$$where,\ K = \frac{\left(\mu F_z\right)_{\text{nominal}}}{C_{x\text{nominal}}},\ \left|\lambda_{\text{i}}\right| \le \left|\lambda_{\text{max}}\right|$$

Constant K is determined by the nominal friction circle and the longitudinal tractive/braking stiffness. The nominal and estimated slip ratio should be in linear range.

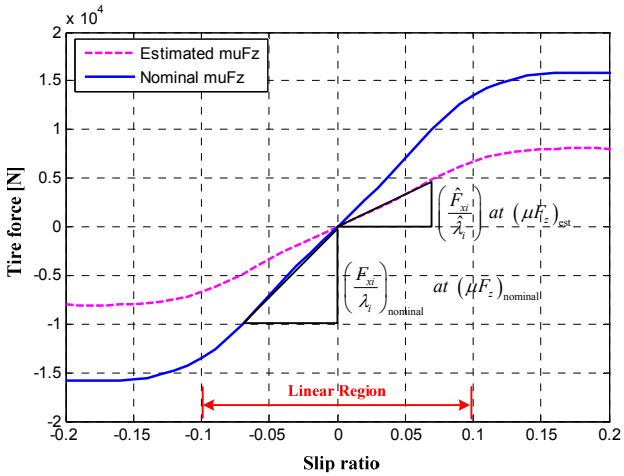

Figure 4.2 The principle of the friction circle estimator

However, if the nominal longitudinal tractive/braking stiffness changes, the friction circle is not estimated accurately. The slope of the longitudinal tire force in the linear range depends on the slip angle as illustrated in figure 4.3. When the vehicle speed is 100 km/h and steering wheel angle is less than 1.5 deg, the slip angle is less than 4 deg, and lateral acceleration is less than 3m/s^2. Figure 4.3 shows comparison of the slip angle and the lateral acceleration when the vehicle is in the stable and unstable region at the 100 km/h. The steering wheel input is sinusoidal, and the frequency is 0.5 Hz. If the magnitude of the steering wheel angle is greater than 1.5 deg, and vehicle velocity is 100 km/h, the vehicle becomes unstable. However, with less than 1.5 deg, slip angle is maintained in a range of -4 to 4 deg and lateral acceleration is in -3 to 3m/s^2.

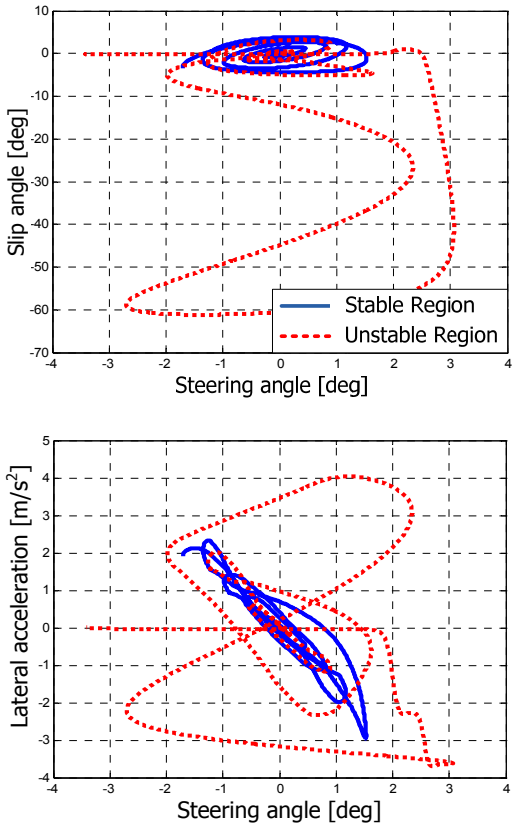

Figure 4.3 Slip angle and lateral acceleration according to steering angle input in the stable region

The slip angle has an effect on the longitudinal tire force slope according to the combined tire dynamics, as shown in figure 4.4. However, when the slip angle is less than 4 deg in the stable region, the effect of the slip angle on the longitudinal tire force slope is slightly affected on the stable region. In this paper, the stability of the vehicle can be guaranteed by the proposed controller

on high speed and severe driving situation. The friction circle estimation can be estimated by the proposed algorithm.

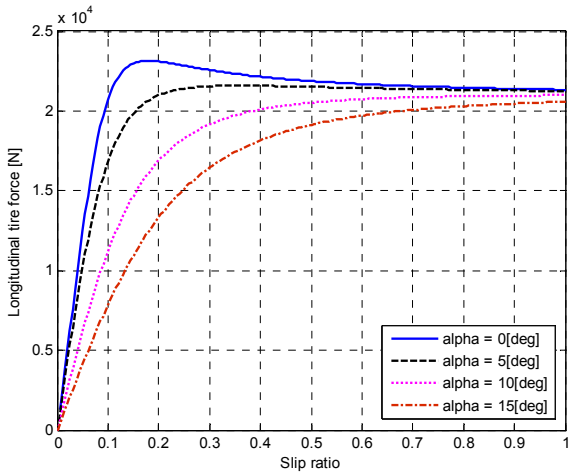

Figure 4.4 Changes of the Slopes of the longitudinal tire force – slip ratio lines due to slip angle

The performance of the friction estimator has been evaluated via computer simulations. A lane change maneuver was conducted and initial velocity sets to 90 km/h. Figure 4.5 (a) to (e) show friction circle estimation results. The longitudinal and lateral tire force estimation results are shown in figure 4.5 (c), (d). Figure 4.5 (e) is the friction circle estimation results. Friction circle estimation result reflects severe friction coefficient change significantly. Vehicle experiences a step change of tire road friction from 0.9 to 0.5 at 3 seconds.

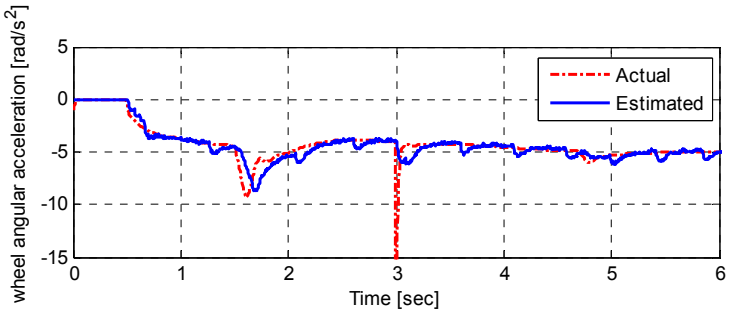

(a) Wheel angular velocity [rad/s^2]

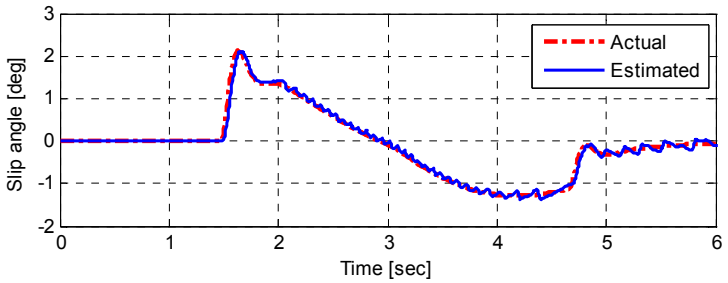

(b) Slip angle [deg]

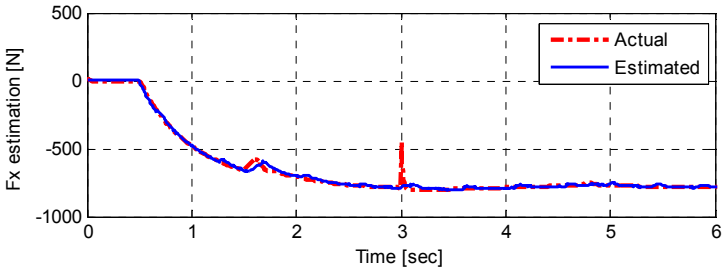

(c) Estimation of longitudinal tire force [N]

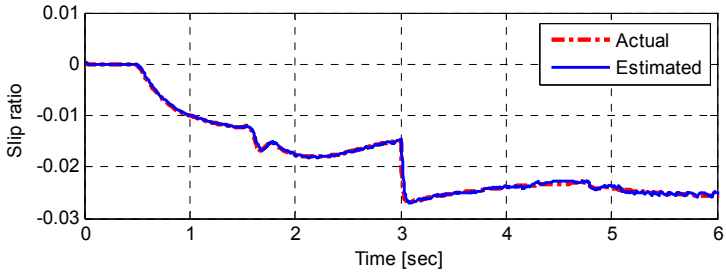

(d) slip ratio

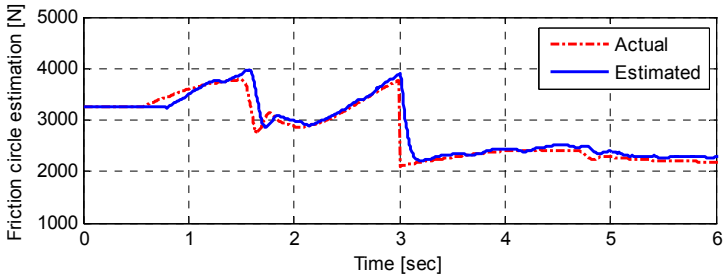

(e) Estimation of friction circle [N]

Figure 4.5 Estimation results of friction circle estimation

Chapter 5

Simulation Results

The proposed integrated driving control algorithm for optimized maneuverability, stability and energy efficiency was evaluated through simulation studies. Simulations with an open-loop and closed-loop driver-vehicle-control system [Kang07] have been conducted to investigate the performance of the integrated driving control algorithm. Steering input and velocity profile of simulations follow formal procedures based on International Standardization Organization (ISO) as shown in table 5.1.

Table 5.1 Test Procedures and Standards for land vehicle control

Standard	Simulation and Test
ISO 7401	Lateral transient response test (step, slalom, pulse)
ISO 7975	Braking in a turning test
ISO 4138	Steady state circular turning test
ISO 3888	Test procedure for a severe lane change maneuver

Comparison cases (even distribution and direct yaw moment control)

Simulation results of a conventional vehicle have been compared to analyze the effectiveness of the proposed control algorithm. Two types of conventional vehicles are developed. The first type vehicle is equipped with mechanical steering, brake and differential gear. Speed controller operates engine and brake systems. In this system, all distributed wheel torques are identical and it can be defined as an even torque distribution system and shown in figure 5.1 (a).

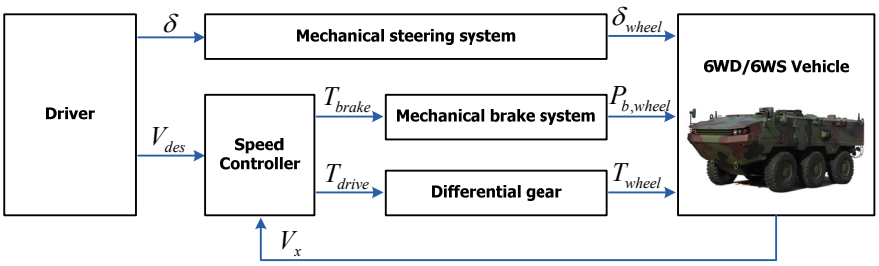

(a) Mechanical drive system (Even distribution)

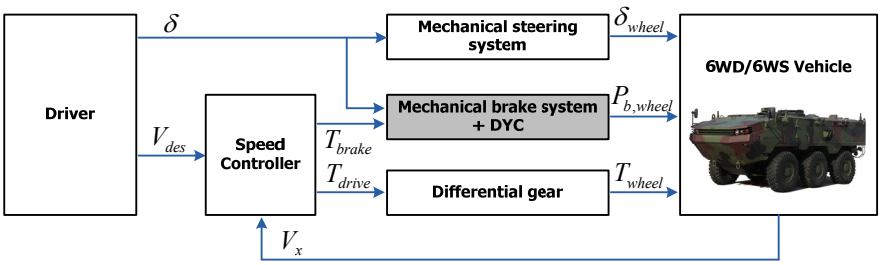

(b) Mechanical drive system equipped with DYC

Figure 5.1 Mechanical system block diagram for performance comparison with the proposed algorithm

The second type vehicle is equipped with mechanical systems which are identical to the first type vehicle. However, for vehicle stability, a direct yaw moment controller has been developed and included into mechanical brake system as shown in figure 5.2 (b). Configuration of compared vehicle systems is illustrated as shown in figure 5.2.

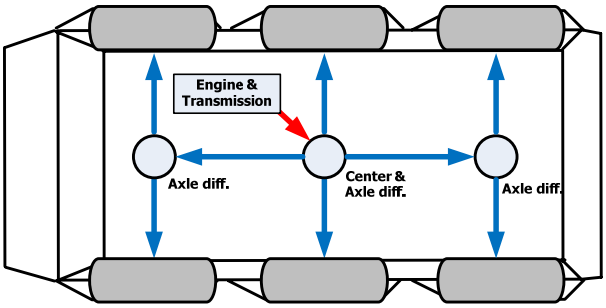

(a) Conventional vehicle with even distribution

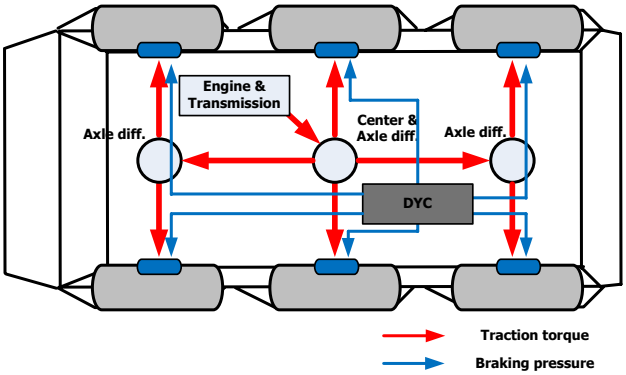

(b) Conventional vehicle with direct yaw moment controller (DYC)

Figure 5.2 Even distribution drive system for conventional vehicle

Distributed output torque is identical to each other. An even torque distribution method is adopted to represent a conventional vehicle equipped with a full differential transmission system. And, mechanical system equipped with direct yaw moment controller (DYC) has been also developed to compare the proposed algorithm with respect to performance of maneuverability and stability. The DYC introduced in this paper is modified appropriately for a 6WD/6WS vehicle. The desired yaw moment is calculated by the upper level controller based on the sliding mode control theory. The upper level control algorithm is identical to that of the proposed control algorithm. Longitudinal brake forces are determined to satisfy yaw moment dynamic equation as follows:

$$M_z = \frac{t}{2}\{-F_{x1} + F_{x2} - F_{x3} + F_{x4} - F_{x5} + F_{x6}\} \tag{5.1}$$

Longitudinal and lateral tire forces in the individual wheels are coupled with each other. The lateral tire force tends to decrease with the increase of the longitudinal one. Also, different geometric feature of each wheel has a different effect on generating yaw moment. In conclusion, a dominant effect wheel is determined through the direction of the desired yaw moment and turning of a 6WD/6WS vehicle. Figure 5.3 shows the change of yaw moment in the case where vehicle is turning left at 80 km/h.

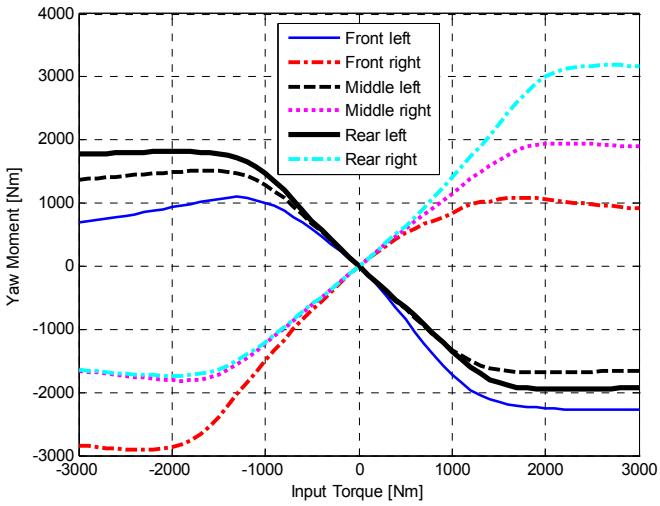

Figure 5.3 Yaw moment generation by individual braking force

The input torque is applied independently to each wheel. To generate yaw moment in the opposite direction, it is most effective to apply input torque on outer front wheel of turning direction. Similarly, to generate yaw moment in the same direction of turning motion, it is most effective to assign input torque on inner rear wheel of turning direction. Table 5.2 shows the effective braking wheel according to the direction of the desired yaw moment. In case I, directions of steering maneuver and required yaw moment are identical and counter-clockwise. Then, the effective braking wheel is rear left wheel. In case II, the direction of steering manoeuvre is counter-clockwise and a direction of required yaw moment is clockwise. Then, the effective wheel is front right wheel. In case III, the directions of steering manoeuvre and required yaw moment are identical and clockwise. Then, the effective braking wheel is rear right wheel. In case IV, the direction of steering maneuver is

clockwise and the direction of required yaw moment is counter-clockwise. Then, the effective braking wheel is front left wheel.

Table 5.2 Effective braking wheel

		Vehicle yaw motion	
		CW(clockwise)	CCW (counter clockwise)
Required yaw moment	CW	Rear right wheel (case III)	Front right wheel (case II)
	CCW	Front left wheel (case IV)	Rear left wheel (case I)

In previous paragraph, the effective braking wheel is chosen by yaw moment controller according to several driving conditions. The braking pressure is applied to braking wheel, which can generate yaw moment. In braking pressure distribution, the effective braking wheel has the largest braking pressure. And, the braking pressure of middle wheel is smaller than that of effective braking wheel, and braking pressure of the other wheel is the smallest one. The lower level controller is designed to use the efficient maximum braking force in order to satisfy the desired yaw moment. The performance of DYC achieves more improvement of lateral stability than conventional DYC like an ESC equipped with general vehicles. Figure 5.4 shows the distribution strategy according to several driving conditions.

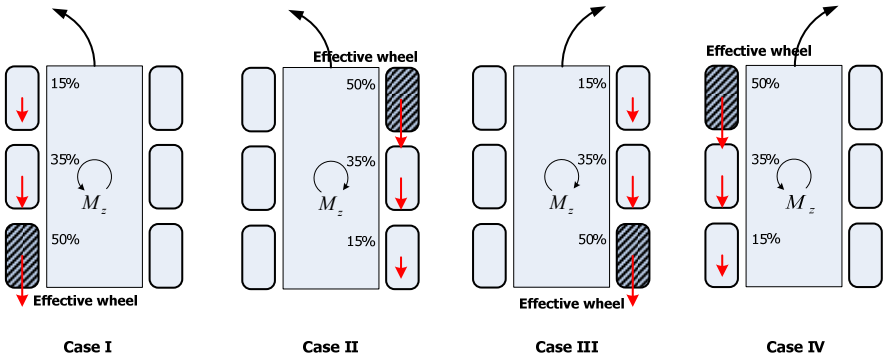

Figure 5.4 Effective wheel according to directions of steering angle and the desired yaw moment

The distributed force of an effective wheel is 50% of total braking force, and the same side middle wheel is 30% percent. The braking force of the other wheel is 15% percent. The distributed force is given in equation (5.2), (5.3), (5.4) and (5.5).

$$\begin{aligned} &Case\ I. \quad M_z = -\frac{t}{2}\left(F_{x1} + F_{x3} + F_{x5}\right), \\ &\qquad F_{x5} = -\frac{M_z}{t}, \quad F_{x3} = 0.7F_{x5}, \quad F_{x1} = 0.3F_{x5} \end{aligned} \tag{5.2}$$

$$\begin{aligned} &Case\ II. \quad M_z = +\frac{t}{2}\left(F_{x2} + F_{x4} + F_{x6}\right), \\ &\qquad F_{x2} = \frac{M_z}{t}, \quad F_{x4} = 0.7F_{x2}, \quad F_{x6} = 0.3F_{x2} \end{aligned} \tag{5.3}$$

$$Case\ III.\ M_z = +\frac{t}{2}\left(F_{x2} + F_{x4} + F_{x6}\right), F_{x6} = \frac{M_z}{t}, \quad F_{x4} = 0.7F_{x6},\ F_{x2} = 0.3F_{x6} \tag{5.4}$$

$$Case\ IV.\ M_z = -\frac{t}{2}\left(F_{x1} + F_{x3} + F_{x5}\right), \quad F_{x1} = -\frac{M_z}{t},\ F_{x3} = 0.7F_{x1},\ F_{x5} = 0.3F_{x1} \tag{5.5}$$

Simulations for algorithm verification of driving performance and stability contain four cases: turning performance with open loop control, closed-loop control, lateral stability, and rollover prevention. The power management algorithm has been also included. Finally, test track simulation is used to verify overall performance of the proposed algorithm with respect to stability, maneuverability and energy efficiency.

5.1 Turning Performance Verification – Open loop Simulation Case

Turning performance verification with open loop simulations was conducted. Step steer, slalom and pulse steer simulation cases based on ISO 7401 are included and steering inputs are determined. The driving control algorithm and conventional vehicle based on even distribution conventional vehicle, simple algorithm, are compared to analyze step responses. Step input steering angle is applied from 0 to 180 deg. In the case of even distribution algorithm of conventional vehicle, it is shown that yaw rate error cannot converge to zero over 80 km/h until 10 seconds. On the other hand, yaw rate error can converge to zero significantly as shown in figure 5.5 (b). The root-mean-square (RMS) value of yaw rate error is expressed according to vehicle velocity in figure 5.5 (d). RMS value of yaw rate error is guaranteed below 2 deg/s in the fixed-point control allocation (FXP CA) case. However, when vehicle velocity increases from 60km/h to faster velocity, RMS of yaw rate error increases in the even distribution case.

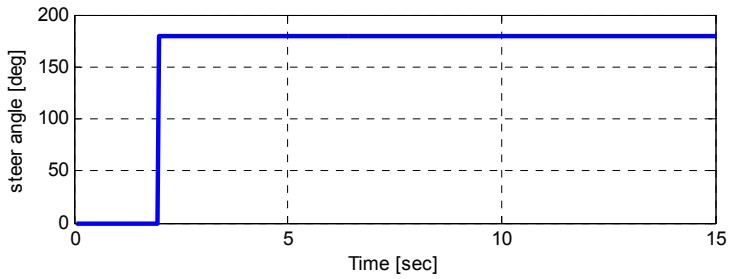

(a) Step steer input [deg]

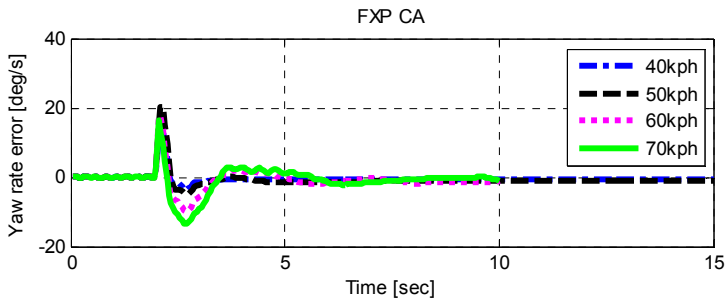

(b) Yaw rate error of FXP CA [deg/s]

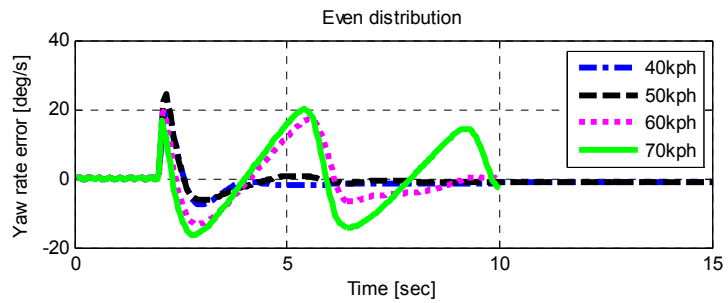

(c) Yaw rate error of even distribution [deg/s]

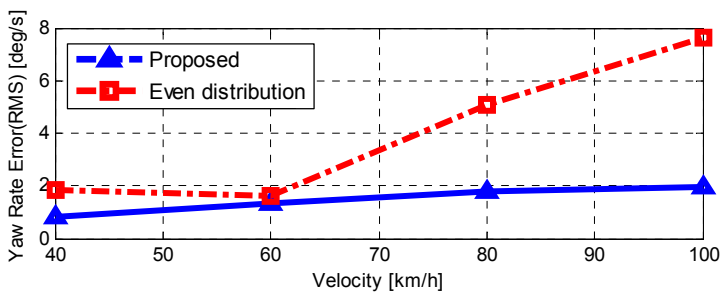

(d) Yaw rate error comparison (RMS) [deg/s]

Figure 5.5 Simulation results of step steer

Slalom input steering angle is applied from -180 to 180 deg and frequency of sinusoidal steer input is 0.25Hz. In the case of even distribution algorithm of conventional vehicle, it is shown that magnitude of yaw rate error is relatively greater than that of FXP CA case as shown in figure 5.6 (d).

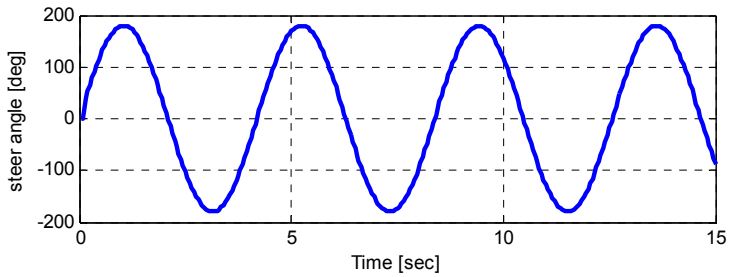

(a) Slalom steer input [deg]

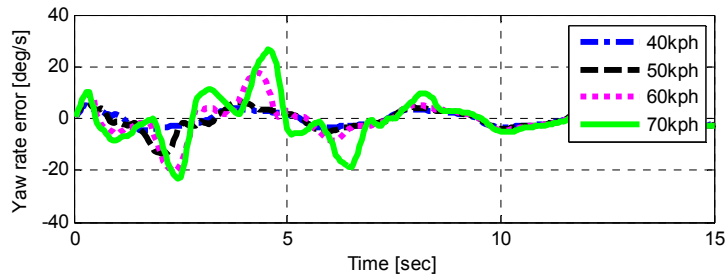

(b) Yaw rate error of FXP CA [deg/s]

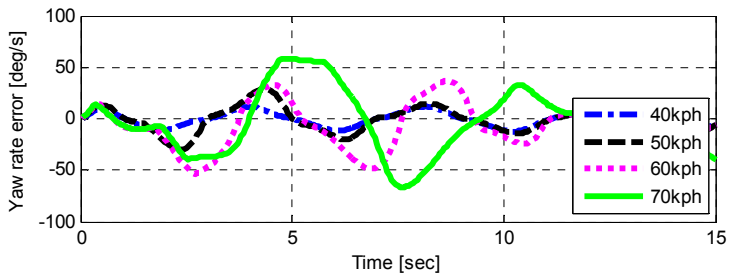

(c) Yaw rate error of even distribution [deg/s]

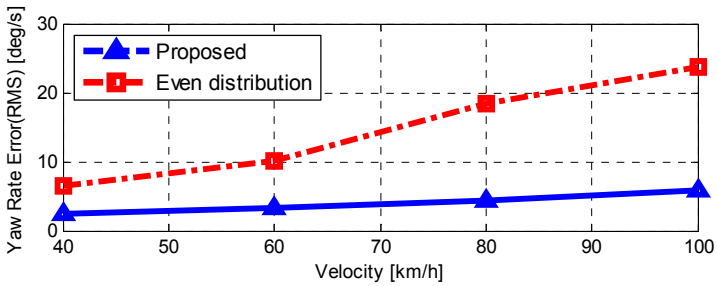

(d) Yaw rate error comparison (RMS) [deg/s]

Figure 5.6 Simulation results of slalom steer

Figure 5.7 (d) shows RMS value of yaw rate error according to vehicle velocity in the pulse steer input simulation case. Difference between even distribution and FXP CA method increases significantly according to increasing the vehicle velocity from 60km/h to 80km/h. When vehicle velocity is 100km/h, RMS value of yaw rate error decreases, compared with 60km/h and 80 km/h. This response is related to over-steer maneuver on fast driving conditions.

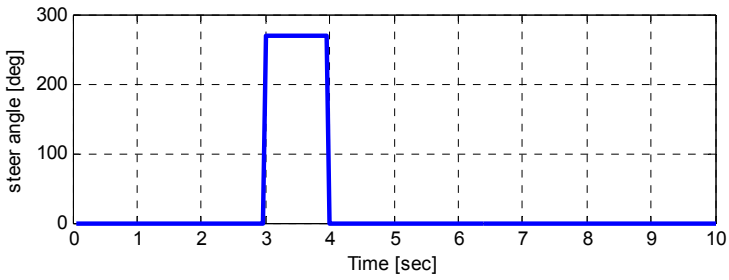

(a) Pulse steer input [deg]

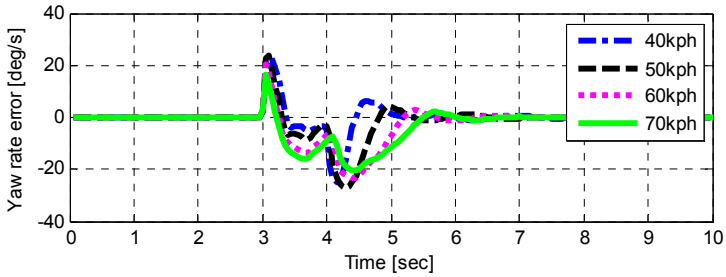

(b) Yaw rate error of FXP CA [deg/s]

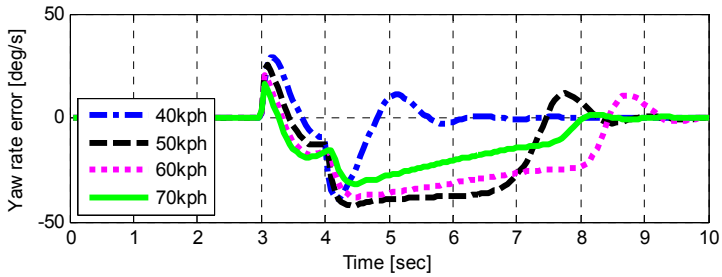

(c) Yaw rate error of even distribution [deg/s]

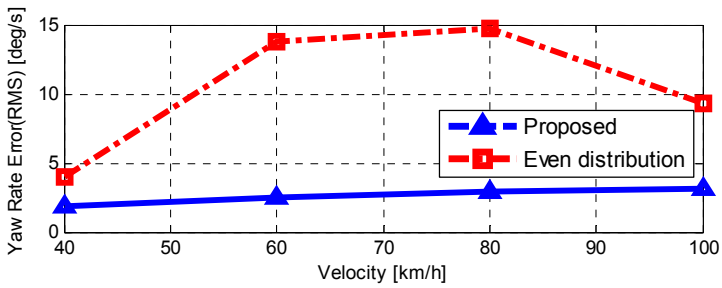

(d) Yaw rate error comparison (RMS) [deg/s]

Figure 5.7 Simulation results of pulse steer

5.2 Turning Performance Verification with Braking Situation – Open Loop

Turning performance verification with open loop simulation was conducted to investigate the maneuverability achieved with the proposed control algorithm. Figure 5.8 shows simulation conditions of steering angle and reference vehicle velocity. Steering angle input increases from 0 to 180 degrees at 1 second and the reference vehicle velocity decreases from 60 km/h to 20 km/h at 2.5 seconds. The deceleration condition consists of three levels: -4m/s2, -6m/s2, -8m/s2.

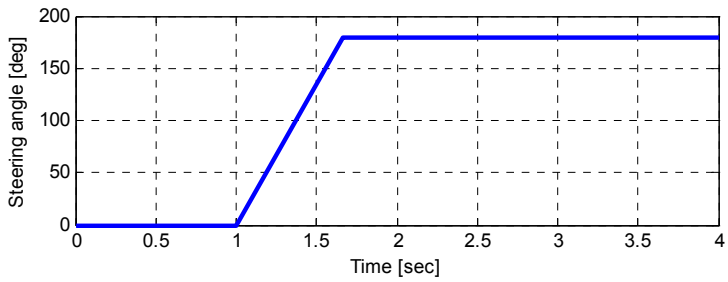

(a) Steering angle [deg]

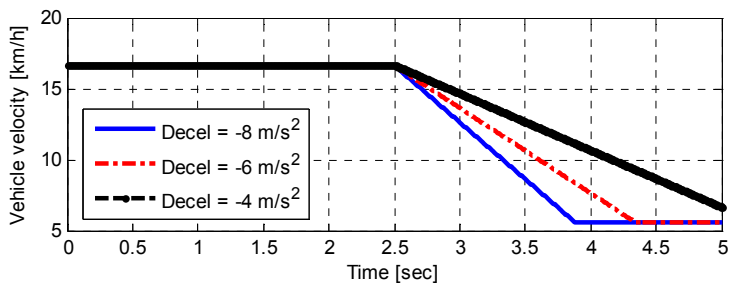

(b) Reference vehicle velocity [km/h]

Figure 5.8 Turning Performance Verification Simulation Conditions

Figure 5.9 shows simulation results of turning performance improvement. Figure 5.9 (a), (b) and (c) represent trajectories of open loop simulation. The even distribution case shows that the vehicle status become unstable when brake commands are applied.

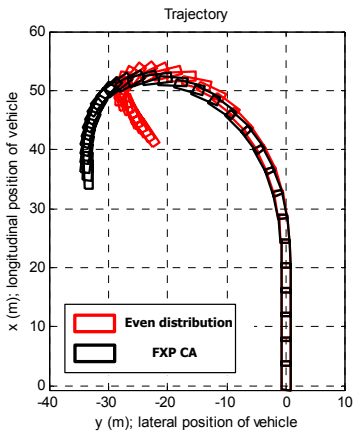

(a) Trajectories (a = -4 m/s^2)

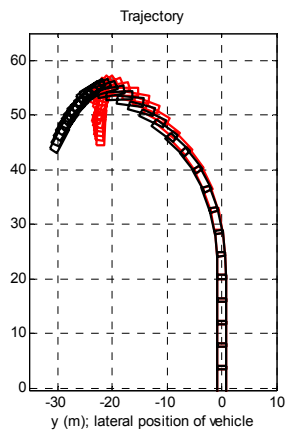

(b) Trajectories (a = -6 m/s^2)

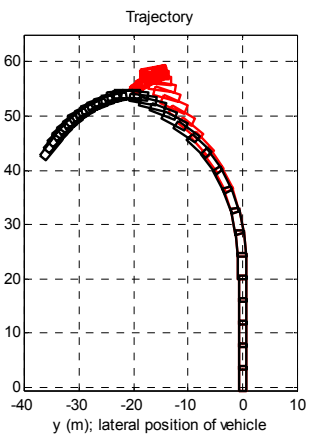

(c) Trajectories (a = -8 m/s^2)

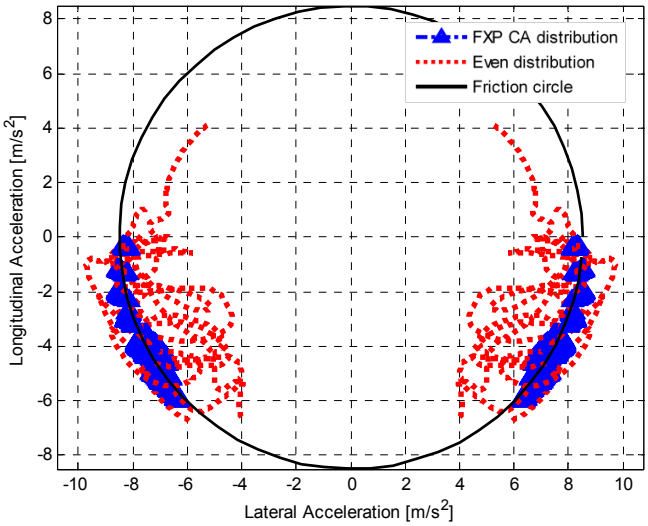

(d) Lateral Acceleration [m/s^2]

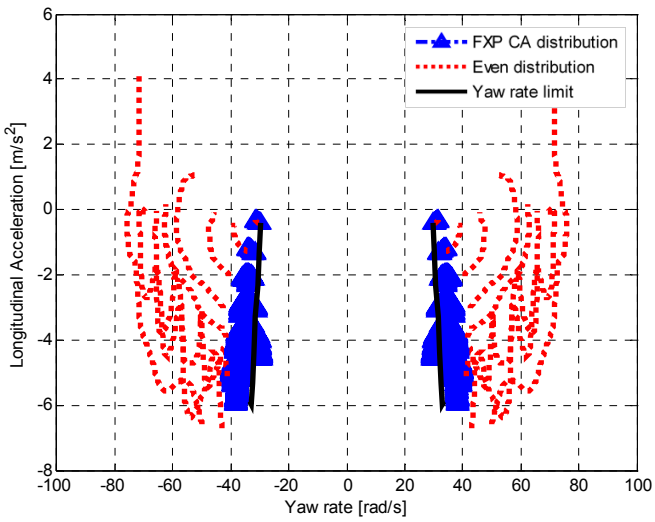

(e) Yaw rate [rad/s]

Figure 5.9 Turning Performance Verification (Open-loop simulation)

The integrated driving control algorithm based on the fixed-point control allocation enhances turning performance and guarantees vehicle stability of the 6WD/6WS vehicle. For more specific verification, analysis of a longitudinal-lateral acceleration plan (g-g diagram) and a longitudinal-yaw rate plan have been performed as shown in figure 5.9 (d) and (e). In figure 5.9 (d), a black solid line represents the friction circle which represents maximum longitudinal and lateral acceleration limits. Blue triangles are located on the friction circle line. This phenomenon shows that the proposed control algorithm can take advantage of the maximum capacity of the turning performance. The red dash line represents acceleration points of even distribution case. Because the vehicle is unstable in over-steer maneuvers, these points are located inside of the friction circle. In figure 5.9 (e), blue triangles are located into the yaw rate limitation line representing maximum turning performance. Due to over-steer maneuvers, red dash line of in the case of even distribution is located outside yaw rate limit line.

5.3 Turning Performance Verification – Closed-loop

Turning performance verification with closed-loop simulation based on a path tracking driver model [Kang07] which has been conducted to investigate the steady state turning performance of the proposed control algorithm. Figure 5.10 shows the reference path and simulation conditions. The turning radius of the reference path is 100m and the vehicle velocity in the simulations ranges from 60 km/h to 100 km/h. Simulation data was obtained during circular turning and has been processed based on the root-mean-square (RMS) method.

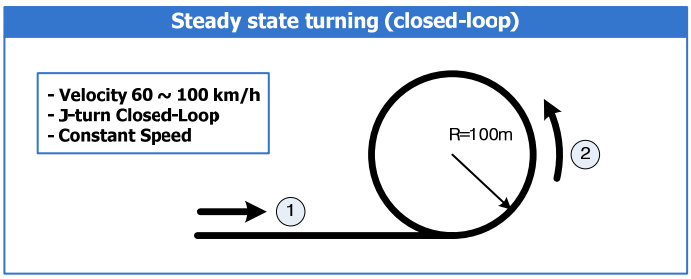

Figure 5.10 Closed-loop Simulation Conditions

Figure 5.11 (a) shows the RMS of lateral error according to vehicle velocity. The difference between even distribution and the fixed-point control allocation is small at 60 km/h. The RMS value of the lateral error increases significantly when increasing the vehicle velocity from 60km/h to 100 km/h. Lateral error is smaller than 1m. From this result, turning performance of the proposed control algorithm is guaranteed in high speed simulation conditions.

Figure 5.11 (b) shows that the steering angle input of driver model increases in order to minimize lateral distance error. The RMS value of the yaw rate error increases until 80km/h and decreases over 90km/h.

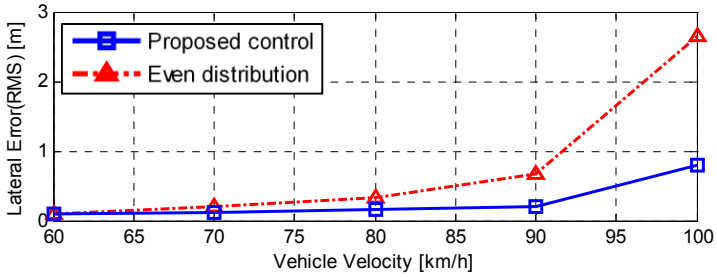

(a) Lateral Error (RMS) [m]

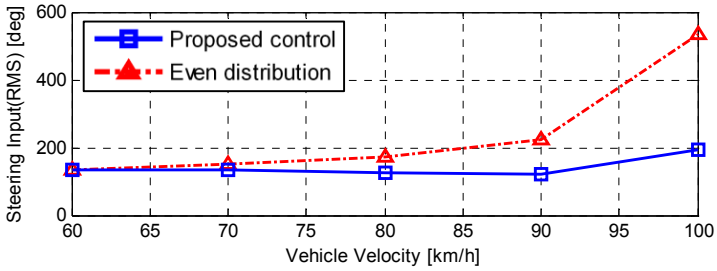

(b) Steering Input (RMS) [deg]

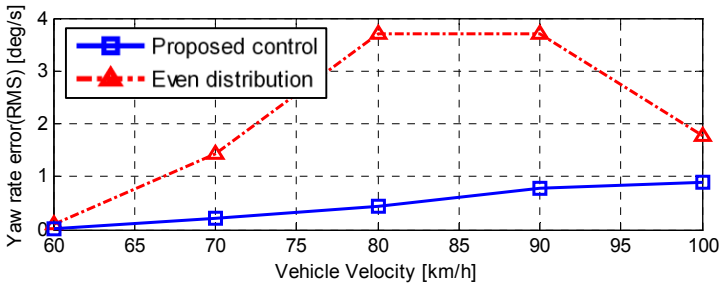

(c) Yaw Rate Error (RMS) [deg/s]

Figure 5.11 Turning Performance Verification (closed-loop) simulation result

5.4 Lateral Stability Verification

In this simulation, when the steering angle is determined by a drive model in order to track the double-lane-change (DLC) reference path that is illustrated as shown in figure 5.12. The reference path of DLC has been modified to adapt simulation conditions for heavy duty vehicles. A DLC maneuver has been simulated on a road with a high friction coefficient ($\mu = 0.85$). The initial vehicle velocity conditions consist of 40, 50, 60 and 70 km/h.

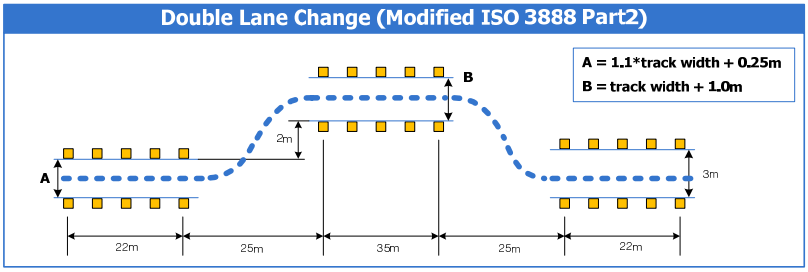

Figure 5.12 Road profile of double lane change

The proposed driving controller enhances performance over that of conventional vehicles with respect to the lateral error and yaw rate error as shown in figure 5.13 (a), (b), (c), (d), (e) and (f). The lateral error and yaw rate error of control method based on proposed control allocation is smaller than those of DYC algorithm and simple control method (even distribution). Because of physical limitations of the target vehicle, the proposed control algorithm could not track the desired yaw rate and lateral error increases significantly in high speed driving condition over 70km/h. In some range, the

lateral error of DYC is less than that of the proposed control method, because vehicle velocity decreases significantly in the DYC method that only uses brake forces for vehicle yaw stability as shown in figure 5.13 (k). On the other hand, the vehicle with even distribution control becomes unstable at over 50km/h because of spin-out. Figure 5.13 (g), (h) and (i) show vehicle trajectories comparison between the proposed, DYC and simple control algorithm. Figure 5.13 (m), and (n) show the RMS value of lateral error according to vehicle velocity. In the case of DYC, the RMS value of the lateral error increases significantly due to increasing the vehicle velocity from 50km/h to 70 km/h. Lateral error of the proposed and DYC control algorithm can be guaranteed to be smaller than 1m. Previously mentioned, due to low vehicle velocity, the lateral error of DYC is a little less than that of the proposed control algorithm. The RMS value of the yaw rate error increases until 60km/h from under steer maneuvering and decreases over 70km/h due to over steer maneuver from unstable driving conditions. From these results, the lateral stability is guaranteed in high speed driving conditions.

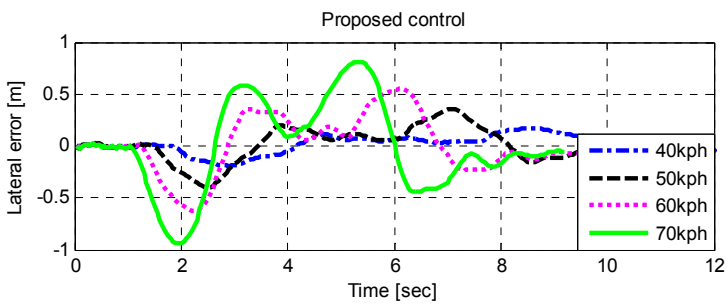

(a) Lateral error [m] (proposed algorithm)

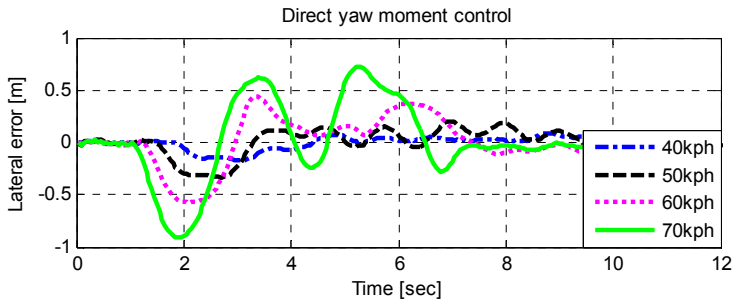

(b) Lateral error [m] (DYC algorithm)

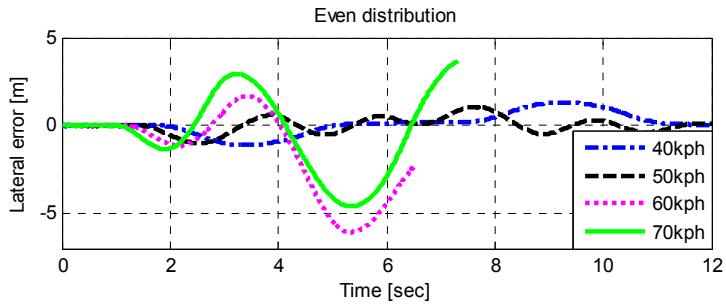

(c) Lateral error [m] (even distribution)

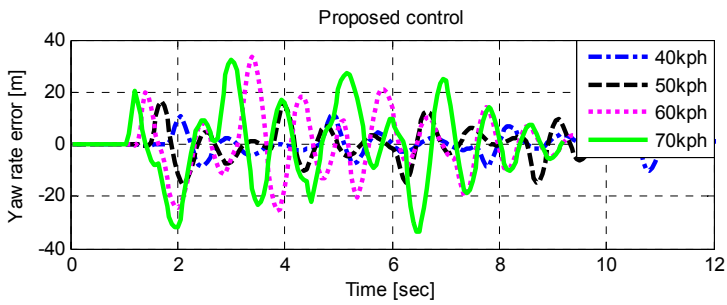

(d) Yaw rate error [deg/s] (proposed algorithm)

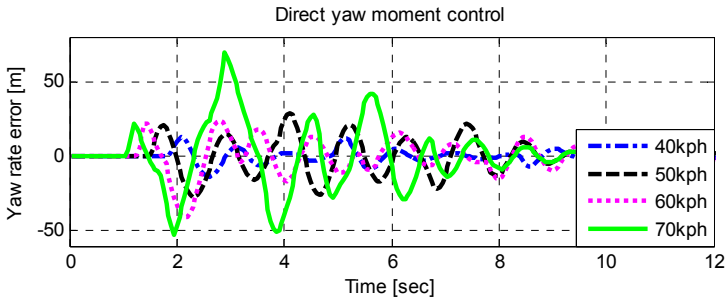

(e) Yaw rate error [deg/s] (DYC)

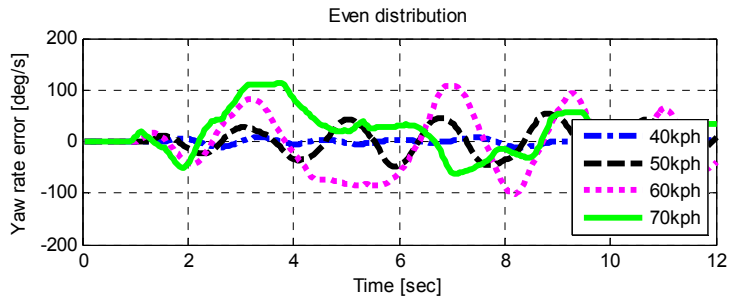

(f) Yaw rate error [deg/s] (even distribution)

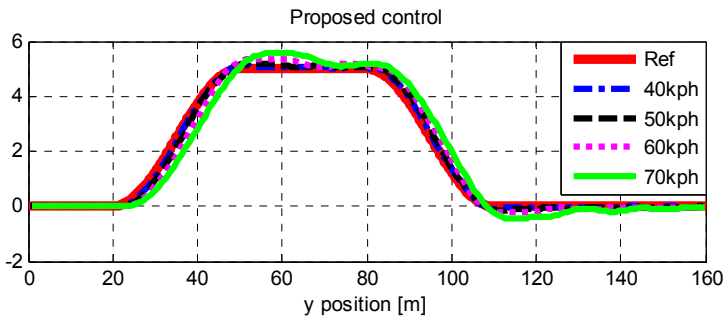

(g) Trajectories [m] (proposed algorithm)

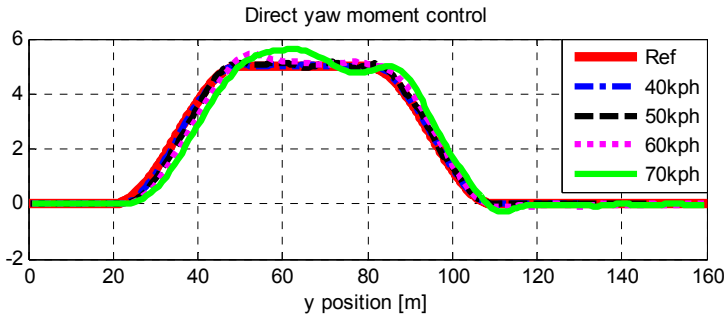

(h) Trajectories [m] (DYC algorithm)

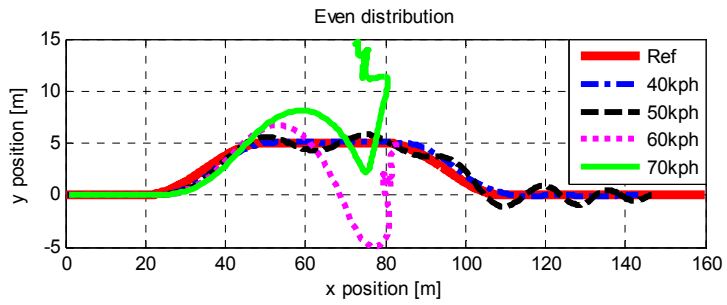

(i) Trajectories [m] (even distribution)

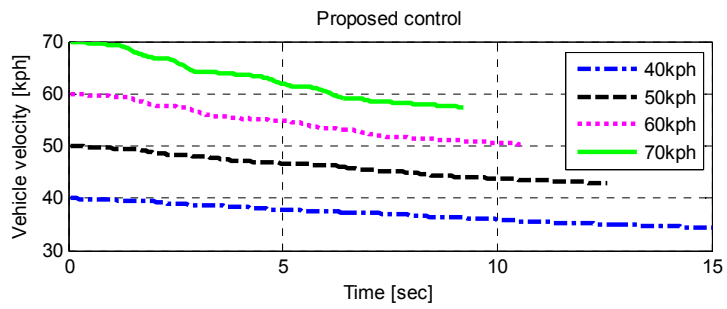

(j) Vehicle velocity [km/h] (proposed algorithm)

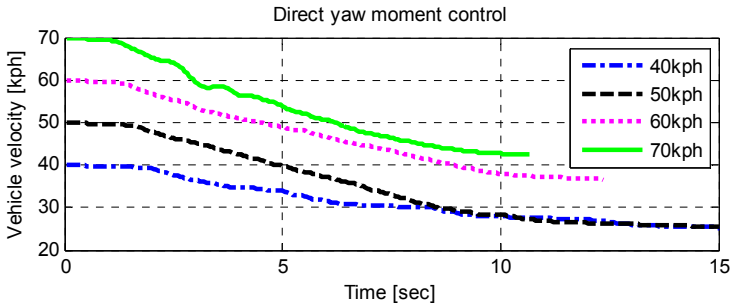

(k) Vehicle velocity [km/h] (DYC)

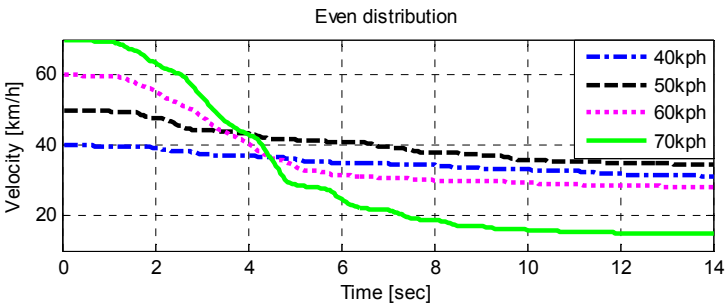

(l) Vehicle velocity [km/h] (even distribution)

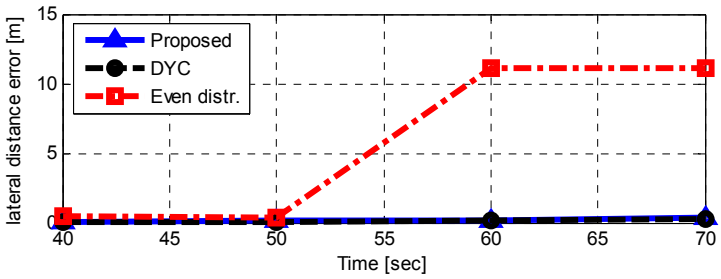

(m) Lateral error comparison (RMS) [m]

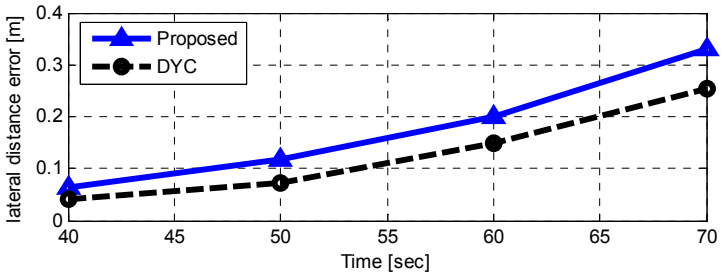

(n) Lateral error comparison (RMS) [deg/s]

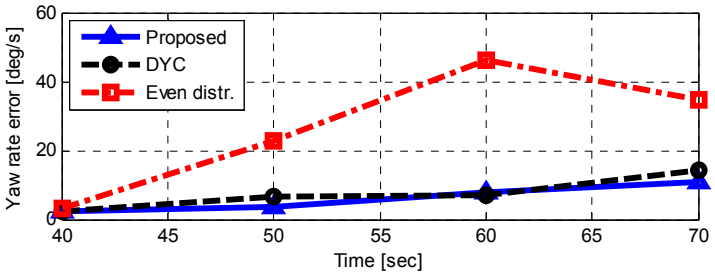

(o) Yaw rate error comparison (RMS) [deg/s]

Figure 5.13 Lateral stability verification (closed-loop) simulation result

Analysis of performance comparison of IDC, DYC and even distribution is written as shown in table 5.3. Analysis results include the RMS and maximum values of lateral distance error and yaw rate error.

Table 5.3 Comparison among the IDC, DYC and even distribution cases

	Vehicle velocity [km/h]	IDC (proposed)	DYC	Even dist.
Lateral distance error (RMS)	40	0.0642	0.0402	0.4548
	50	0.1172	0.0726	0.3417
	60	0.2006	0.1477	11.1064
	70	0.3300	0.2525	11.0911
Yaw rate error (RMS)	40	2.2502	2.4038	3.2958
	50	3.7209	6.6872	22.8818
	60	7.7430	7.0846	46.3557
	70	10.7758	14.1659	34.8883
Lateral distance error (Max)	40	0.1920	0.1706	1.3083
	50	0.3942	0.3340	1.0852
	60	0.6191	0.5749	INF
	70	0.9374	0.9127	INF
Yaw rate error (Max)	40	11.4401	13.5084	11.5895
	50	16.1730	28.8430	54.0042
	60	33.6433	41.0117	108.9917
	70	33.3212	69.5328	112.7027

5.5 Rollover Stability Verification

In this simulation, wheel steering angle is determined by an open-loop steering controller in order to conduct a fish hook test as shown in figure 5.14. A fish hook test has been simulated under high friction coefficient road conditions ($\mu = 0.85$). The initial vehicle speed is 80 km/h.

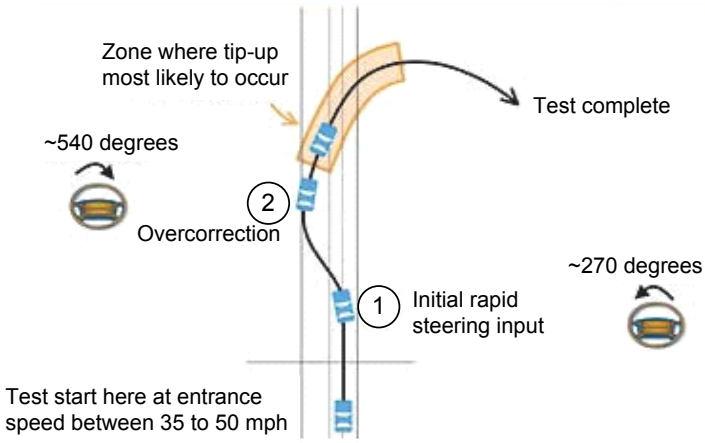

(a) Procedure of fish hook test

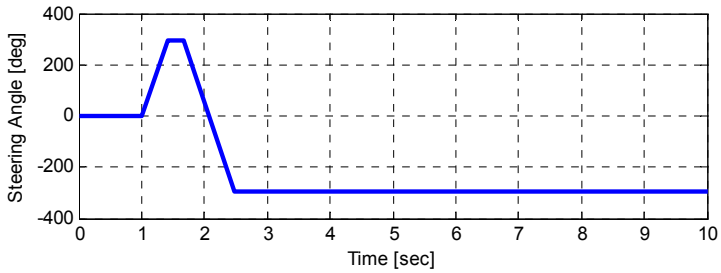

(b) Steering angle of fish hook test

Figure 5.14 Fish hook test for rollover prevention

Figure 5.15 shows rollover stability simulation results in control cases I and II. In control case I, total simulation time is 4.3 seconds and vehicle eventually rolled over. Rollover index (RI) is greater than 1 as shown in figure 5.15 (c). Figure 5.15 (d) shows that roll angle and roll rate begin to diverge from the initial point which is located in the stable region based on the phase plane in the case of even distribution (left graph). In figure 5.15 (a), the longitudinal velocity decreases due to G-vectoring control. The desired longitudinal acceleration is determined to keep from exceeding the limitation of the defined lateral acceleration. Figure 5.15 (d) shows limitations and measurements of lateral acceleration. When measured lateral acceleration is greater than the limitation of lateral acceleration the, target longitudinal acceleration is calculated to reduce the lateral acceleration of the vehicle. Decreasing the longitudinal velocity can prevent exceeding the limitation of lateral acceleration and guarantee rollover stability as shown in figure 5.15 (c). Figure 5.15 (d) shows that roll angle and roll rate are stable. The vehicle roll stability is guaranteed using the GVC of the proposed driving controller.

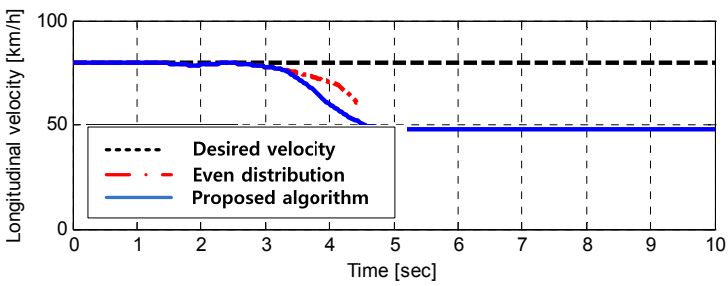

(a) Vehicle velocity [km/h]

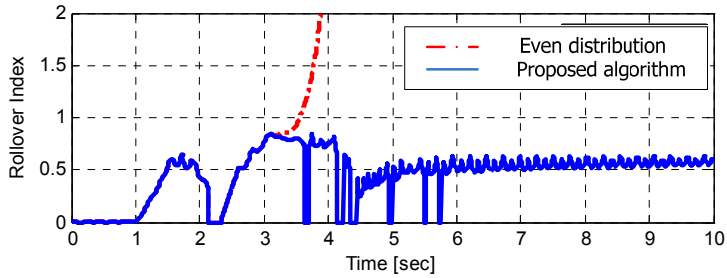

(b) Rollover Index

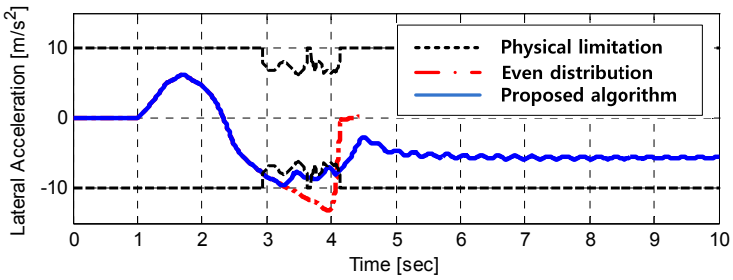

(c) Lateral acceleration [m/s^2]

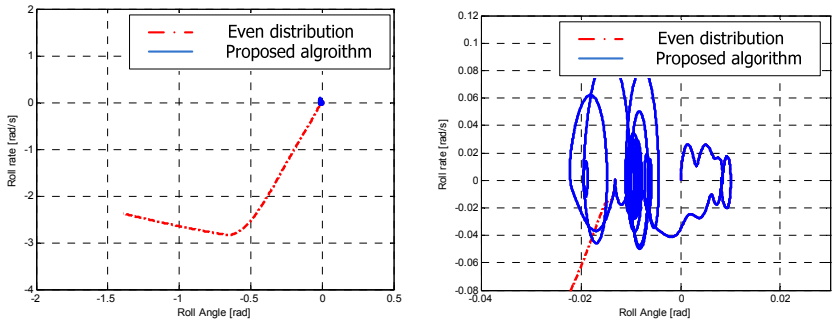

(d) Phase plane of roll angle [rad] and roll rate [rad/s]

Figure 5.15 Simulation Results for Rollover Stability Verification

5.6 Driving Performance Verification for Gradient Road

The climbing performance verification with the gradient road condition has been conducted, compared with the proposed the integrated driving control algorithm based on the control allocation method and even distribution of conventional vehicle. The profile of gradient road angle is shown in figure 5.16. Initial velocity is set to 10 km/h.

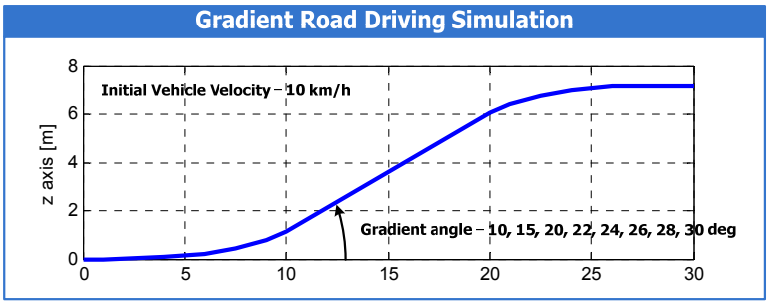

Figure 5.16 Simulation conditions for gradient driving performance verification

Figure 5.17 shows improved gradient driving performance of the proposed control algorithm. Gradient driving performance index has been defined by the desired velocity and measured vehicle longitudinal velocity as follows :

$$Performance = \frac{v_x}{v_{xdes}} \tag{5.6}$$

When gradient road angle increases, performance index gradually decreases. This phenomenon can be explained by increasing driving load which is generated by gravity. If gradient road angel is greater than 20 deg, the decline of gradient driving performance index of the proposed control algorithm is slight, compared to that of even distribution case as shown in figure 5.17 (a). From energy consumption standpoint, the required power is important factor to verify improvement of energy efficiency. In the case of even distribution, although the driving performance is less than that of the proposed control case, large amount of power consumption need to be required as shown in figure 5.17 (b).

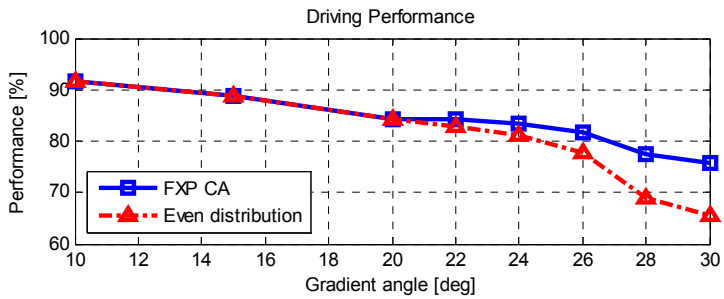

(a) Driving Performance [%]

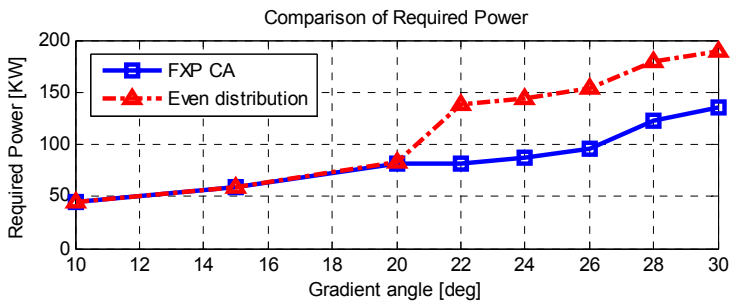

(b) Required Power [N]

Figure 5.17 Simulation results of gradient road driving conditions

5.7 Performance Verification of Energy efficiency improvement

Power management simulations have been conducted to verify performance of energy efficiency improvement. The ECMS algorithm is developed to minimize energy consumption and verified with velocity profiles which contains stop, low and high speed driving conditions. Simulation conditions with only diesel engine and thermostat algorithm are used to compare the performance of the proposed power management algorithm. Capacity of diesel engine is 330 kW. The thermostat represents very simple power management algorithm. If SOC is less than the minimum SOC, thermostat algorithm operates engine/generator in the state of optimal operating point (OOP) until SOC becomes greater than the maximum SOC. The minimum and maximum SOC are defined to guarantee the life of batteries. In general, minimum SOC is set to 0.4 and maximum SOC is 0.8. These values depend on type of battery. Block diagram of the thermostat algorithm is illustrated in detail as shown figure 5.18.

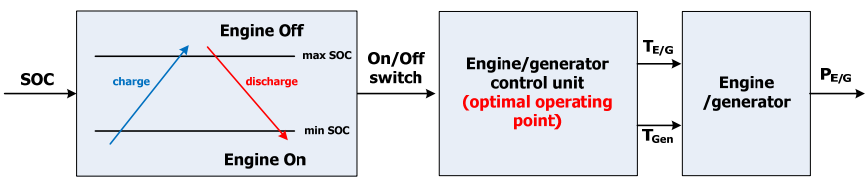

Figure 5.18 Block diagram of thermostat control strategy

Advantages of the thermostat algorithm are simple and able to operate engine/generator on the most efficient operating point. Therefore, minimized energy loss according to transient engine operating can be obtained. On the other hand, when required driving power for fast driving is not generated from the engine/generator, it is difficult to maintain optimal operating. Also, large capacity of battery has to be adopted to cover wide range of driving required power.

Three case simulations have been conducted with the ECMS, thermostat and diesel engine only in 0.2, 0.4 and 0.6 initial SOC for performance comparison of the power management algorithm. The series hybrid system consists of 120kW dual engine and battery. Capacity of discharge is 80 kW and that of charge is 50 kW. In the case of thermostat, the required output engine power is evenly distributed. Detail simulation cases are explained as shown in table 5.4.

Table 5.4 Simulation conditions of ECMS, thermostat and diesel for performance verification

ECMS	THERMOSTAT	DIESEL ONLY
1. Initial SOC 0.6 (120kW dual ECMS)	1. Initial SOC 0.6 (120kW dual even distribution)	No battery 330kW Diesel Engine 6 AT
2. Initial SOC 0.4 (120kW dual ECMS)	2. Initial SOC 0.4 (120kW dual even distribution)	
3. Initial SOC 0.2 (120kW dual ECMS)	3. Initial SOC 0.2 (120kW dual even distribution)	

Figure 5.19 shows the desired velocity profile, throttle and brake command. Throttle and brake commands are determined to satisfy the desired velocity profile.

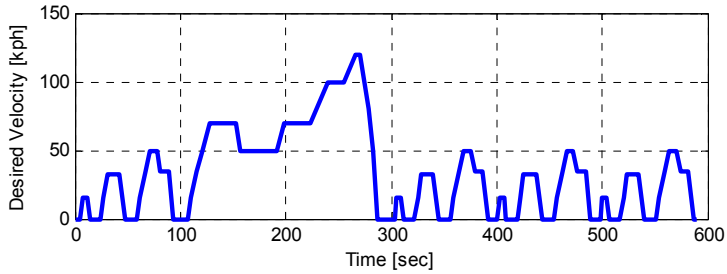

(a) Desired velocity profile [km/h]

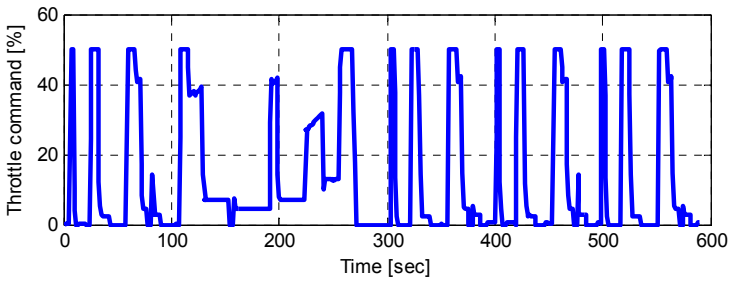

(b) Throttle percent [%]

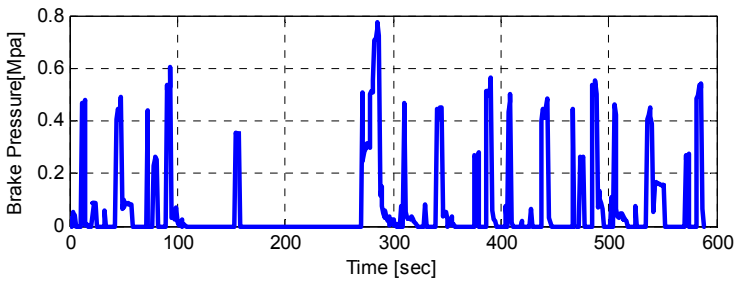

(c) Brake pressure of master cylinder [Mpa]

Figure 5.19 Driver's throttle and brake commands

Figure 5.20 shows simulation results of power management algorithm with 0.6 initial SOC. The ECMS is used to investigate improved performance and compared to thermostat algorithm and diesel engine. The required power of dual engine and battery are determined by the ECMS and thermostat algorithm. The summation of engine and battery output power is total required driving power as shown in figure 5.20 (b) and (c). In the case of thermostat, output power of one of dual engines is identical to that of other engine. When SOC is less than defined minimum SOC, engine/generator starts to charge battery. Final SOC is about 60%. On the other hand, final SOC of ECMS algorithm is less than that of thermostat. Figure 5.20 (d) represents SOC of each case and (e) shows fuel consumption. Fuel consumption of diesel engine case is the largest and that of ECMS case is the smallest among other algorithm.

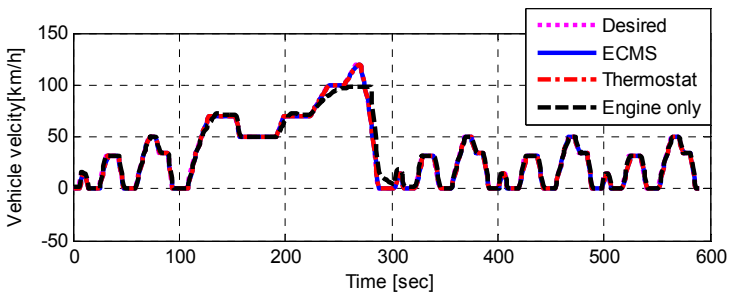

(a) Vehicle velocity [km/h]

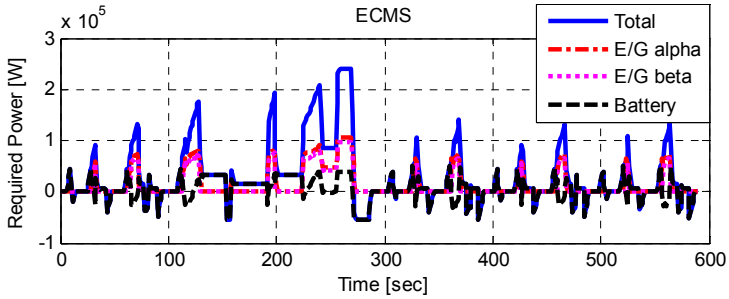

(b) Required power for each power elements [W] (ECMS)

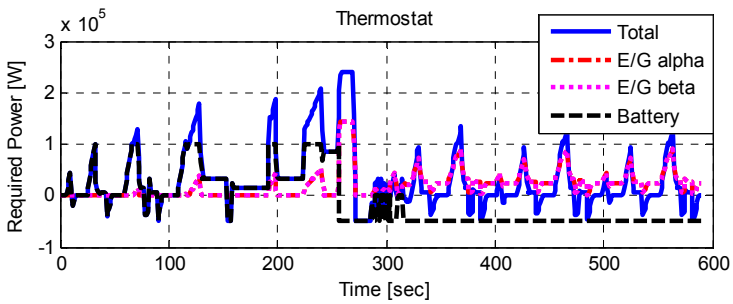

(c) Required power for each power elements [W] (Thermostat)

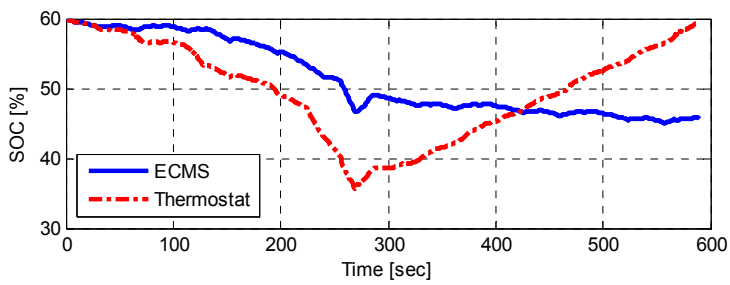

(d) Status of charge (SOC)

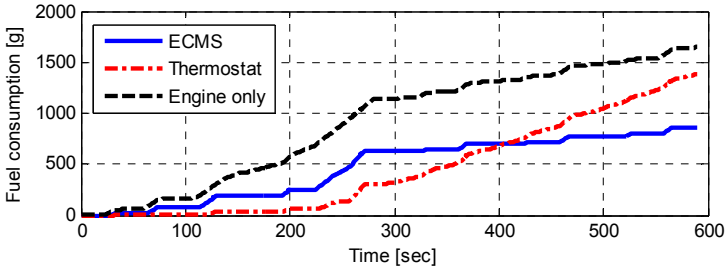

(e) Fuel Consumption [g]

Figure 5.20 Simulation results for initial SOC 0.6

Figure 5.21 shows simulation results of power management algorithm with 0.4 initial SOC. Final SOC of thermostat is about 78% because engine/generator charges battery continuously. Therefore, equivalent fuel consumption is the largest unlike previous results. On the other hand, SOC of ECMS case keeps initial SOC.

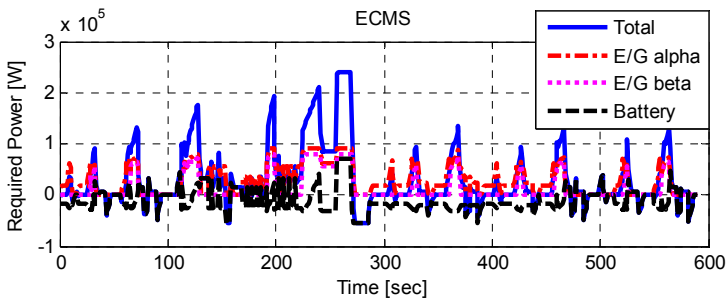

(a) Required power for each power elements [W] (ECMS)

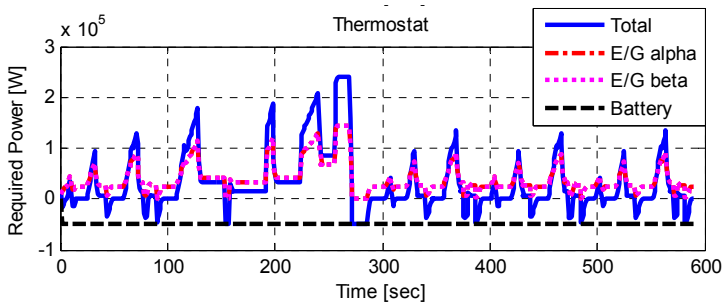

(b) Required power for each power elements [W] (Thermostat)

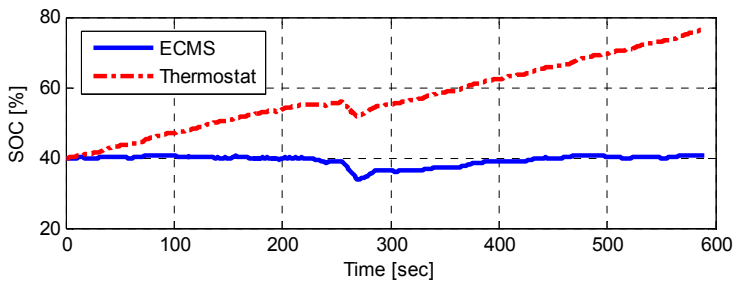

(c) Status of charge (SOC)

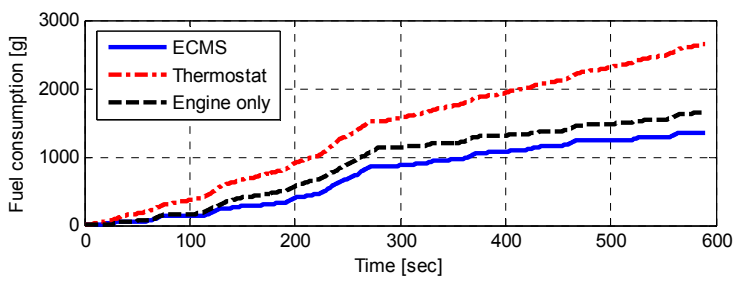

(d) Fuel Consumption [g]

Figure 5.21 Simulation results for initial SOC 0.4

Figure 5.22 shows simulation results of power management algorithm with 0.2 initial SOC. The thermostat algorithm charges constantly due to low SOC of battery. Therefore, generated output power of engine/generator should satisfy the summation of the required driving and discharge power. In the case of ECMS, engine/generator makes most power of the required driving and charge power. However, when the vehicle needs fast acceleration, the battery output power is assigned to support engine/generator for energy efficiency improvement as shown in figure 5.22 (a) and (b).

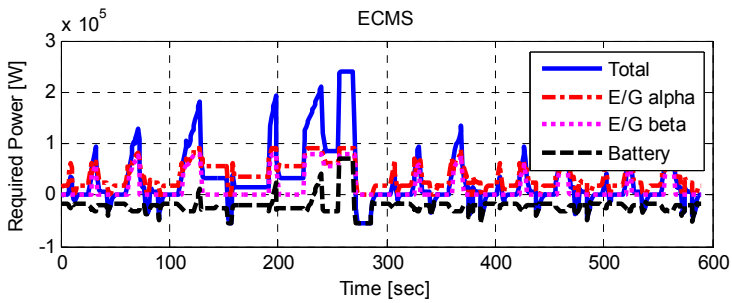

(a) Required power for each power elements [W] (ECMS)

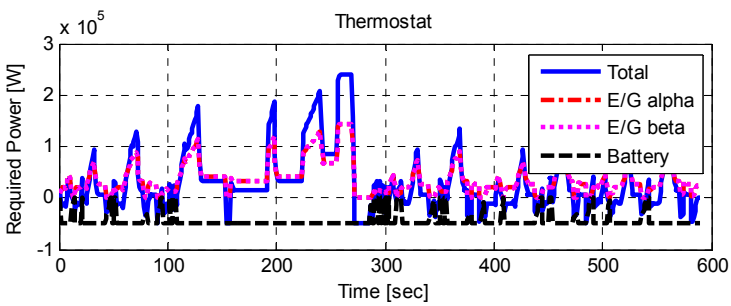

(b) Required power for each power elements [W] (Thermostat)

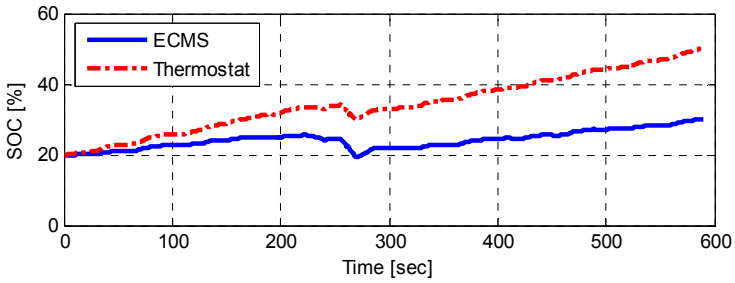

(c) Status of charge (SOC)

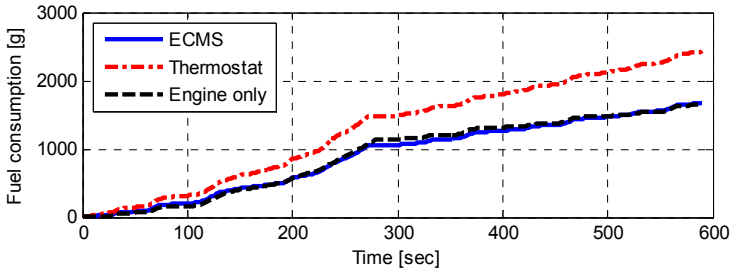

(d) Fuel Consumption [g]

Figure 5.22 Simulation results for initial SOC 0.2

The effect of mismatched SOC at the end of the cycle is compensated for by conducting several simulations with different initial values of SOC. As shown in figure 5.23, the fuel consumption changes monotonically and approximately linearly with the SOC difference. The fuel efficiency with zero SOC variation can be calculated by interpolation.

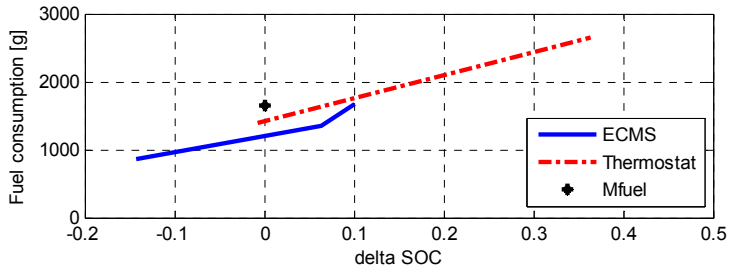

Figure 5.23 Compensation of fuel consumption according to SOC difference

Figure 5.24 shows fuel consumption of the ECMS, thermostat algorithm and only diesel engine according to initial SOC for performance analysis of power management algorithm. In low SOC, both of the ECMS and thermostat algorithms make engine/generator charge battery and provide the required power for vehicle driving simultaneously. In higher SOC, the required power of engine/generator and battery has been evenly distributed in the ECMS algorithm.

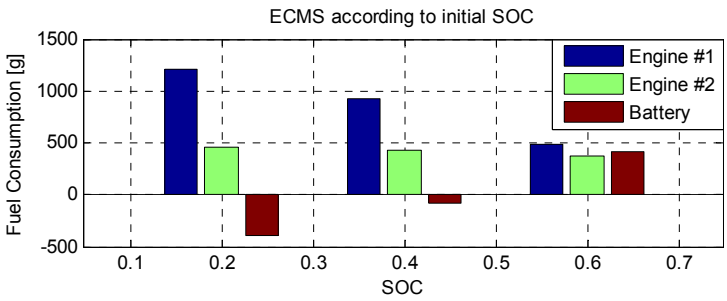

(a) Fuel consumption based on ECMS algorithm [g]

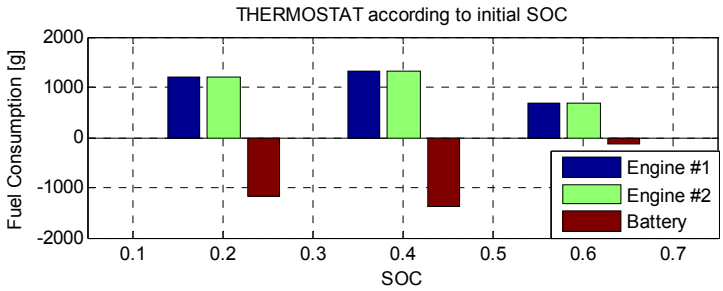

(b) Fuel consumption based on THERMOSTAT algorithm [g]

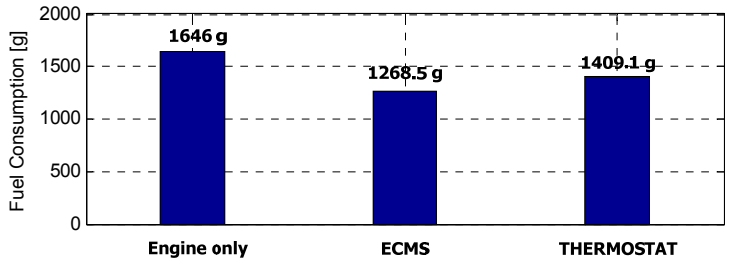

(c) Total equivalent fuel consumption [g]

Figure 5.24 Performance analysis of power management system

The overall equivalent fuel consumption of the thermostat algorithm is reduced to 85.6% in comparison with diesel engine. In the case of ECMS algorithm, fuel consumption is reduced to 77.04%. Detail analysis results are expressed as shown in Table 5.5. From these simulation results, the ECMS algorithm is regarded as more efficient algorithm. Improved performance of the proposed power management algorithm can be obtained in this study.

Table 5.5 Comparison of power management algorithm performance

ECMS	thermostat	Diesel
1268.5 [g]	**1409.1 [g]**	**1646 [g]**
77.04 [%]	**85.6 [%]**	**100 [%]**

5.8 Integrated Performance Verification using Test Track

The integrated driving control algorithm enhances performance of maneuvering, stability and energy efficiency. In this study, test track has been used to verify the integrated performance of the proposed algorithm. Total distance of the test track is 2,880m. The test track consists of various curvature and on-road and off-road. Road geometry of the reference path is shown in figure 5.25. Global positioning data has been obtained by RT3002 which is GPS/INS integrated system.

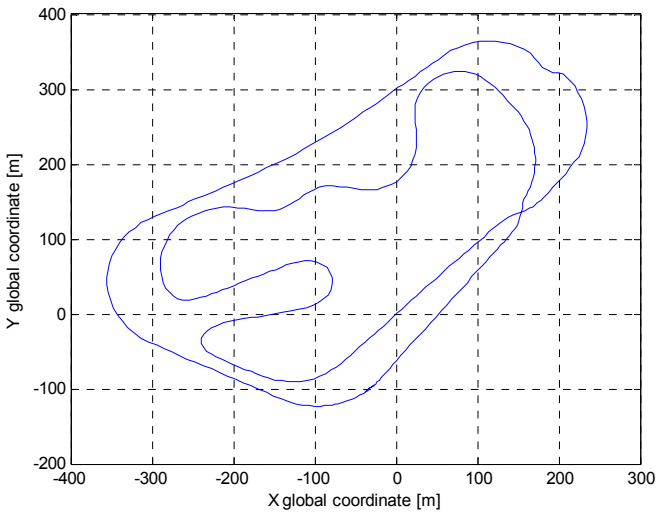

Figure 5.25 Reference path of test track

The desired velocity depends on road curvature. The longitudinal desired velocity should be reduced in small road curvature and increase in large curvature. Figure 5.26 shows the target velocity according to track distance.

The maximum vehicle speed is set to 78 km/h and the minimum speed is 50 km/h.

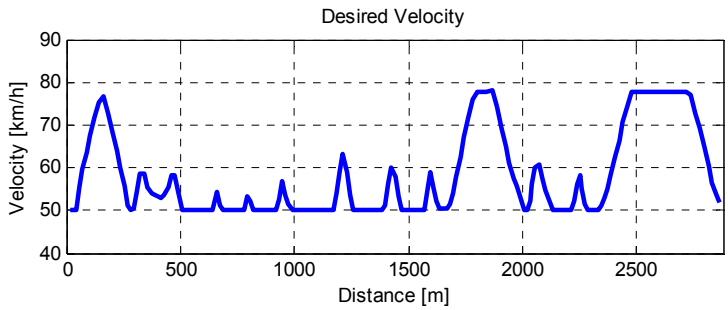

Figure 5.26 Desired velocity according to track distance

The lap time of three cases represents driving performance and can be written in table 5.6. In the case of the integrated driving control algorithm (IDC), the lap time is 186.4 seconds and that is the minimum time among others.

Table 5.6 Lap time of the test track

	IDC	DYC	EVEN
Lap time	**186.4 [sec]**	**190.6 [sec]**	**186.6 [sec]**

Figure 5.27 shows that integrated performance of the proposed algorithm related to maneuvering and energy efficiency is improved, compared to the DYC and even distribution algorithm. The desired longitudinal velocity and measured vehicle velocity of IDC, DYC and even distribution cases are shown in figure 5.27 (a) and (b). The velocity tracking error of DYC case is

greater than that of other cases. In the lateral – angle error diagram, a formatted area which is generated by trajectory of lateral distance and angle error of DYC case is smaller than that of IDC and even distribution cases. This result shows that performance of DYC seems to be most improved. However, this phenomenon can be explained by the lateral distance error and angle error which are located according to the longitudinal velocity error as shown in figure 5.27 (e) and (f). The lateral distance and angle errors are smaller than those of other control cases due to low vehicle speed in the case of DYC. For rapid evasion or avoidance, it is important to guarantee velocity tracking performance. In conclusion, the IDC algorithm is useful for the proposed platform.

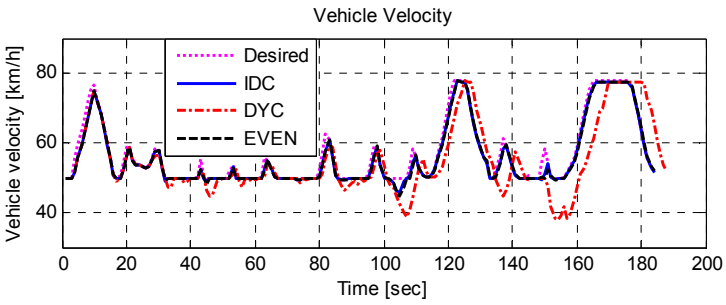

(a) Vehicle velocity [km/h]

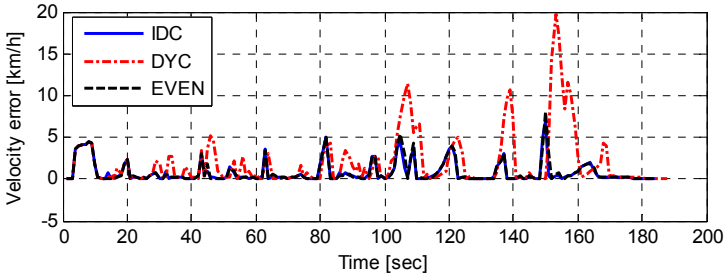

(b) Velocity error [km/h]

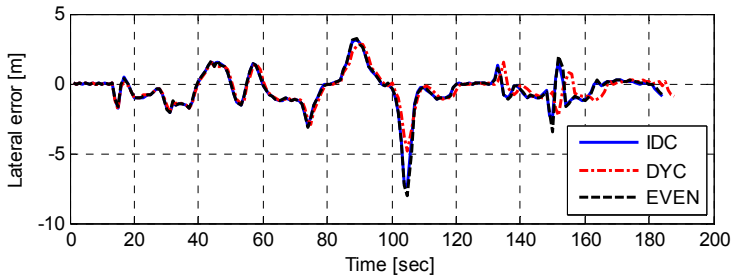

(c) Lateral distance error [m]

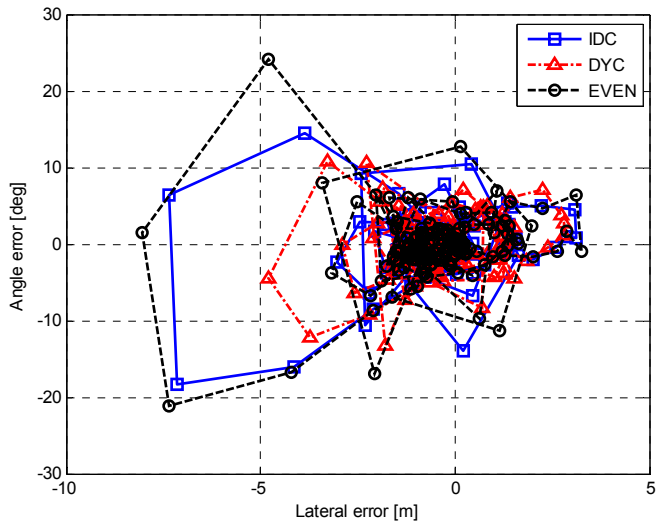

(d) Lateral – angle error [m-deg]

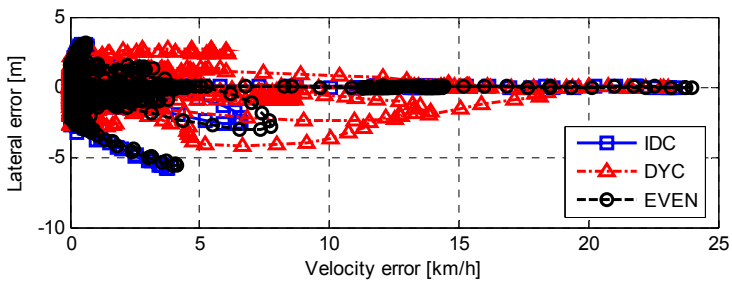

(e) Velocity – lateral distance error [km/h-m]

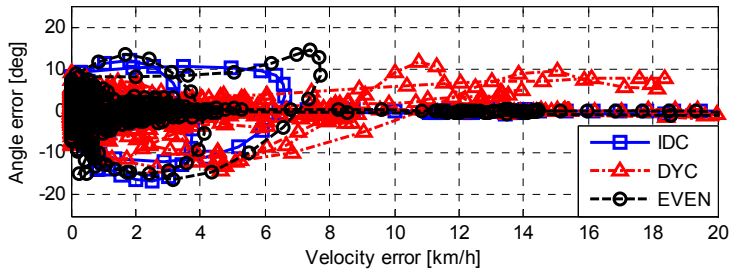

(f) Velocity – angle error [km/h-deg]

Figure 5.27 Maneuver performance comparisons among IDC, DYC and even distribution

Figure 5.28 shows simulation results for energy efficiency performance verification with the proposed algorithm based on equivalent fuel consumption minimization strategy (ECMS) method, compared with the thermostat simple method and diesel engine only. In the case of ECMS, the SOC of the integrated driving control (IDC) algorithm is greater than that of direct yaw moment control (DYC) and even distribution algorithm. That means energy dissipation of battery in IDC case is relatively small. And the SOC of DYC is higher than that of even distribution as shown in figure 5.28 (a) and (b). Fuel consumption of IDC is also minimum value. Figure 5.28 (c) and (d) show that result of the thermostat algorithm is similar to the ECMS algorithm. The most obvious difference compared with the ECMS case is that the fuel consumption in the early driving is not large, because battery energy is dominantly used to control the vehicle velocity. Fuel consumption of diesel engine is especially larger than amount of used fuel in other cases and shown in figure 5.28 (e).

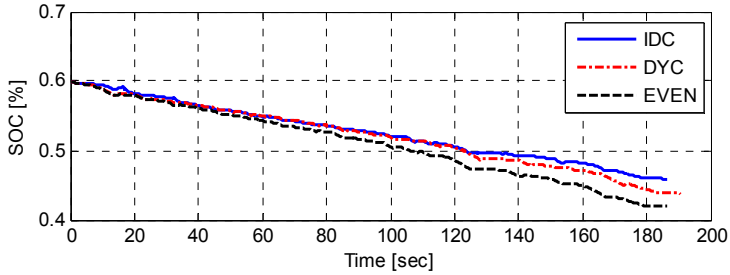

(a) Status of charge (SOC) in the case of ECMS

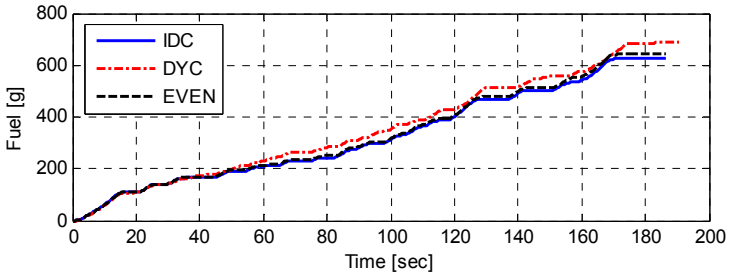

(b) Fuel consumption of engines (ECMS)

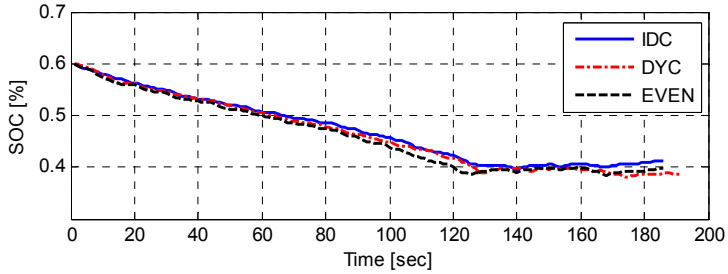

(c) Status of charge (SOC) in the case of thermostat

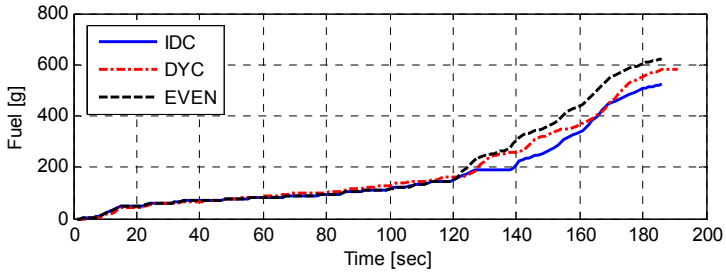

(d) Fuel consumption of engines (thermostat)

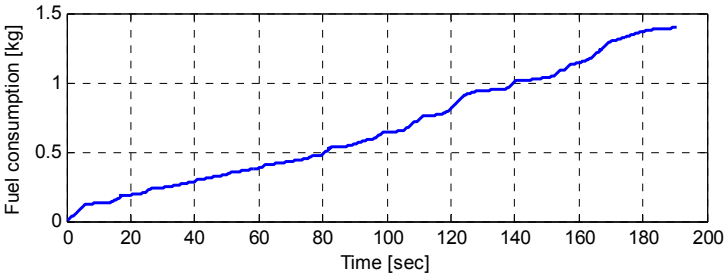

(e) Fuel consumption of engines (Diesel engine only)

Figure 5.28 Integrated performance verification of maneuver and power improvement

Through the results of analysis and integration, table 5.7 with comparison results of integrated performance can be obtained. All seven cases have been conducted to compare the integrated performance that consists of maneurvering and energy efficiency. Maneuvering performance of ECMS case is exactly identical to that of thermostat case, assuming that power system configuration, driving conditions and driving control algorithm are same except for the power management algorithm. Previously mentioned,

maneuvering performance of the IDC algorithm has been significantly improved. In terms of energy efficiency, the ECMS algorithm can achieve considerable improvement. In summary, the IDC based on the ECMS algorithm has been verified as the proper designed algorithm in order to satisfy integrated performance. In summary, the IDC based on the ECMS algorithm has been verified as the proper designed algorithm in order to satisfy integrated performance.

Table 5.7 Comparison of Integrated performance

ECMS	I. IDC	II. DYC	III. EVEN
Lap time	**186.4 [sec]**	**190.6 [sec]**	**186.6 [sec]**
Equivalent fuel	**962.58 [g]**	**1072.83 [g]**	**1073.77 [g]**
Fuel economy	**2991.96 [m/kg]**	**2684.48 [m/kg]**	**2682.13 [m/kg]**

Thermostat	IV. IDC	V. DYC	VI. EVEN
Lap time	**186.4 [sec]**	**190.6 [sec]**	**186.6 [sec]**
Equivalent fuel	**1157.82 [g]**	**1303.77 [g]**	**1309.72 [g]**
Fuel economy	**2487.43 [m/kg]**	**2208.97 [m/kg]**	**2198.94 [m/kg]**

Diesel	VII. EVEN
Lap time	**190.5 [sec]**
Fuel	**1397.03 [g]**
Fuel economy	**2061.51[m/kg]**

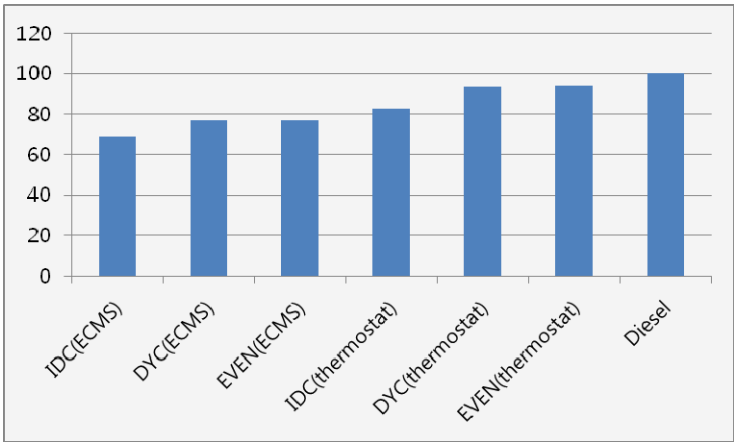

Figure 5.29 Fuel consumption ratio (based on diesel simulation result) [%]

5.9 Integrated Performance Verification using Test Track (DLC included)

Improved performance of the IDC based on the ECMS algorithm has been proved in previous section 5.8. In this section, double lane change has been included in the modified test track in order to simultaneously investigate stability and energy efficiency performance of the proposed algorithm. Figure 5.30 shows the modified test track. Initial velocity is set to 60 km/h and road friction coefficient is 0.85.

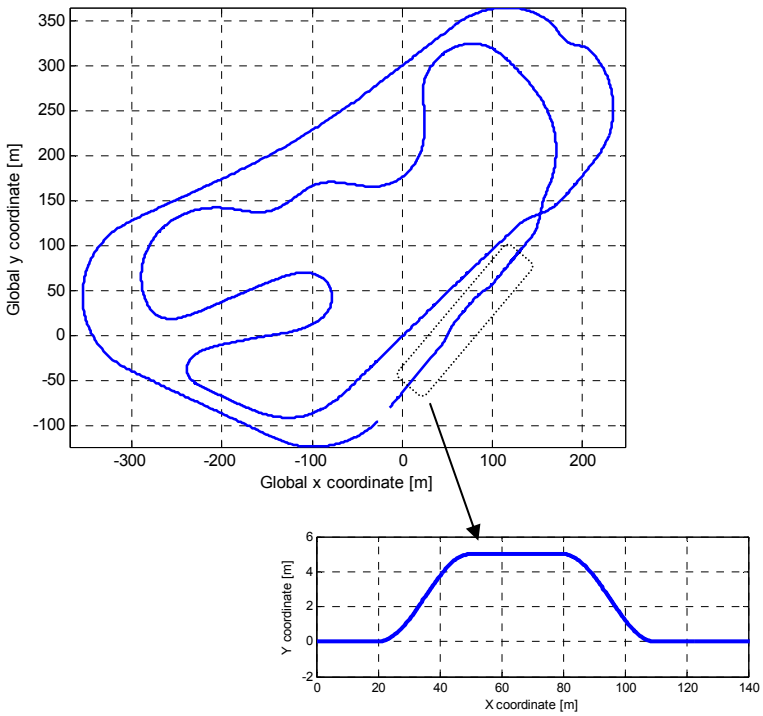

Figure 5.30 Double lane change included in test track

Figure 5.31 (a) and (b) show lateral distance and angle error. In the case of even distribution, vehicle status becomes unstable at 22 seconds. The lateral distance errors of the IDC and DYC simulation cases are less than 2 meters and angle error are guaranteed as small value.

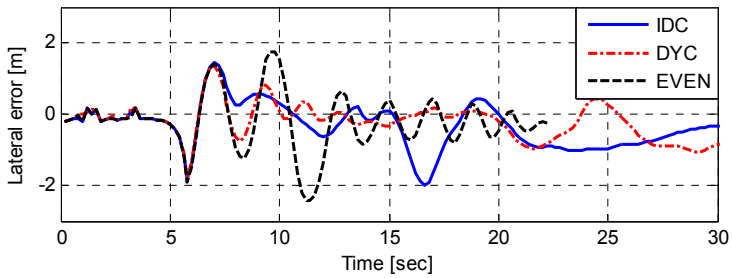

(a) Lateral distance error [m]

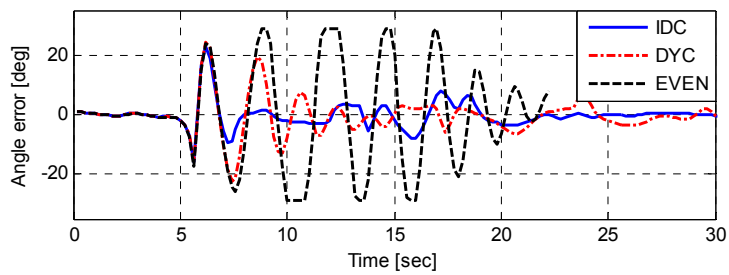

(b) Angle error [deg]

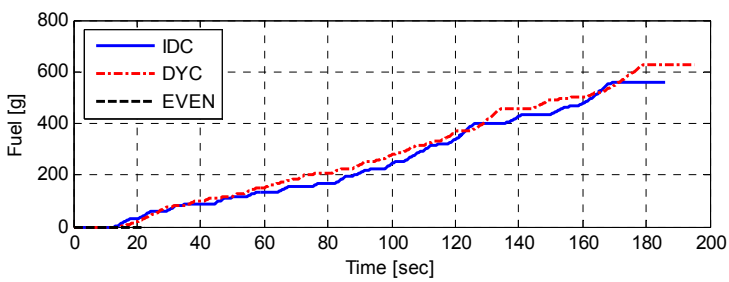

(c) Fuel consumption [g]

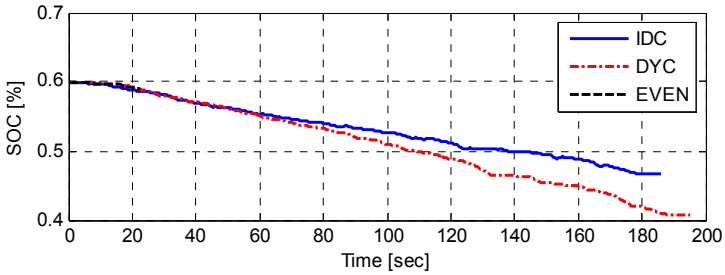

(d) SOC [%]

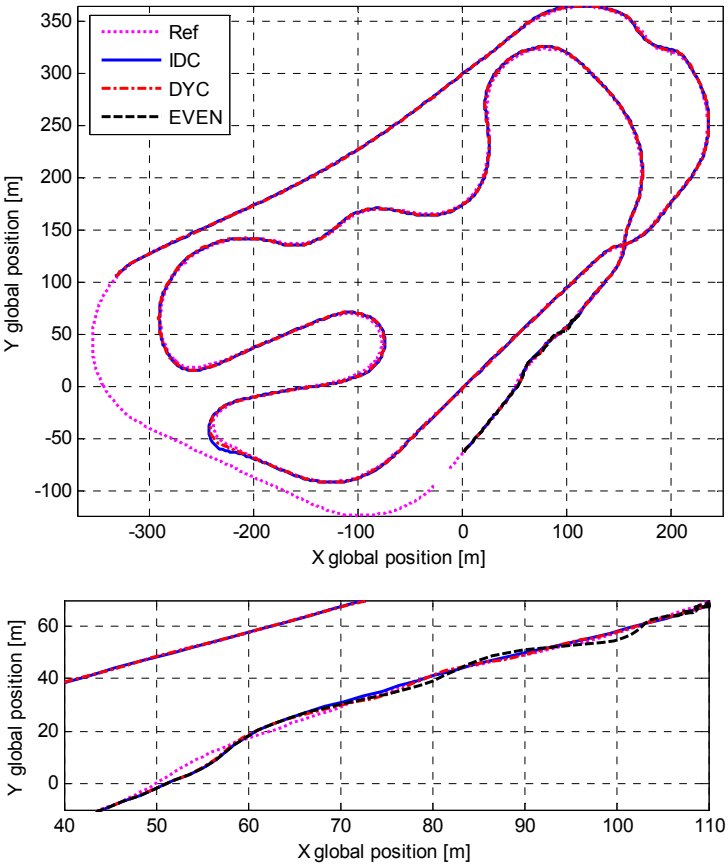

(e) Trajectories

Figure 5.31 Simulation results of the modified test track (DLC included)

Table 5.8 shows lap time and equivalent fuel consumption of these simulation results. Even distribution simulation was stopped at DLC road profile. Therefore, lap time and fuel consumption did not exist and could not be included in these results. The IDC and DYC algorithm, unlike even distribution algorithm, make the vehicle stable and increase energy efficiency. Moreover, the IDC algorithm has good maneuvering and energy saving performance while the vehicle stability is guaranteed.

Table 5.8 Comparison of Integrated performance (maneuvering, stability and energy efficiency)

ECMS	IDC	DYC	EVEN
Lab time	**185.84 [sec]**	**195.32 [sec]**	**-**
Equivalent fuel	**1011.99 [g]**	**1282.03 [g]**	**-**
Fuel economy	**2845.87 [m/kg]**	**2246.44 [m/kg]**	**-**

Chapter 6

Conclusion and Future Work

Development and performance verification of an integrated driving control algorithm for a 6WD/6WS series hybrid electric vehicle has been conducted. An integrated driving control system, which can prevent vehicle rollover and simultaneously improve maneuverability and lateral stability by independent drive and brake torque of six in-wheel motor, has been proposed in this dissertation. A hierarchical control structure, i.e. desired dynamics, upper level, lower level and power management layer, is adopted. The desired dynamics determines the steering angle of each wheel and the desired velocity according to driver's steering, throttle, and braking inputs. Stability decision, yaw moment control, and speed control algorithms are included in the upper level control layer in order to track the desired dynamics and guarantee yaw and roll stability. The lower level control layer, which is based on a control allocation method, computes actuator commands, such as independent driving and regenerative braking torques.

In the upper level control layer, the stability decision algorithm defines

stability regions on a g-g diagram and calculates the desired longitudinal acceleration, which is based on a G-vectoring control method, and the desired yaw rate for lateral and yaw stability, and rollover prevention. The speed control calculates the desired longitudinal net force, and the desired net yaw moment is determined to track the desired yaw rate. In the lower level control layer, the control allocation algorithm coordinates in-wheel motor output torque which is limited by performance of in-wheel motor and wheel slip control for preventing excessive wheel slip. From an electric standpoint, distributed output torque is also limited by amount of generable or regenerative power which can be generated in engine/generator and battery for preventing electric damages. For real-time implementation, the fixed-point control allocation method has been adopted among the other control allocation methods such as the cascaded generalized inverse, interior-point, active set algorithm. The execution time and accuracy are considered to select the proper algorithm that is suitable for real-time control systems. In the power management layer, the optimized engine/generator and battery output power are determined to minimize energy consumption. Fuel consumption minimization strategy (ECMS) is useful for on-line optimization and adopted to implement real-time application.

Finally, the results of the computer simulations using TruckSim, based on the open loop and closed-loop steering with various driving conditions, reveal that the proposed control algorithm can satisfactorily improve the maneuverability and stability. Specifically, the proposed control algorithm shows very good performance of turning, yaw rate tracking and rollover preventing, compared to the conventional vehicle and DYC algorithm which

is modified for six wheeled vehicle. In addition, from the view point of energy efficiency, the modified ECMS algorithm is able to achieve optimized fuel consumption. Amount of fuel consumption is relatively reduced about 14% and 23% respectively, compared to simple control algorithm, thermostat, and diesel engine.

The friction estimation algorithm has been developed to provide the proposed control algorithm. It is suitable for electric vehicle equipped with in-wheel motor and road condition that friction coefficient changes rapidly and drastically.

Real-time tests with manufactured test vehicle on various driving and road conditions will be conducted to improve the overall vehicle stability and performance of turning and climbing and braking in the future. And for more energy efficiency, a new fuel consumption strategy for on-line optimization needs to be designed to minimize energy loss which is generated by ignoring time-transient dynamic features of engine and generator.

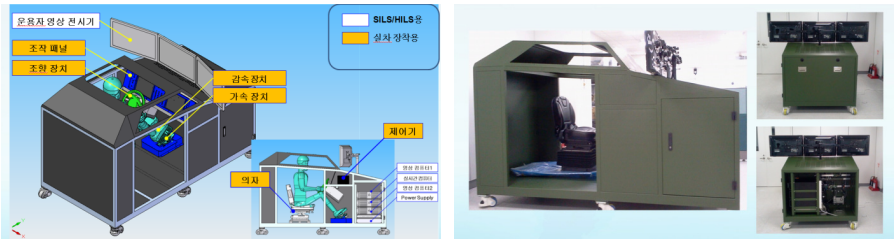

Figure 6.1 Hardware-in-the-loop simulation systems

Bibliography

[Van99] Van Zanten, A.T., Erhardt. R., Landesfei nd, K., &Pfaff, G., "VDC Systems Development a Yaw Moment Control using Braking Forces", JSME International Journal, Vol.42, No2, 1999, pp.301-308

[Masao02] Masao Nagai, Motoki Shino, Feng Gao, "Study on integrated control of active front steer angle and direct yaw moment", JSAE Review 23, 2002, pp.309-315

[Toki01] Toki Shino and Masao Nagai, "Yaw moment control of electric vehicle for improving handling and stability", JSAE Review22, 2001, pp.473-480

[Nagai99] Nagai, M., Yamanak, S. and Hirano, Y., "Integrated control of active rear wheel steering and yaw moment control using braking forces", JSME Int. J., Series C42, 2, 1999, pp.301-308

[Song07] Song, J. H., Kim, H.S. and Kim, B.S., "Vehicle longitudinal and lateral stability enhancement using a TCS and yaw motion controller", International Journal, Automotive Technology 8, Vol.1, 2007, pp.49-57

[Shibahata92] Shibahata, Y., Shimada, K., and Tomari, T., "The improvement of vehicle maneuverability by direct yaw moment control", Proc. Int. Symp. Advanced Vehicle Control, 1992, pp.452-457

[Huh00] K., Huh, J., Kim and J., Hong, “Handling and driving characteristics for six-wheeled vehicle”, Proceedings of the Institution of Mechanical Engineers, Part D, Journal of Automobile Engineering, Vol. 214, No.2, 2000, pp.159-170

[Jackson02] Andrew Jackson and David Crolla, “Improving Performance of a 6x6 off-Road Vehicle Through Individual Wheel Control”, SAE, 2002, 2002-01-0968

[Chen06] B.C., Chen, C.C., Yu and W.F., Hsu, “Optimal Steering Control for Six-Wheeled vehicle”, Proceeding of International Symposium on Advanced Vehicle Control, 2006, pp.605-610

[An06] S.J., An, H. Y., Lee, W. K., Cho, G., Jung, K. Yi, and K., Lee, “Development of steering algorithm for 6WS military vehicle and verification by experiment using a scale-down vehicle”, Proc. Int. Symp. Advanced Vehicle Control, 2006, pp.245-250

[An08] S.J. An, K. YI, G. Jung, K. I. Lee and Y. W. Kim, “Desired yaw rate and steering control method during cornering for a six-wheeled vehicle”, IJAT, Vol.9, No.2, 2008, pp.173-181

[Junya10] Junya Takahashi, Makoto Yamakado, Shinjiro Saito, and Atsushi Yokoyama, “A New Hybrid Stability-control System with Understeer-prevention Control based on G-Vectoring concept”, Proceedings of AVEC 2010, Paper ID 247, UK, 2010

[Joseph01] Joseph S. Brinker and Kevin A. Wise, “Flight testing of reconfigurable control law on the x-36 tailless aircraft, Journal of Guidance”, Control and Dynamics, 24(5), September 2001.

[Tondel05] Tondel, P. and T. A. Johanson, “Control Allocation for Yaw Stabilization in Automotive Vehicle using Multi parametric Nonlinear Programming”, American Control Conference, Proceedings of the 2005

[Brad06] Brad Schofield, tore Hagglund and Anders Rantzer, “Vehicle Dynamics Control and Control Allocation for Rollover Prevention”, Proceedings of the 2006 IEEE International Conference on Control Applications, Munich, German, October 4-6, 2006, pp149-154

[Burken99] J. J. Burken, P. Lu and Z. Wu, “Reconfigurable flight control designs with application to the X-33 vehicle”, Proceedings AIAA Guidance, Navigation and Control Conference, Paper AIAA 99-4134, Portland, OR, 1999

[Vanderbei98] R. Vanderbei, “LOQO : An interior point code for quadratic programming”, Princeton Univ., Princeton, NJ, Tech. Rep. SOR 94-12, 1998

[Virnig94] J. Virnig and D. Bodden, “Multivariable control allocation and control law conditioning when control effectors limit”, Proceedings of AIAA Guidance, Navigation, and Control Conference, Paper AIAA 94-3609, Scottsdale, AZ, 1994

[Bordignon96] K. A. Bordignon, “Constrained Control Allocation for Systems with Redundant Control Effectors”, Ph.D. Thesis, Dept. Aerospace & Ocean Eng., Virginia Polytechnic Institute & State Univ., Blacksburg, VA, 1996

[Härkegård02] O. Härkegård, “Efficient Active Set Algorithm for Solving Constrained Least Squares Problems in Aircraft Control Allocation”, Dept of Electrical Engineering, Linkopings University, Sweden, Tech. Rep. LiTH-ISY-R-2426, 2002

[Gelb71] G. H. Gelb, N. A. Richardson, T. C. Wang and B. Berman, “An electro-mechanical transmission for hybrid vehicle power trains – design and dynamometer testing”, SAE, Warrendale, PA, Tech. Rep. 710235, Jan 11-15, 1971

[Miller05] J. M. Miller and M. Everett, “An assessment of ultra-capacitors as the power cache in Toyota THS-II, GM-allision AHS-2 and ford FHS hybrid propulsion system”, in Proceedings of 20th Annu. Appl. Power Electron. Conf. Expo., 2005, vol.1, pp481-490

[Sasaki98] S. Sasaki, “Toyota’s newly developed hybrid powertrain”, presented at the IEEE 10th Int. Symp. Power Semicond. Devices ICs, Kyoto, Japan, Jun. 1998

[Hermance99] D. Hermance, “Toyota hybrid system”, presented at the SAE TOPTEC Conference, Albany, NY, May 1999

[Kimura99] A. Kimura, T. Abe and S. Sasaki, “Drive force control of a parallel-series hybrid system”, JSAE Rev., vol.20, pp.337-341, 1999

[Abe00] S. Abe, “Development of the hybrid vehicle and its future expectation”, SAE, Warrendale, PA, Teck. Rep. 2000-01-CA042, 2000

[Brahma00] A. Brahma, Y. Guezennec and G. Rizzoni, “Optimal Energy Management in Series Hybrid Electric Vehicles”, Proceedings of the American Control Conference Chicago, pp. 60~64, June 2000

[Perez06] L. V. Perez , G. R. Bossio , D. Moitre, G. O. Garcia, “Optimization of power management in an hybrid electric vehicle using dynamic programming”, Mathematics and Computers in Simulation, Vol. 73, Issue. 1, pp.244-254, November 2006

[Pisu07] P. Pisu and G. Rizzoni, “A Comparative Study Of Supervisory Control Strategies for Hybrid Electric Vehicles”, IEEE Transactions on Control Technology, Vol. 15, No. 3, May 2007

[Paganelli02] G. Paganelli, Y. Guezennec, and G. Rizzoni, “Optimizing control strategy for hybrid fuel cell vehicle”, SAE, Warrendale, PA, Tech. Rep. 2001-01-0102, 2002

[Pacejka02] Pacejka H.B, 2002, “Tyre and Vehicle Dynamics”, Butterworth Heinemann

[Yamakado10] M. Yamakado, J. Takahashi, S. Saito, A. Yokoyama and M. Abe, “Improvement in vehicle agility and stability by G-vectoring control”, Vehicle System Dynamics, Vol.48, 2010, pp231-254

[Yoon09] Yoon, J., Cho, W., Koo, B. and Yi, K., “Unified Chassis Control for Rollover Prevention and Lateral Stability”, IEEE Transactions on Vehicular Technology, Vehicular Technology, IEEE Transaction on, Vol.58, pp.596-609

[Burken01] Burken, J. J., Lu, P., Wu, Z., and Bahm, C., “Two Reconfigurable Flight-Control Design Methods: Robust Servomechanism and Control Allocation”, Journal of Guidance, Control, and Dynamics, Vol. 24, No. 3, pp. 482 - 493.

[Wang06] Wang J., R.G Longoria, “Coordinated Vehicle Dynamics Control with Control Distribution”, Proceedings of the 2006 American Control Conference, Minepolis, Minnesota, 2006, pp.5348-5353

[Durham93] Durham, W. C., “Constrained Control Allocation”, Journal of Guidance, Control and Dynamics 16, 717-725, 1993

[John94] John C. Virnig and David S. Bodden, “Multivariable control allocation and control law conditioning when control effectors limit”, In Proceedings of the AIAA Guidance, Navigation, and Control Conference, number AIAA 94-3609, pages 572–582, 1994.

[John04] John H. Plumlee, David M. Bevly and A. Scottedward Hodel, “Control of a Vehicle using Quadratic Programming based Control Allocation Techniques”, Proceedings of the 2004 American Control Conference, Boston, Massachusetts, 2004, Vol.5, pp.4704-4709

[Zhang95] Y. Zhang, D. Zhang, “On polynomiality of the mehrotra-type predictor-corrector interior-point algorithms”, Math. Program., vol.68, pp. 303-318, 1995

[Kim10] Wongun Kim, Kyongsu Yi, “Development of Driving Control System Based on Optimal Distribution for a 6WD/6WS Vehicle”, SAE2010, 2010-01-0091

[Kang07] Juyong Kang and Kyongsu Yi, “Development and Validation of a Finite Preview Optimal Control based Human Driver Steering Model”, KSAE spring conference, 2007, pp.855-860

[Kang10] Juyong Kang, Wongun Kim, Jongseok Lee and Kyongsu Yi, “Skid steering based control of a robotic vehicle with six-wheel drives”, Proc. IMechE, part D : Journal of Automotive Engineering, vol.224, pp.1369-1391

초 록

직렬형 하이브리드 기반 6 륜 인휠 차량의 최적 주행성, 안정성 및 에너지 효율을 위한 주행제어 알고리즘 개발

본 논문은 직렬형 하이브리드 기반 6 륜 인휠차량의 최적 주행성, 안정성 및 에너지 효율을 위한 주행제어 알고리즘 개발에 대하여 서술하였다. 대상 차량은 구동, 제동 및 조향이 독립적으로 가능한 시스템으로 구성되어 있다. 통합 주행제어 알고리즘은 6WD/6WS 차량의 최적 안정성, 주행성 및 에너지 효율을 위해 개발되었습니다. 제안된 알고리즘은 목표 동역학, 상위 제어, 하위 제어, 동력관리 계층을 포함하여 크게 4 부분으로 구성되어 있습니다. 목표 동역학 계층은 운전자의 조향, 구동 및 제동 입력을 통해 각 휠의 조향각과 목표 속도 및 제동량을 결정합니다. 안정성 판단/제어, 요 모멘트 제어 및 속도 제어는 상위 제어기에 포함되어 있다. 안정성 판단/제어는 차량의 안정성을 판단하여 횡안정성 및 전복 안정성을 확보하기 위하여 G-vectoring 과 요 모멘트 제어를 실시한다. 요

모멘트 제어는 요 안정성을 확보하기 위해 목표 요 속도를 만족시키는 목표 요 모멘트를 결정한다. G-vectoring 제어는 과도한 횡 가속도를 줄이기 위하여 종방향 가속도를 차량에 작용하게 하여 전복 안정성을 확보 하도록 설계하였다. 속도 제어는 운전자의 의도를 만족하기 위하여 슬라이딩 제어 기법을 기반으로 설계되었다. 하위 제어기는 각 휠의 슬립 상황, 인휠 모터의 토크 제한등을 고려하여 각 휠에 분배된다. 이를 위하여 Control Allocation 기법이 사용되었으며, 실시간 구현을 위하여 4 가지 해석 기법을 개발하고 적용하여 적합한 알고리즘을 적용하였다. 동력관리 제어는 차량 구동에 있어서 연료소모량을 최소로 하기 위한 전략을 기반으로 설계되었다. 등가 연료 소모량 최소 전략 (ECMS)이 사용되어 최적의 연료 효율을 확보하였다.

제어기 성능 검증을 위하여 컴퓨터 시뮬레이션을 수행하였다. 시뮬레이션 결과를 통해 일반 차량의 성능과 비교하여, 크게 향상된 안정성, 주행성 및 에너지 효율을 확인 하였다.

주요어 : 통합주행제어, 제어분배, 횡안정성, 전복안정성, 동력관리 제어

학 번 : 2008-30901